Monthly Notices of the ROYAL ASTRONOMICAL SOCIETY

MNRAS **545,** 1–30 (2026) https://doi.org/10.1093/mnras/staf2117
Advance Access publication 2025 November 28

JADES and BlackTHUNDER: rest-frame Balmer-line absorption and the local environment in a Little Red Dot at $z = 5$

Francesco D'Eugenio [1,2★] Ignas Juodžbalis [1,2] Xihan Ji [1,2] Jan Scholtz [1,2] Roberto Maiolino [1,2,3] Stefano Carniani [4] Michele Perna [5] Giovanni Mazzolari [6,7,8] Hannah Übler [6] Santiago Arribas [5] Rachana Bhatawdekar [9] Andrew J. Bunker [10] Giovanni Cresci [11] Emma Curtis-Lake [12] Kevin Hainline [13] Kohei Inayoshi [14] Yuki Isobe [1,2] Zhiyuan Ji [13] Benjamin D. Johnson [15] Gareth C. Jones [1,2] Tobias J. Looser [15] Erica J. Nelson [16] Eleonora Parlanti [4,6] Dávid Puskás [1,2] Pierluigi Rinaldi [13] Brant Robertson [17] Bruno Rodríguez Del Pino [5] Irene Shivaei [5] Fengwu Sun [15] Sandro Tacchella [1,2] Giacomo Venturi [4] Marta Volonteri [18] Christina C. Williams [19] Christopher N. A. Willmer [13] Chris Willott [20] and Joris Witstok [21,22]

Affiliations are listed at the end of the paper

Accepted 2025 November 14. Received 2025 November 3; in original form 2025 June 17

ABSTRACT

We present a 'Little Red Dot' (LRD) broad-line active galactic nucleus (AGN) at $z = 5.077$, observed with NIRSpec/MSA (micro-shutter assembly) and NIRSpec/IFU (integral-field unit) by the JADES (*JWST* Advanced Deep Extragalactic Survey) and BlackTHUNDER (Black holes in THe early Universe aNd their DensE surRoundings) surveys. Combining spatially resolved and high-resolution spectroscopy, we characterize its central engine, host, and environment. Hα has multiple components, including two broad Gaussians, yielding a black-hole mass $\log(M_\bullet/\mathrm{M}_\odot) = 7.65$, while [O III]$\lambda$5007 gives a galaxy dynamical mass $\log(M_{\rm dyn}/\mathrm{M}_\odot) = 9.1$, suggesting an overmassive black hole relative to the host galaxy. The target is immersed in a 7-kpc wide pool of ionized gas and has three neighbours: a satellite galaxy, a possible satellite/gas cloud, and a tentatively detected spatially detached outflow. Hα shows strong, rest-frame absorption, deeper than the continuum, ruling out a stellar origin. The velocity and velocity dispersion are $v_{\rm abs} = -13$ km s^{-1} and $\sigma_{\rm abs} = 120$ km s^{-1}. There is tentative evidence (2.6σ) of temporal variability in the equivalent width of the Hα absorber over two rest-frame months, suggesting a highly dynamic nucleus. Notably, while the Hα absorber is clearly visible and even dominant in the high-resolution *G*395*H* observations, it is not detected in the medium-resolution *G*395*M* data of the same epoch. This implies that the current incidence rate of absorbers in LRDs – and especially of rest-frame absorbers – may be severely underestimated, because most LRDs rely on lower resolution spectroscopy. The high incidence rate of rest-frame absorbers in LRDs may indicate a configuration that is either intrinsically stationary, such as a rotating disc, or that exhibits time-averaged stability, such as an oscillatory 'breathing mode' accretion with cyclic expansion and contraction of the gas around the supermassive black hole.

Key words: galaxies: active – quasars: supermassive black holes – galaxies: Seyfert.

1 INTRODUCTION

In the standard Lambda-cold dark matter (ΛCDM) cosmology, a key yet poorly understood agent in shaping galaxies is feedback from accreting supermassive black holes (SMBHs), which manifests via episodes of active galactic nuclei (AGNs). In the past few years, SMBH feedback has been invoked mainly to explain the low stellar-to-total mass fraction at dark-matter halo masses higher than $\sim 10^{12}$ M$_\odot$ (P. S. Behroozi, C. Conroy & R. H. Wechsler 2010; B. P. Moster et al. 2010). However, more recently, AGNs are being revisited as drivers in the low-mass range too. This paradigm shift stems from the convergence of new observational evidence (J. E. Greene & L. C. Ho 2004; J. E. Greene, L. C. Ho & J. S. Ulvestad 2006; M. Schramm et al. 2013; S. Satyapal et al. 2014; J. E. Greene, J. Strader & L. C. Ho 2020) and of recent theoretical progress (J. Silk 2017; S. Koudmani, D. Sijacki & M. C. Smith 2022).

Observationally, the pivot of this revolution in our view of AGNs has been the discovery of a large population of low-luminosity AGN ($L_{\rm bol} \lesssim 10^{45}$ erg s^{-1}) at redshifts $z = 2$–9, thanks to the superior sensitivity of *James Webb Space Telescope* (*JWST*). These objects are primarily identified via their broad permitted line emission, with no matching counterpart in the forbidden lines (D. D. Kocevski et al. 2023; H. Übler et al. 2023). In addition, a complementary population of narrow-line AGN is also thought to exist (J. Scholtz et al. 2025c), but these objects have received far less attention, because

★ E-mail: francesco.deugenio@gmail.com

identifying these hidden AGNs is significantly more challenging than for their broad-line counterparts. Due to a series of unfavourable coincidences, the optical tracers of narrow-line AGNs used at $z \lesssim 3$ and for more massive AGNs, (such as the BPT diagram; J. A. Baldwin, M. M. Phillips & R. Terlevich 1981) are inapplicable. In particular, low metallicity and lack of an extended low-ionization zone conspire to cluster both AGN and star-forming galaxies in the same region of the BPT diagram. As a result, these standard diagrams have been shown to fail to identify even secure AGN, such as AGN with broad permitted lines (e.g. D. D. Kocevski et al. 2023; H. Übler et al. 2023; I. Juodžbalis et al. 2025).

Nevertheless, even the broad-line population alone presents new challenges to our view of AGN, with the discovery of their X-ray and radio weakness, relative to the expectations derived from more luminous AGN. This weakness could be due to high covering factors of neutral and/or ionized gas (I. Juodžbalis et al. 2024a, hereafter: J24; V. Rusakov et al. 2025), or super-Eddington accretion rates $\lambda_{\rm E} > 1$ (E. Lambrides et al. 2024; F. Pacucci & R. Narayan 2024). Modelling the spectral energy distribution (SED) of these AGN has led to conflicting claims of 'overmassive' SMBHs (relative to the host stellar mass $M_\star$ and to local scaling relations; Y. Harikane et al. 2023; R. Maiolino et al. 2024; I. Juodžbalis et al. 2024b), or of normal SMBH–$M_\star$ scaling (Y. Sun et al. 2025), of possibly extremely massive host galaxies (B. Wang et al. 2024, 2025), or even of no SMBHs at all (J. F. W. Baggen et al. 2024; M. Kokubo & Y. Harikane 2025). Part of this confusion may be due to the use of the same terminology for different sample selections, so a clarification of our subjective language choice may be helpful.

Several low-luminosity, spectroscopically identified broad-line AGN appear red and compact in NIRCam imaging ('Little Red Dots', LRDs; J. Matthee et al. 2024). Many of these broad-line AGN have 'v'-shaped SEDs (L. J. Furtak et al. 2024; B. Wang et al. 2024, 2025; J24), which has led to searching for similar objects in photometry (J. E. Greene et al. 2024; D. D. Kocevski et al. 2025). However, many of these photometrically identified LRDs appear consistent with stellar-dominated SEDs (P. G. Pérez-González et al. 2024; C. C. Williams et al. 2024). Conversely, out of the population of spectroscopically confirmed broad-line AGN, the fraction of LRDs is fairly low (20–30 per cent; K. N. Hainline et al. 2024; A. J. Taylor et al. 2025). In light of the above, in this work we aim to study and discuss only broad-line AGN, with no bearing on photometrically identified samples.

Among low-luminosity, broad-line AGN, there is a high detection rate of Balmer-series absorption (J. Matthee et al. 2024), with velocities ranging from -340 to $+50$ km s^{-1}. The equivalent width (EW) of this absorption is generally too high to be explained by stellar atmospheric absorption (J. Matthee et al. 2024; I. Juodžbalis et al. 2024a; F. D'Eugenio et al. 2025a), implying the existence of dense absorbing gas clouds near the broad-line region (BLR, J. Matthee et al. 2024; B. Wang et al. 2025; J24). The high detection rate of these absorbing clouds provides essential information for deciphering the structure of this new population of AGN. In particular, a high covering factor could explain the X-ray weakness of these sources (B. Wang et al. 2025; J24). Moreover, the physical conditions, kinematics and chemical composition of these clouds may help us understand the balance between SMBH fuelling and outflows in this unexplored regime.

In this work, we present *JWST*/NIRCam and NIRSpec observations of a broad-line AGN at $z = 5$ with rest-frame Balmer-line absorption (Section 2). This galaxy was initially discovered by JADES (*JWST* Advanced Deep Extragalactic Survey; D. J. Eisenstein et al. 2023) and then re-observed by BlackTHUNDER (Black holes in THe early Universe aNd their DensE surRoundings) one year later. We present a full analysis of the images and integrated spectroscopy (Section 3), and present the resulting physical properties in Section 4; among these, we identify a rest-frame Hα absorber, with tentative evidence of EW variation. In Section 5, we present the surrounding environment. We conclude with a discussion of our findings (Section 6) and with a brief summary (Section 7).

Throughout this work, we assume a flat Λ-CDM cosmology with $H_0 = 67.4$ km s^{-1} Mpc^{-1} and $\Omega_{\rm m} = 0.315$ (Planck Collaboration VI 2020), giving a physical scale of 6.37 kpc arcsec^{-1} at redshift $z = 5.08$ (all physical scales are given as proper quantities). Stellar masses are total stellar mass formed, assuming a G. Chabrier (2003) initial mass function, integrated between 0.1 and 120 $M_\odot$. All magnitudes are in the AB system (J. B. Oke & J. E. Gunn 1983) and all EWs are in the rest frame, with negative EW corresponding to line emission.

2 DATA

2.1 Target galaxy 159717

Galaxy JADES-GS + 033223.41−275404.5 at $z = 5.07781 \pm 0.00003$ (hereafter, 159717) is located in the GOODS-South cosmological deep field (Great Observatories Origins Deep Survey; M. Giavalisco et al. 2004). It was first reported as a V-band drop-out, GSWV 2234354045, with a photometric redshift $z_{\rm phot} = 5.3$ (R. J. Bouwens et al. 2015). It was selected for follow-up spectroscopy as part of the JADES (M. Rieke 2020; D. J. Eisenstein et al. 2023; A. J. Bunker, NIRSPEC Instrument Science Team & JAESs Collaboration 2020), as a relatively bright NIRCam source ($F444W < 27$ mag) with photometric redshift $4.5 < z_{\rm phot} < 5.7$ (K. N. Hainline et al. 2024; priority 7.5 in table 4 of F. D'Eugenio et al. 2025d). JADES spectroscopy identified this galaxy as a Lyα emitter (G. C. Jones et al. 2024). Subsequently, the source was also targeted by BlackTHUNDER (Section 2.3). As a result, this galaxy is one of few such systems with deep, multi-epoch *JWST*/NIRSpec spectroscopy to date (in addition to A2744-QSO1; L. J. Furtak et al. 2025; X. Ji et al. 2025).

2.2 JADES Data

We use *JWST*/NIRCam imaging from JADES programme IDs PID 1180, 1210, and 1286 (M. J. Rieke et al. 2023; D. J. Eisenstein et al. 2023) and from FRESCO (the First Reionization Epoch Spectroscopic COmplete Survey, PID 1895; P. A. Oesch et al. 2023), in combination with legacy *Hubble Space Telescope* (*HST*)/ACS and WFC3 imaging from the Hubble Legacy Field data (K. E. Whitaker et al. 2019). The NIRCam data reduction from JADES has been presented in the public data release (DR) articles (M. J. Rieke et al. 2023; D. J. Eisenstein et al. 2025; F. D'Eugenio et al. 2025d). We also use NIRSpec (P. Jakobsen et al. 2022) micro-shutter assembly spectroscopy (MSA; P. Ferruit et al. 2022), obtained as part of PID 1286. These data were selected and observed in the 'medium jwst gs' tier of JADES (D. J. Eisenstein et al. 2023). An RGB false-colour image of the target, with the MSA shutters overlaid is shown in Fig. 1(a), with a bright interloper in the foreground. The MSA observations consist of 8009 s with prism, $G140M$ and $G395H$, and 9322 s with $G235M$ and $G395M$. These integration times were split into two times three nodded exposures, using the NRSIRS2 readout mode (B. J. Rauscher et al. 2012, 2017). We used the nodded exposures to subtract the background, leading to possible foreground-source subtraction due to the contaminant. For the prism, we use only half the nodded pairs, to avoid subtracting

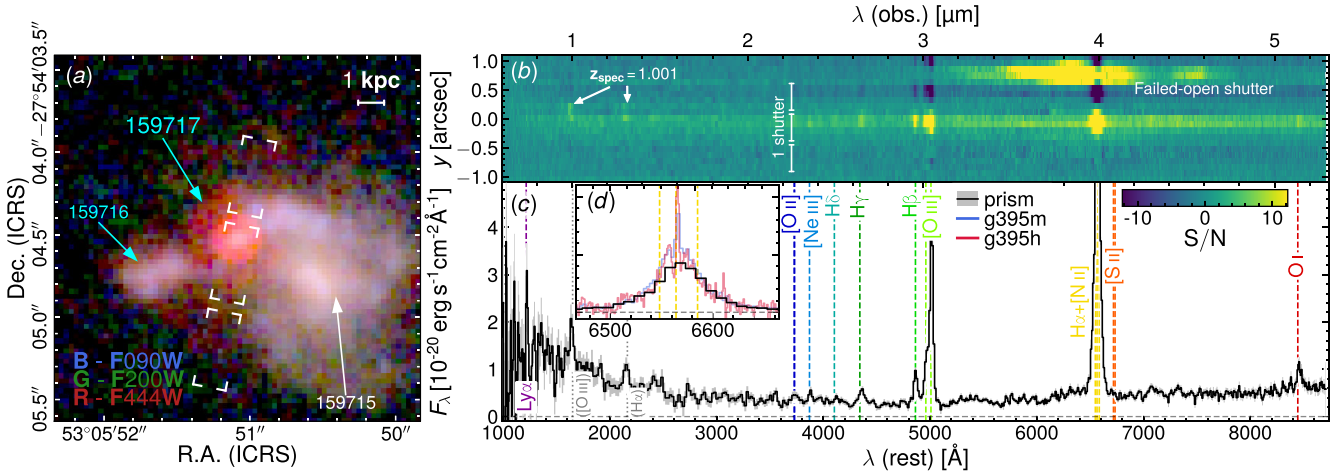

Figure 1. Summary of the JADES observations. Panel (a); RGB NIRCam image, highlighting the target AGN at $z = 5.077$ (red hues), a satellite to the East, and a foreground spiral galaxy. The white corners trace the vertices of the NIRSpec/MSA microshutters. Panel (b); 2D signal-to-noise map from NIRSpec/MSA prism. Balmer and high-ionization lines from the AGN are clearly visible; in the rest-frame UV, there are several faint signatures of the blended complexes Hβ and [O III]λ5007, and Hα and [N II] λ6583 from the foreground star-forming regions. A relatively strong line at $\lambda = 5.14$ μm is identified as the resonant O I λ8446. Panel (c); 3-pixel (0.3-arcsec) extraction prism spectrum centred on the AGN. Foreground emission-line contamination in the rest-frame UV is marked by vertical dotted lines. Note the red optical spectrum (i.e. positive slope), and the large Balmer decrement Hα/Hβ, typical of LRDs. The inset Panel (d) shows a zoom-in around Hα, with the *G395M* and *G395H* spectra in blue and pink, respectively.

the light from a 'disobedient' open shutter, which contains a bright feature (possibly polycyclic aromatic hydrocarbon emission; visible in the top 0.5 arcsec of Fig. 1b). Apart from this tailored setting, the data reduction process is the same as described in the JADES DR1 and DR3 articles (A. J. Bunker et al. 2024; F. D'Eugenio et al. 2025d). We used point-source path-loss corrections appropriate for an unresolved source. Due to the presence of multiple nearby sources, it is essential to separate physically associated systems from foreground and background systems. Where spectra are not available, we use photometric redshifts z_{phot} from EAZY (G. B. Brammer, P. G. van Dokkum & P. Coppi 2008), using photometry from JADES DR2 (D. J. Eisenstein et al. 2025) and the methods outlined in K. N. Hainline et al. (2024). The JADES DR1 and DR3 NIRSpec data reduction has a 15 per cent systematic offset between the gratings and prism fluxes (A. J. Bunker et al. 2024; F. D'Eugenio et al. 2025d). Since the prism flux calibration is in agreement with NIRCam (A. J. Bunker et al. 2023), we downscale all the grating spectra from JADES by a factor of 0.85. This brings the Hα flux measured from the gratings in agreement with both the prism value and with the value from the BlackTHUNDER G395H spectrum, which uses a more recent calibration (Section 2.3).

NIRCam shows a crowded field (Fig. 1a; see also Fig. 2), with a satellite JADES-GS + 033223.44−275404.7 (hereafter: ID 159716) at photometric redshift $z_{phot} = 5.22 \pm 0.08$ ($z_{spec} = 5.07622 \pm 0.00002$; Section 5.1), and behind the foreground spiral galaxy J033223.38−275404.6 (CANDELS ID GS-1826, Cosmic Assembly Near-infrared Deep Extragalactic Legacy Survey, Grogin et al., 2011, Koekemoer et al.,2011; JADES ID JADES-GS-159715; hereafter: 159715) at $z_{phot} = 1.18 \pm 0.06$ ($z_{spec} = 1.00115 \pm 0.00001$; Appendix A). The presence of this interloper complicates significantly our analysis; most relevant to this work, we estimate that the additional foreground dust attenuation correction for the AGN is a secondary effect (Section 3.9) and there is no significant magnification from gravitational lensing (Appendix B).

The prism spectrum shows the characteristic 'v'-shaped inflection of some LRDs, combining a blue UV (ultraviolet) slope $\beta_{UV} = -2$ with a red rest-frame optical continuum, with the inflection point near

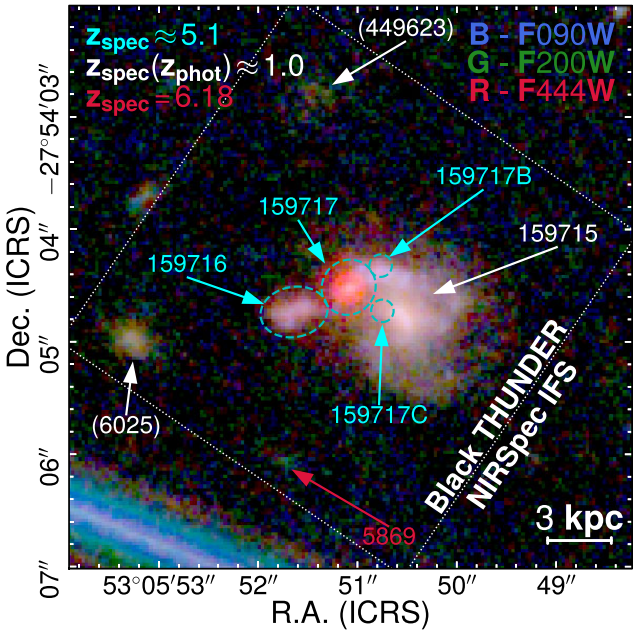

Figure 2. The NIRSpec/IFS field of view overlaid on false-colour NIRCam image. Dashed ellipses and circles are the apertures used to extract the spectra of 159717 and physically associated galaxies, 159716 and two more emission-line detections (159717B and 159717C) which are not visible in this image. Other clearly detected sources in the field of view are indicated. Names in cyan are physically associated with 159717; names in white are in the foreground (with names in parentheses indicating sources without a spectroscopic redshift). The galaxy in red is in the background. Galaxy names that do not end in a letter are from the JADES catalogue v1.0.

the Balmer limit (D. J. Setton et al. 2025a). We lack MIRI coverage to explore if the SED of our target displays the rest-frame 1.6-μm turnover typical of stellar-dominated spectra (P. G. Pérez-González et al. 2024; C. C. Williams et al. 2024).

The rest-UV spectrum shows tentative evidence of Lyα emission (G. C. Jones et al. 2024, but our spatially resolved data suggests this may be [O II]$\lambda\lambda$3726,3729 emission at $z = 1$ from 159715; Appendix A), and a possible 2-γ or damped Lyα absorption (DLA) continuum. These features have been associated with AGN in the past (Y. Li et al. 2024; S. Wu et al. 2024; S. Tacchella et al. 2025, but see A. J. Cameron et al. 2024; C. Terp et al. 2024 for different interpretations). The rest-frame UV spectrum also shows evidence for two lines at $\lambda = 1.05$ and 1.36 μm, present in both the prism and medium-resolution *G*140*M* data. The 1.05-μm line is spectrally resolved into a doublet; these are therefore the [O III]$\lambda\lambda$4959,5007 doublet and Hα from the northern spiral arm of 159715 at $z_{\rm spec} = 1.00115$. At this redshift, and due to the low resolution of the prism, Lyα could also correspond to [O II]$\lambda\lambda$3726,3729 in the foreground. Similarly, a tentative line at 1.16 μm matches very well both [C III] λ1909 in the AGN but also He Iλ5875 at $z = 1$.

The rest-frame optical spectrum shows both Balmer and metal-line emission. The latter include [O II]$\lambda\lambda$3726,3729, [Ne III] λ3869, [O III]$\lambda\lambda$4959,5007, and the fluorescent O I λ8446. The Balmer emission is broad, as highlighted also in Fig. 1(d), where we show Hα as observed in the medium- and high-resolution gratings. The width of Hα exceeds a full-width half-maximum of FWHM = 1500 km s^{-1}; coupled with the narrow emission from the forbidden [O III]$\lambda\lambda$4959,5007 lines (dispersion $\sigma \sim 50$ km s^{-1}), this is strong evidence for an AGN BLR. This explanation resonates with the detection of the O I λ8446 line, a high-energy resonant line which is very faint in star-forming galaxies (A. L. Strom et al. 2023), but is common in AGN hosts (R. J. Rudy, G. S. Rossano & R. C. Puetter 1989; I. Juodžbalis et al. 2024a). The Balmer emission is dominated by the broad component, but a narrow component is clearly visible. The high-resolution spectrum shows clear evidence for Hα absorption too (Section 3).

2.3 BlackTHUNDER Data

BlackTHUNDER is a *JWST*/NIRSpec programme (PID 5015; PIs: H. Übler and R. Maiolino) that targets 20 low-luminosity broad-line AGN using NIRSpec integral-field spectroscopy (IFS; T. Böker et al. 2022). The sample consists of broad-line AGN at $z > 5$, so 159717 was included for follow-up spectroscopy after being first identified in JADES. The observing setup has two visits, using the prism and the *G*395*H* grating, consisting of 14 dithered integrations each. For the prism, we used the NRSIRS2RAPID readout mode, with 37 groups per integration and a single integration per dither, totalling 7761 s. For the grating, we used NRSIRS2 and 23 groups per integration, totalling 23 692 s. The observations were strongly affected by anomalous proton flux, resulting in a higher rate of artefacts.

We processed the raw files using the *JWST* Science Calibration pipeline JWST (C. Alves de Oliveira et al. 2018), version 1.15.0, with the calibration files specified by the Calibration Reference Data System (CRDS) context file number 1281. Additional processing steps were performed, following the procedure developed by M. Perna et al. (2023). Residual pink noise was corrected using a polynomial fit. We manually masked regions affected by open shutters from the NIRSpec MSA (P. Ferruit et al. 2022), and by strong cosmic rays. Remaining outliers were flagged in individual exposures using the Laplacian edge detection algorithm (P. G. van Dokkum 2001), as implemented by F. D'Eugenio et al. (2024). From the reduced 2D frames, we created the rectified data cubes using the 'drizzle' algorithm and an output grid with 0.05-arcsec spaxels.

The background was subtracted by creating a white image and an emission-line image, obtained respectively by taking the median across all wavelengths, and across a narrow wavelength window centred on [O III]λ5007. We ran SExtractor (E. Bertin & S. Arnouts 1996) to create a segmentation map for each of the two images, we then padded these segmentation maps by two spaxels, and finally defined the source mask as the union of the two padded segmentation maps. We estimate the background for each wavelength pixel using the background algorithm from the ASTROPY package (Astropy Collaboration 2013, 2018), with a 5×5 filtering window, and with spatial interpolation across the windows and across the source mask. The resulting background datacube was smoothed in wavelength using median filtering and a window of 25 pixels. The quality of the resulting background-subtracted cube was assessed by taking random apertures (outside of the source mask) and verifying that their flux was consistent with zero.

2.4 Field characterization and redshift determination

The IFS field of view is illustrated in Fig. 2, where we also indicate foreground and background sources detected from photometry. The known interloper 159715 has already been discussed (Section 2.2), but BlackTHUNDER high-resolution spectroscopy detects Paα in the northern spiral arm, enabling a precise redshift measurement (Appendix A). The two galaxies JADES-GS-449623 and JADES-GS-6025 are identified in the JADES catalogue v1.0 (JADES Collaboration, in preparation); they have photometric redshift $\approx$ 1 (K. N. Hainline et al. 2024), but we are unable to provide spectroscopic confirmation, because no emission lines are detected by BlackTHUNDER. We confirm spectroscopically JADES-GS-5869, via detection of [O III]$\lambda\lambda$4959,5007 and Hα in the prism spectrum, yielding $z = 6.190 \pm 0.001$. We also indicate the locations of 159717B, a much fainter emission-line source at the same redshift as 159717, and yet another emission-line source (159717C); these two objects are not visible in Fig. 2, but are discussed in Section 5.

2.5 BlackTHUNDER aperture spectra

To study the main target 159717, we define two aperture spectra: a 'total' aperture of semimajor axis $R_{\rm ap} = 0.25$ arcsec (1.6 kpc; to capture the total flux of the galaxy) and a smaller aperture with $R_{\rm ap} = 0.125$ arcsec (0.8 kpc), to maximize the signal-to-noise ratio (SNR) at the expense of inaccurate aperture losses, due to the resolved nature of the target in [O III]λ5007. To define these apertures, we use a curve-of-growth approach. We create an image of the broad-line Hα by co-adding the cube along the wavelength slices in the wings of the broad line, at a wavelength of 4 μm (see Section 3.3). We then model the resulting image as a Gaussian light profile plus linear background, using GALFIT (C. Y. Peng et al. 2002, 2010), with the assumption that the source is unresolved in broad Hα, and that this emission line traces the instrument point spread function (PSF). The best-fitting Gaussian model has axis ratio 0.9 and position angle −25.4°. The PSF is elongated in the direction along the IFU slices, in agreement with F. D'Eugenio et al. (2024), but here we find a considerably larger FWHM than in F. D'Eugenio et al. (2024), with FWHM = 0.175 arcsec along the slicers. This larger PSF is in agreement with independent measurements (the bright quasar J0224−4711, M. Perna, in preparation; G. C. Jones et al. 2025; S. Zamora et al. 2025). The disagreement is due to F. D'Eugenio et al. (2024) using a less accurate method than here, based on forward modelling an extended target starting from the NIRCam images.

We create a set of aperture spectra by summing the light inside elliptical apertures with the same shape and centre as the best-fitting Gaussian model, with increasing semimajor axis in steps of one 0.05-arcsec spaxel, starting from one and reaching 10 spaxels. For each

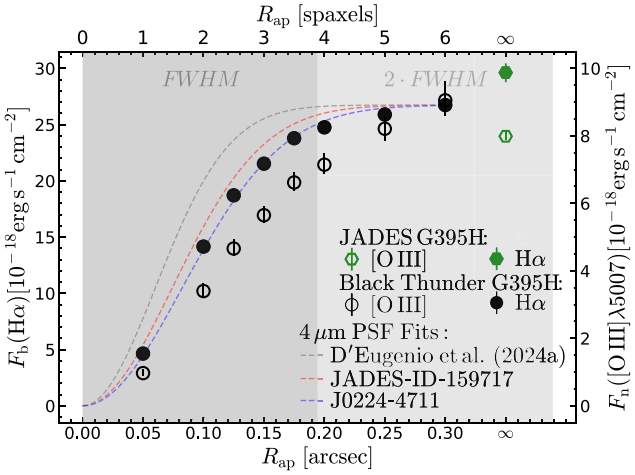

Figure 3. Curve of growth of emission lines from BlackTHUNDER (black circles), compared to the JADES aperture-corrected values (green). The empty symbols trace narrow [O III]λ5007 flux (right axis), the filled symbols are broad Hα (left axis). The Hα fluxes are corrected for $n = 2$ hydrogen absorption (Sections 3.2–3.4). The dashed lines are curves of growth of Gaussians of varying FWHM. Broad Hα closely follows a Gaussian profile, while [O III]λ5007 displays a less steep slope which implies a spatially resolved nature. Our fiducial aperture has $R_{ap} = 0.25$ arcsec, so it does not require large aperture corrections. We also use a smaller aperture to maximize the SNR, but this smaller aperture, with point-source aperture corrections, may underestimate the flux of [O III]λ5007, which is not point-like, unlike broad Hα. The grey curve is estimated from an extended source; the blue curve is estimated from the broad Hα emission line of the QSO J0224−4711.

wavelength pixel of the aperture spectrum, the flux is determined by adding all spaxels from the corresponding wavelength slice, weighting each spaxel only by the fractional area inside the current elliptical aperture. This approach does not benefit from the increased precision of inverse variance, but avoids biasing the result. To remove outliers, we use 4σ clipping for each wavelength slice: we first divide the current slice by the PSF, then we calculate the median and define σ as half the 84th–16th interpercentile range of the data. Finally, we assign weight zero to all voxels deviating more than 4σ from the median. The uncertainties are estimated by repeating the same procedure on the variance datacube. The resulting error spectrum is upscaled to match the empirical noise observed in the aperture spectrum. To do so, we estimate the effective noise on the aperture spectrum by calculating the standard deviation about the median-filtered spectrum inside a moving window, neglecting emission-line regions. We then upscale the original error spectrum to match the median value of the empirical error spectrum. This preserves wavelength-specific noise features like photon noise around bright emission lines and under-exposed pixels.

Our fiducial aperture to study 159717 has semimajor axis of 0.25 arcsec, which encloses ∼90 per cent of the PSF flux at the wavelength of Hα (cyan dashed circle in Fig. 2; see also S. Zamora et al. 2025). We also consider a smaller aperture of radius 0.125 arcsec; this second aperture maximizes the SNR of the spectrum, but we apply an aperture-correction factor of 1.22 to capture the total Hα flux. This accuracy of aperture choice is validated in Fig. 3, where we show the emission-line fluxes from narrow [O III]λ5007 and from broad Hα as a function of aperture radius, without applying any aperture-loss correction. The circles with uncertainties are measurements from BlackTHUNDER (Sections 3.2 and 3.3), while the green hexagons are measurements from JADES (Section 3.4). The empty/filled symbols refer to the fluxes of [O III]λ5007 and of broad H α. The dashed lines compare the curve of growth of three PSFs: the model from F. D'Eugenio et al. (2024, grey line), which clearly underestimates the FWHM; a simple Gaussian fit to the broad Hα image (red), and a Gaussian fit to the broad Hα wing of the J0224−4711 QSO.

The different curves of growth between the filled and empty symbols highlight the spatially extended nature of [O III]λ5007, while the broad Hα follows closely a Gaussian profile as expected from a point source. The neighbours contribution to [O III]λ5007 begins around $R > R_{ap} \sim 0.2$ arcsec.

Having located the neighbours, we create aperture spectra to measure their systemic redshift and emission-line ratios. For 159717B and 159717C, which are not spatially resolved (Section 3.1), we use circular apertures of radius 0.1 arcsec, which ensure maximum possible SNR. For 159716, which is extended, we use an elliptical aperture that encloses the full NIRCam-detected flux. These three apertures are outlined in Fig. 2.

As noted by H. Übler et al. (2023), aperture spectra that assume uncorrelated noise result in severely underestimated uncertainties. We therefore upscale the uncertainties spectrum by a factor of four, estimated by comparing the robust standard deviation of the fit residuals to the nominal uncertainties.

3 ANALYSIS

3.1 Size measurement

LRDs are known to have compact sizes in the rest-frame optical (L. J. Furtak et al. 2023; M. Killi et al. 2024), consistent with the broad lines and optical continuum being dominated by AGN (A. Graaff et al. 2025; X. Ji et al. 2025; R. P. Naidu et al. 2025). Where sufficiently deep NIRCam imaging is available, the rest-frame UV sizes are often extended (M. Killi et al. 2024; J24), often displaying complex UV morphologies (P. Rinaldi et al. 2025). However, the case in hand is complicated by the presence of the foreground contaminant. We adopt two complementary approaches. The first method leverages the well understood PSF and noise properties of NIRCam, but suffers from considerable contamination by 159715 and self-contamination from the red LRD continuum. The second method uses the [O III]λ5007 line map from the NIRSpec/IFS *G*395*H* observations, which suffer from no continuum contamination but have a larger PSF and poorer noise performance than NIRCam, due to correlated noise in the aperture (Section 2.5).

For the first method, we create an emission-line map of the target by subtracting the PSF-matched *F*200*W* image (which does not contain strong emission lines) from the *F*277*W* image (which contains Hβ and [O III]λ5007). The resulting image is shown in Fig. 4(a). Due to the complex nature of the field, we adopt generous masking around the bulge of 159715 and, to the north, a diffraction spike from a bright star. We model five sources, based on fitting and inspecting the residuals. These consist of a point source and a Sérsic profile at the location of 159717, two Sérsic profiles to describe the 'cigar-shaped' 159716, and a point source to describe 159717B. The centre of each source is marked by a cross marker in Figs 4(a)–(c). We infer the model parameters using PYSERSIC (I. Pasha & T. B. Miller 2023), adopting the empirical *F*277*W* PSF from Z. Ji et al. (2024). The fitting setup is the same as F. D'Eugenio et al. (2025f).

The marginalized posterior probabilities on key model parameters are reported in Table 1, and the fiducial (maximum a-posteriori; MAP) model and the data-model χ residuals are illustrated in Figs 4(b) and (c). The χ map highlights the presence of significant

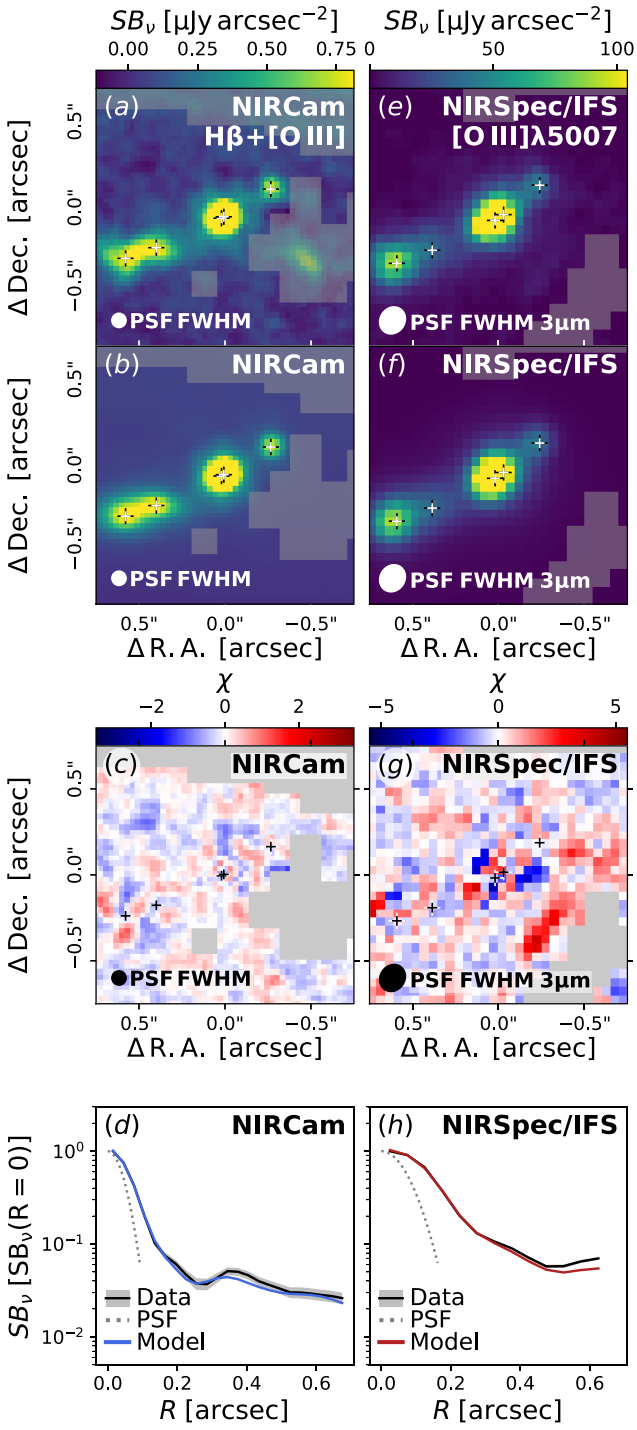

Figure 4. Sérsic models of the NIRCam $F277W-F200W$ image (capturing Hβ and [O III]λλ4959,5007 at $z = 5$; panels a–d) and of the NIRSpec/IFS [O III]λ5007 map (panels e–h). We model the scene using five components (centred on the black/white crosses). The four rows are the data, MAP model, residuals, and the surface brightness profile. The main galaxy 159717 (centre of cutouts) is modelled as a superposition of a point-source and a Sérsic component, with a flux ratio of 0.6–0.7. The galaxy is spatially resolved, with the Sérsic component having intrinsic half-light semimajor axis $R_e = 200$ and 900 pc in the NIRCam and NIRSpec/IFS models, respectively. Given the red $F277W-F200W$ continuum colour of LRDs, the NIRCam image in panel (a) also includes continuum flux, which is absent in the NIRSpec/IFS image (we used a wavelength band of 150 km s^{-1}).

residual substructure, but we deem this a satisfactory model, given the complexity of the field and the ongoing interaction between the galaxies. For 159717, we find a flux ratio between the point-source and Sérsic component of 0.7 ± 0.2; the Sérsic component has a very large index $n = 4.5$, albeit the uncertainties are also large. The semimajor axis half-light radius is extremely compact, $R_e = 0.21 \pm 0.06$ kpc; for reference, a galaxy with stellar mass $M_\star = 10^8$–10^9 M$_\odot$ has $R_e = 0.5$–0.8 kpc at redshift $5 < z < 6$ (T. B. Miller et al. 2025). For 159717, we tested forcing an exponential disc profile using a Gaussian prior probability with mean $n = 1$ and standard deviation 0.1; this results in a twice larger R_e, but also in two times lower flux, with the point-source component becoming the brightest of the two. The satellite galaxy 159716 has larger size than 159717, with the two (spatially offset) components having $R_e = 0.8$ and 0.9 kpc, respectively. These values are close to the expectations for a galaxy as massive as 159716 (Section 5.2).

The second approach is equivalent, aside from the data and mask used, and from the larger and non-circular PSF of NIRSpec/IFS (Section 2.5). The emission-line map has been created by taking the median of the datacube in a 150-km s^{-1} window centred on [O III]λ5007 (Fig. 4e). We find no evidence of contamination from the foreground galaxy, but there are low-intensity artefacts that we mask. A relatively bright, elongated feature is not masked; this could be an artefact, but is very close to the location of 159717C. We use the same five components to model the system and the same inference method as for NIRCam.

The inference results are displayed in Figs 4(e)–(h) and are reported in the bottom five rows of Table 1. For 159717, we find $R_e = 0.92 \pm 0.02$ kpc, 4.5 times larger than for NIRCam. A likely explanation is that the NIRCam emission-line map suffers from substantial contamination from the object continuum, which may arise from a compact or even unresolved component (A. Graaff et al. 2025; R. P. Naidu et al. 2025). This is confirmed by the prism observations, which indeed detect a compact continuum source (Appendix C). In contrast, NIRSpec/IFS can accurately identify [O III]λ5007 emission and eliminate any underlying continuum. The Sérsic index is significantly lower than for NIRCam $n = 1.9 \pm 0.2$ (3σ difference) and the shape is considerably rounder. The origin of this discrepancy is unclear, but a possibility is that the NIRCam emission-line map $F277W-F200W$ is heavily biased by a point-source continuum, thus yielding a more compact solution. However, the flux ratio between the point-source and Sérsic components is 0.57 ± 0.04, consistent with the NIRCam value, so overall the difference may be dominated by systematics, e.g. in the PSF determination. For 159716, the sizes are in good agreement with NIRCam.

In Section 5, we will show that the kinematic properties of the [O III]λ5007-emitting gas surrounding 159717 suggest a merger scenario. In this context, it is reasonable to expect the gas to be more extended than the continuum – particularly because we find no evidence of gaps in the gas distribution or in its velocity field (see again Section 5). This suggests that the half-light [O III]λ5007 size measured from NIRSpec/IFS should not be used for calculating the dynamical mass of the system. For this reason, hereafter we adopt the NIRCam R_e value of 0.21 ± 0.06 kpc as the fiducial size measurement for 159717. However, we also present the corresponding NIRSpec measurements for comparison. Note that these R_e values already remove the contribution of the unresolved component. Had we modelled 159717 with a single Sérsic profile without separating the point-source contribution, the resulting R_e would be even smaller, giving even lower constraints on the dynamical mass.

Table 1. Morphological parameters of the sources at $z = 5.077$, derived from PYSERSIC modelling.

Source ID	Data	Profile	F_ν^a (μJy)	n –	q –	PA (rad)	R_e (pixels^b)	R_e (kpc)
159717	NIRCam	Sérsic	0.063 ± 0.011	4.5 ± 1.6	0.44 ± 0.17	2.0 ± 0.2	1.1 ± 0.3	0.21 ± 0.06^c
159717	”	Point Source	0.042 ± 0.011	–	–	–	–	–
159716	”	Sérsic	0.053 ± 0.008	1.8 ± 0.7	0.40 ± 0.09	1.7 ± 0.1	4.6 ± 0.9	0.9 ± 0.2
159716	”	Sérsic	0.036 ± 0.006	2.5 ± 1.1	0.16 ± 0.06	1.6 ± 0.07	4.0 ± 0.8	0.8 ± 0.2
159717B	”	Point Source	0.015 ± 0.001	–	–	–	–	–
159717	NIRSpec/IFS	Sérsic	8.2 ± 0.4	1.9 ± 0.2	0.98 ± 0.02	1.7 ± 0.8	2.9 ± 0.06	0.92 ± 0.02^c
159717	”	Point Source	4.7 ± 0.2	–	–	–	–	–
159716	”	Sérsic	6.5 ± 0.5	6.0 ± 1.0	0.95 ± 0.05	1.5 ± 0.9	2.5 ± 0.3	0.8 ± 0.1
159716	”	Sérsic	2.9 ± 0.3	0.8 ± 0.1	0.53 ± 0.05	1.86 ± 0.07	3.4 ± 0.3	1.1 ± 0.1
159717B	”	Point Source	1.0 ± 0.1	–	–	–	–	–

Notes. Each row corresponds to a source, as indicated in column 1. The first five and bottom five rows report the parameters inferred from the NIRCam and NIRSpec/IFS data (column 2). 159717 and 159716 are modelled with two components, 159717B with a single point-source component, and 159717C is not modelled. The columns report the marginalized posterior distributions on the model parameters, with the median and 16th–84th percentile range. [a] For NIRCam, F_ν is the difference in flux density between the $F200W$ and $F277W$ wide-band filters. For NIRSpec/IFS, F_ν is the average flux density inside a narrow wavelength window of 150 km s^{-1}, centred on [O III]λ5007 (hence the much higher F_ν in NIRSpec than in NIRCam).
[b] We use 0.03-arcsec pixels for NIRCam and 0.05-arcsec spaxels for NIRSpec/IFS.
[c] The large difference between NIRCam and NIRSpec could be due to NIRSpec being more sensitive to the emission-line morphology, while the NIRCam emission-line map may suffer from contamination from the point-source continuum.

3.2 Emission-line measurement methods

To measure the emission lines, we use a Bayesian approach, using different models as specified in the following sections. To integrate the posterior distribution, we use the Markov Chain Monte Carlo (MCMC) method, with the software EMCEE (D. Foreman-Mackey et al. 2013). Before comparing to the data, all models are convolved with the wavelength-dependent line-spread function (LSF) of NIRSpec (P. Jakobsen et al. 2022). For JADES only, we use the LSF corrected for slit underfill in NIRSpec/MSA (A. Graaff et al. 2024). After this step, the model is integrated over each spectral pixel. To initialize the chains, we first identify the minimum-χ^2 solution using the specified model and ordinary least-squares minimization. We mask any spectral pixel deviating more than 3σ from the best-fitting model; this bad-pixel mask is saved and used later for the Bayesian estimate step. We estimate the uncertainties on this solution using the resulting Jacobian matrix. We use 140 chains initialized from truncated Gaussians, with mean equal to the minimum-χ^2 solution, and dispersion equal to twice the least-squares uncertainty. The truncation uses very generous bounds; we inspected the marginalized posterior probabilities after each fit, and increased the truncation bounds whenever a bound was within 3σ away from the median. The exception being when a physically motivated solution is being enforced (e.g. non-negative flux for forbidden emission lines, covering factors between 0 and 1). We run 10 000 steps for each chain, with 50 percent burn-in steps. All chains are concatenated and visually inspected for convergence. As fiducial parameters, we adopt the median and 16th–84th percentile range of the marginalized posterior. Hereafter, the fiducial model is always the MAP model.

3.3 High-resolution BlackTHUNDER spectrum – black-hole properties

For the properties of the SMBH, we rely on the high-resolution BlackTHUNDER $G395H$ data around Hβ–[O III]λλ4959,5007 and H α, using the ‘total’ elliptical aperture with $R_{ap} = 0.25$ arcsec. We use the Bayesian approach outlined in J24, but model simultaneously both line groups. The continuum is parametrized as two first-order polynomials in two windows centred at 3 and 4 μm (rest-frame 4935 and 6565 Å), requiring four free parameters. All narrow lines share the same redshift z_n and velocity dispersion σ_n (two free parameters); z_n is adopted as the spectroscopic redshift of the galaxy z_{spec}. We assume Gaussian velocity distributions, which for the range of velocities considered here, can be approximated as Gaussians in wavelength space too, as

$$f[v(\lambda)] = \frac{c}{\sqrt{2\pi}\,\sigma_n(1+z_n)\lambda_0(k)} \cdot \exp\left\{-\frac{1}{2}\left[\frac{c\,(\lambda-\lambda_0(k)\cdot(1+z_n))}{\sigma_n(1+z_n)\lambda_0(k)}\right]^2\right\}, \quad (1)$$

where λ is the observed wavelength and $\lambda_0(k)$ is the vacuum rest-frame wavelength of a given emission line (k = H β, [O III]λ4959, ...). The [O III]λλ4959,5007 and [N II] λλ6548,6583 doublets require 1 extra free parameter each (in addition to the shared redshift and velocity dispersion of the narrow lines; the doublet flux ratios are fixed to 0.335, see P. J. Storey & C. J. Zeippen 2000, and 0.327, see I. Dojčinović, J. Kovačević-Dojčinović & L. Č. Popović 2023, respectively). Narrow Hα and Hβ require two free parameters. Broad Hα emission requires two Gaussians; their common redshift is $(1 + z_n) \cdot \exp(v_b/c)$, parametrized by the velocity of the broad component v_b relative to the redshift of the narrow component. Their flux is parametrized by the total flux F_b (H α) and by the flux ratio $F_{b,1}/F_b$ (H α), while their FWHMs are free parameters, subject to $\mathrm{FWHM}_{b,1} < \mathrm{FWHM}_{b,2}$. Broad Hβ is also modelled as a double Gaussian, but is parametrized only with the flux ratio between H β and Hα, while all other parameters are tied to the broad Hα. The broad components require six free parameters. A simpler model using a single Gaussian is manifestly inadequate and is statistically disfavoured (we used the Bayesian information criterion, BIC, G. Schwarz 1978, and we obtain ΔBIC > 10; we find consistent results using the χ^2 distribution). As pointed out in F. D'Eugenio et al. (2025a), a double Gaussian model for the BLR is adopted as an effective line profile, without interpreting it as two SMBHs. For the broad-line Gaussians only, we also model the effect of a foreground $n = 2$ hydrogen absorber, using a geometric covering factor C_f and the optical-depth approach, with the residual intensity

at wavelengths λ given by

$$I(\lambda)/I_0(\lambda) = 1 - C_f + C_f \cdot \exp(-\tau(k;\,\lambda))$$
$$\tau(k;\,\lambda) = \tau_0(k) \cdot f[v(\lambda)], \quad (2)$$

where $I_0(\lambda)$ is the spectral flux density before absorption, $\tau_0(k)$ is the optical depth at the centre of the line (with k = H β or H α) and $f[v(\lambda)]$ is the velocity distribution of the absorbing atoms. The latter is approximated again using equation (1), with $\lambda_0(k) = \lambda_0$(H α), and replacing z_n and σ_n with $z_{abs}(v_{abs})$ and σ_{abs}, where v_{abs} and σ_{abs} describe the Gaussian velocity distribution of the absorbing gas. v_{abs} is related to the absorber redshift z_{abs} by $(1 + z_{abs}) \equiv (1 + z_n) \cdot \exp(v_{abs}/c)$, thus the velocity of the absorber is measured relative to the redshift of the narrow lines. The five free parameters for the absorption are C_f, τ_0(H β), and τ_0(H α) from equation (2), and v_{abs} and σ_{abs} from the equivalent of equation (1), giving a total of 21 free parameters in the model. We also model a broader component in [O III]λλ4959,5007 only, which adds three free parameters, the doublet velocity and velocity dispersion and the broad-[O III]λ5007 flux. In addition to the standard flat priors (Section 3.2), we also use three erfc priors. We penalize the narrow [N II] λ6583/Hα ratio against values higher than 1 (based on the very low detection rate of [N II] λλ6548,6583 at $z > 5$; A. J. Cameron et al. 2023). We also penalize the ratios σ_n/σ_{out} and F_{out}([O III]λ5007)/F_n([O III]λ5007) against values higher than 1, to avoid swapping the narrow-line flux with the much fainter broader [O III]λ5007 emission. Since none of these ratios can be negative, we normalize the erfc prior by its integral over the non-negative numbers.

The posterior parameters of the fit to the fiducial aperture spectrum are listed in column 1 of Table 2. In Fig. 5 instead, we show the data and fiducial model from the high-SNR aperture with $R_{ap} = 0.125$ arcsec. Compared to the $R_{ap} = 0.25$-arcsec aperture, this smaller aperture spectrum has biased emission-line ratios but offers higher SNR in the broad lines. The model correctly reproduces the shape of the emission lines, including the complex profile around Hβ and Hα. Broad Hβ emission is clearly present, with a 7σ detection (F_b (H β) $= 1.4 \pm 0.2 \times 10^{-18}$ erg s^{-1} cm^{-2}; Table 2, column 2), whereas the $R_{ap} = 0.25$-arcsec aperture yields only a 4σ result (Table 2, column 1), consistent with the expectations for an unresolved source. Fig. 5(c) shows χ, the data-minus-model residuals normalized by the noise (black line). The sand-coloured line highlights the systematically higher residuals when omitting the broad-Hβ component. Tentative Hβ absorption is also seen, with a slightly blueshifted centroid (inset panel). The broad [O III]λλ4959,5007 component is detected too, albeit only at the 5σ level, but is discussed more in detail in Section 3.5.

We detect a marginal blueshift of the broad Hα ($v_b = -45 \pm 9$ km s^{-1}), but this is driven by the large aperture, which may bias the narrow-line redshift estimate due to contamination from possible extended emission along the axis connecting 159717B to 159716 (Fig. 2). In agreement with this hypothesis, when repeating the fit for the 0.125-arcsec aperture (Table 2, column 2), we find indeed a lower systemic redshift (2σ significance) and, therefore, less blueshifted broad Hα ($v_b = -28 \pm 8$ km s^{-1}). There are some positive residuals at the spectral position of the narrow Hα line and at the blue wing of the Hα absorption. These residuals are not statistically significant, but they can be removed by decoupling the narrow Hα from the bluer narrow lines, and by introducing a second Hα absorber.

The Hα absorption has EW$_{abs}$ (H α) $= 6.9^{+0.5}_{-0.4}$ Å relative to the broad-line flux density. This value is deceptively small: the strength of the absorption can be fully appreciated when related to the broad-Hα equivalent width, EW(F_b (H α)) $= -1100$ Å, or when relating the absorption to the continuum (EW$_{abs}$ (H α) $= 190$ Å).

A selected subset of model parameters is shown in Fig. 8, showing that the *G395H* data can meaningfully constrain C_f and τ_0(H α), even though a strong degeneracy between these two parameters persists (as expected; e.g. R. L. Davies et al. 2024, J24). The velocity dispersion $\sigma_{abs} = 120 \pm 10$ km s^{-1} of the absorber is similar to other results reported in the literature (e.g. J24), but strikingly, the absorber velocity is remarkably low, $v_{abs} = -26^{+3}_{-4}$ km s^{-1}, statistically consistent with the velocity of the BLR ($v_b = -28 \pm 8$ km s^{-1}).

3.4 High-resolution JADES spectroscopy

The availability of JADES *G395H* spectroscopy enables us to test 159717 for time variability. We fit the *G395H* JADES data with the same approach as for the BlackTHUNDER *G395H* aperture data, with two differences. We remove the broad Hβ component, the Hβ absorber, and the broad [O III]λλ4959,5007 component, since we find no supporting statistical evidence for any of these features (five less free parameters than the model in the previous section), but we add the narrow [S II]λλ6716,6731 doublet, with free [S II] λ6716flux and doublet flux ratio (constrained to the physical range from R. L. Sanders et al. 2016, adding two more free parameters).

The resulting best-fitting model is shown in Fig. 6, while the percentiles of the posterior probabilities are in Table 2, column 3. Several parameters have different posterior probability distributions between JADES and BlackTHUNDER. The lack of broad [O III], broad Hβ, and H β absorption is consistent with the lower SNR of the JADES observations. The JADES data show clear detections of [S II] λλ6716,6731, but we discard these as unreliable (Section 3.6). JADES finds higher redshift $z_n = 5.07783 \pm 0.00002$ with high significance (11σ), but the redshift difference is only $\Delta z = 0.0003$, which corresponds to just one third of a spectral pixel at 4 μm, so the discrepancy could be due to systematics in the wavelength solution, which for sources smaller than the MSA microshutter depends on the intrashutter position – itself known only approximately. An error of this magnitude could be due to the bias between intrashutter position and wavelength solution in the JADES MSA data reduction (F. D'Eugenio et al. 2025d; see J. Scholtz et al. 2025a for a solution to this problem). We tested that decoupling the redshift of the spectral regions around Hβ–[O III]λλ4959,5007 from the redshift of the lines closest to Hα does not substantially improve the fit. The velocity dispersion is marginally different from BlackTHUNDER, with instrument-deconvolved $\sigma_n = 54 \pm 1$ km s^{-1} (2σ difference). Systematic uncertainties in the LSF may be responsible for this discrepancy. In fact, we assumed the LSF for point sources from A. Graaff et al. (2024), but in our case this choice likely overestimates the actual resolution, because while 159717 is compact, the narrow lines are spatially resolved (Section 3.1), so the effective resolution is intermediate between the nominal value assuming uniform slit illumination and the LSF for point sources. The JADES data have lower observed F_n (H β) $= (0.83 \pm 0.08) \times 10^{18}$ erg s^{-1} cm^{-2} (2σ significance). This small difference leads the model to infer higher dust attenuation, $A_V = 1.4^{+0.3}_{-0.2}$ mag, but this latter difference is not statistically significant (1.4σ). Lower narrow Hβ flux is consistent with the bias deriving from assuming point-source path-loss corrections in the JADES data reduction, which assume a higher flux loss at redder wavelengths, thereby potentially leading to a spurious increase in the Balmer decrement. These non-consequential differences have plausible explanations and overall do not affect our results.

Table 2. Posterior probabilities for key parameters of the emission-lines model. Our fiducial measurements use the BlackTHUNDER 0.25-arcsec aperture, which ensures accurate line ratios across the wavelength range. This accuracy comes at the cost of lower SNR, as evidenced by the higher SNR in some lines (e.g. F_b (H β) goes from 4σ to 7σ detection when restricting the aperture to 0.125 arcsec). Parameters in square brackets in column (4) are constrained using priors from the the posterior of the *G395H* model.

Survey Aperture Disperser Parameter	Fit	Unit	BlackTHUNDER $R_{ap}=0.25$ arcsec *G395H* (1)	BlackTHUNDER $R_{ap}=0.125$ arcsec *G395H* (2)	JADES MSA *G395H* (3)	JADES MSA *G235M* and *G395M* (4)
F_n([O II]λ3726)	Y	10^{-18} erg s^{-1} cm^{-2}	–	–	–	$0.32^{+0.05}_{-0.04}$
F_n([O II]λ3729)/F_n([O II]λ3726)	Y	–	–	–	–	$1.1^{+0.2}_{-3}$
F_n([Ne III]λ3869)	Y	10^{-18} erg s^{-1} cm^{-2}	–	–	–	$0.48^{+0.06}_{-0.07}$
F_n (H γ)[a]	Y	10^{-18} erg s^{-1} cm^{-2}	–	–	–	$0.35^{+0.04}_{-0.04}$
F_n([O III]λ4363)	Y	10^{-18} erg s^{-1} cm^{-2}	–	–	–	$0.23^{+0.06}_{-0.06}$
F_n (H β)[a]	Y	10^{-18} erg s^{-1} cm^{-2}	$1.08^{+0.06}_{-0.06}$	$0.88^{+0.05}_{-0.05}$	$0.90^{+0.08}_{-0.08}$	$0.93^{+0.07}_{-0.07}$
F_n([O III]λ5007)	Y	10^{-18} erg s^{-1} cm^{-2}	$8.2^{+0.3}_{-0.4}$	$6.5^{+0.3}_{-0.4}$	$8.0^{+0.1}_{-0.1}$	$7.3^{+0.1}_{-0.1}$
F_n (H α)	Y	10^{-18} erg s^{-1} cm^{-2}	$4.5^{+0.2}_{-0.2}$	$3.6^{+0.2}_{-0.2}$	$4.3^{+0.2}_{-0.2}$	$4.2^{+0.2}_{-0.2}$
F_n([N II]λ6583)	Y	10^{-18} erg s^{-1} cm^{-2}	< 0.15	< 0.1	< 0.15	(< 0.2)
F_n([S II]λ6716)	Y	10^{-18} erg s^{-1} cm^{-2}	–	–	–[b]	(< 0.06)
A_V [a]	N	mag	$1.0^{+0.2}_{-0.2}$	$1.0^{+0.2}_{-0.1}$	$1.4^{+0.3}_{-0.2}$	$1.2^{+0.2}_{-0.2}$
$A_{V,b}$	N	mag	$4.4^{+0.7}_{-0.5}$	$4.8^{+0.5}_{-0.4}$	–	–
σ_n	Y	km s^{-1}	49^{+2}_{-2}	47^{+2}_{-2}	54^{+1}_{-1}	69^{+3}_{-3}
z_n	Y	—	$5.07753^{+0.00002}_{-0.00002}$	$5.07747^{+0.00002}_{-0.00002}$	$5.07783^{+0.00002}_{-0.00002}$	$5.07785^{+0.00004}_{-0.00004}$
F_{out}([O III]λ5007)	Y	10^{-18} erg s^{-1} cm^{-2}	$1.6^{+0.4}_{-0.3}$	$1.5^{+0.4}_{-0.3}$	–	–
v_{out}	Y	km s^{-1}	-20^{+10}_{-20}	-29^{+10}_{-12}	–	–
σ_{out}	Y	km s^{-1}	130^{+20}_{-20}	120^{+20}_{-20}	–	–
v_b	Y	km s^{-1}	-45^{+9}_{-9}	-28^{+7}_{-8}	-20^{+10}_{-10}	-10^{+7}_{-7}
F_b (H β)/F_b (H α)	Y	–	$0.06^{+0.01}_{-0.01}$	$0.055^{+0.009}_{-0.010}$	–	–
F_b (H β)[c]	N	10^{-18} erg s^{-1} cm^{-2}	$1.6^{+0.4}_{-0.4}$	$1.4^{+0.2}_{-0.2}$	–	–
F_b (H α)[c]	Y	10^{-18} erg s^{-1} cm^{-2}	$25.9^{+0.6}_{-0.6}$	$25.8^{+0.5}_{-0.4}$	$29.8^{+0.8}_{-0.8}$	$27.4^{+0.3}_{-0.3}$
$F_{b,1}/F_b$ (H α)	Y	–	$0.39^{+0.07}_{-0.07}$	$0.37^{+0.03}_{-0.03}$	$0.35^{+0.02}_{-0.02}$	$0.47^{+0.05}_{-0.05}$
FWHM$_{b,1}$ (H α)	Y	km s^{-1}	1300^{+100}_{-100}	1330^{+80}_{-80}	1100^{+70}_{-70}	1550^{+100}_{-100}
FWHM$_{b,2}$ (H α)	Y	km s^{-1}	3200^{+300}_{-200}	3200^{+100}_{-100}	3400^{+200}_{-100}	3900^{+200}_{-200}
FWHM$_b$ (H α)	N	km s^{-1}	1740^{+80}_{-90}	1790^{+60}_{-60}	1490^{+80}_{-80}	1920^{+70}_{-60}
v_{abs}	Y	km s^{-1}	-34^{+5}_{-5}	-26^{+4}_{-4}	-13^{+5}_{-4}	$[-6^{+7}_{-7}]$
σ_{abs}	Y	km s^{-1}	98^{+8}_{-7}	103^{+6}_{-6}	108^{+8}_{-8}	$[84^{+7}_{-6}]$
C_f	Y	–	$0.94^{+0.04}_{-0.08}$	$0.90^{+0.07}_{-0.12}$	$0.95^{+0.03}_{-0.06}$	$[0.96^{+0.03}_{-0.04}]$
τ_0(H β)	Y	–	20^{+7}_{-8}	7^{+6}_{-3}	–	–
τ_0(H α)	Y	–	$2.2^{+0.6}_{-0.4}$	$2.0^{+0.6}_{-0.4}$	$3.1^{+0.7}_{-0.5}$	$[2.7^{+0.3}_{-0.3}]$
EW$_{abs}$ (H β)	N	Å	$9.2^{+0.7}_{-0.9}$	$8.0^{+1.0}_{-1.1}$	–	–
EW$_{abs}$ (H α)	N	Å	$6.6^{+0.5}_{-0.4}$	$6.7^{+0.7}_{-0.5}$	$8.3^{+0.5}_{-0.4}$	–
$T_e(O^{2+})$	N	10^4 K	–	–	–	$2.1^{+0.4}_{-0.3}$
$T_e(O^+)$	N	10^4 K	–	–	–	$1.8^{+0.3}_{-0.2}$
$n_e(O^+)$	N	cm^{-3}	–	–	400^{+700}_{-300}	
$12+\log(O^{2+}/H^+)$	N	dex	–	–	–	$7.5^{+0.2}_{-0.1}$
$12+\log(O^+/H^+)$	N	dex	–	–	–	$6.8^{+0.2}_{-0.2}$
$12+\log(O/H)$	N	dex	–	–	–	$7.6^{+0.2}_{-0.1}$
$\log(M_\bullet/M_\odot)_{A_V}$	N	dex	$7.65^{+0.05}_{-0.05}$	$7.68^{+0.04}_{-0.04}$	$7.60^{+0.06}_{-0.07}$ (±0.3)	–
$\log(M_\bullet/M_\odot)_{A_{V,b}}$	N	dex	$8.14^{+0.11}_{-0.10}$	$8.24^{+0.08}_{-0.07}$	–	–

Notes. Note the dependence of dust attenuation on the aperture size used. The JADES NIRSpec/MSA grating spectra have been downscaled by 0.85 to match the line fluxes of BlackTHUNDER and of the JADES prism. [a]For the medium-gratings only, we fix the intrinsic flux ratio between the narrow Balmer lines and apply a dust attenuation. Hence, for this fit, A_V is a free parameter, while the F_n (H γ) and F_n (H β) are not.
[b][S II] λ6716 and [S II]λ6731 are formally detected at 6σ and 5σ in the JADES G395H data, but not in the other configurations (and fall in the detector gap in the BlackTHUNDER *G395H* data). We interpret the observed signal as spectral overlap from other sources (Section 3.6).
[c]For the flux of the BLRs, we report the flux before the Balmer absorber.

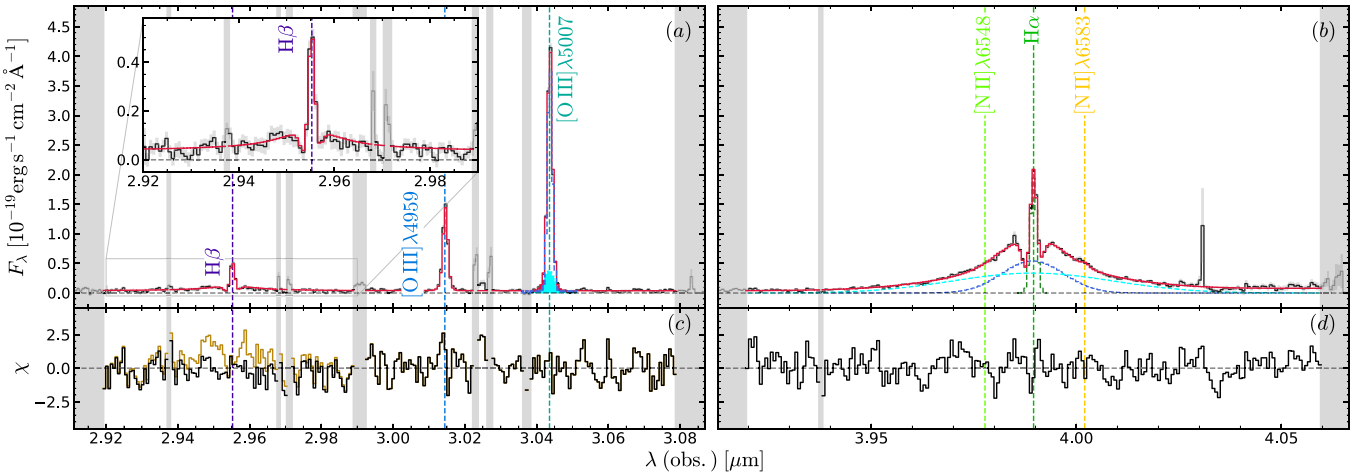

Figure 5. BlackTHUNDER *G*395*H* $R_{ap} = 0.125$-arcsec aperture spectrum (black line), with the best-fitting model overlaid in red. Grey vertical strips mark either spectral regions outside of the fitted range or pixels affected by masked outliers (Section 3.2). In the bottom panels, we show the fiducial χ residuals (black line) and the residuals of the disfavoured model without a broad Hβ component (sand-coloured line). The blue line and filled cyan curve in panel (a) show the two components (narrow and broad) of the [O III]λ5007 emission line; similarly, the dashed lines in panel (b) show the individual emission components of Hα (without absorption).

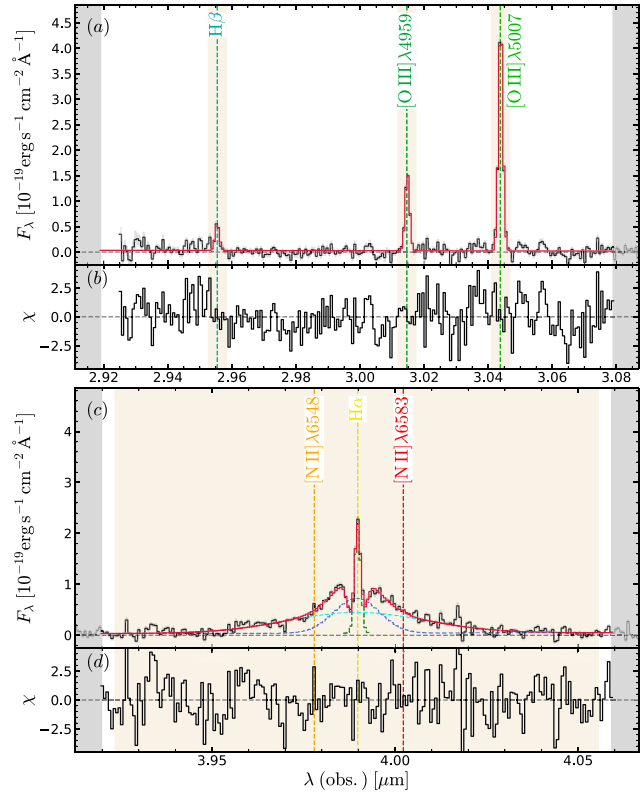

Figure 6. JADES *G*395*H* aperture spectrum (black line), with the best-fitting model overlaid in red. Grey vertical bands are not included in the fit, while sand-coloured bands are the regions we used to calculate the BIC value and to compare different models (Section 3.4). In the bottom panels, we show the χ residuals.

However, there are two important mismatches. The FWHM of the broad-Hα line is $\mathrm{FWHM_b}$ (H α) $= 1490 \pm 80$ km s^{-1} for JADES and 1790 ± 60 km s^{-1} for BlackTHUNDER (a 3σ discrepancy). This 20 per cent difference alone propagates to an error on the SMBH mass of 45 per cent (Section 4.1), only marginally reduced by the 14 per cent larger Hα flux in JADES than in BlackTHUNDER. This flux difference (4σ) reflects the difficulty of inferring the emitted Hα flux in the presence of strong absorption (τ_0(H α) $= 3.1^{+0.7}_{-0.5}$).

3.5 Ionized outflows

The broad [O III]λλ4959,5007 component (shown separately by the filled cyan line under [O III]λ5007 in Fig. 5a) is clearly much broader than the narrow lines, yet significantly narrower than the broad Balmer lines. It is not detected in JADES (ΔBIC = 6), while the deeper BlackTHUNDER data favours multiple components, with an improvement of ΔBIC = 21 for the double-component model over the single-component model.

According to the BlackTHUNDER data, both [O III]λλ4959,5007 components are kinematically narrow ($\sigma_{out} = 140 \pm 20$ km s^{-1} versus $\sigma_n = 50 \pm 2$ km s^{-1}) and they are consistent with the same systemic velocity (velocity offset $\delta v = -20^{+10}_{-20}$ km s^{-1}). The narrowest component is the brightest, with an [O III]λ5007 flux of $8.3^{+0.3}_{-0.4} \times 10^{-18}$ erg s^{-1} cm^{-2}, while the broad component has flux F_{out}([O III]λ5007) $= 1.5^{+0.4}_{-0.3} \times 10^{-18}$ erg s^{-1} cm^{-2} (5σ significance). The significance does not change with aperture size, suggesting a spatially resolved nature. However, the SNR is too low for detecting the broader component in individual spaxels, hence we omit it from the spatially resolved analysis (Section 5).

Repeating the deblending analysis performed on [O III]λ5007 for Hα and Hβ is not possible due to degeneracies with the absorption profile shape and, in the case of Hβ, the low SNR. Given this lack of information, it is impossible to provide a physical interpretation of the two components. We present three simple scenarios. The narrowest component may be tracing the host galaxy, while the broadest component is due to tidally disrupted material following the interaction with one or more satellites (Section 5). Alternatively, if the broadest component traces the host galaxy, then the narrowest component could be either a star-forming clump, or gas photoionized by the AGN. Faint outflows are also a possibility, with an outflow velocity that can be estimated (D. S. Rupke, S. Veilleux & D. B. Sanders 2005; S. Veilleux, G. Cecil & J. Bland-Hawthorn 2005) as $|v_{out}| + 2 \cdot \sigma_{out} = 300$ km s^{-1}, in agreement with the values found in star-forming galaxies at $z > 4$ (S. Carniani et al. 2024). The possible

detection of a localized outflow resonates with the finding of the detached outflow component 159717C (Sections 5.1 and 5.3).

3.6 Absence of nitrogen, sulphur, and helium

Near H α, we find no evidence for [N II] $\lambda\lambda$6548,6583 and [SII] $\lambda\lambda$6716,6731, as expected from the generally low detection rate of these lines at $z > 5$ (A. J. Cameron et al. 2023; S. Mascia et al. 2024; I. Juodžbalis et al. 2025; F. D'Eugenio et al. 2025d). Performing the inference while including [N II] $\lambda\lambda$6548,6583 (with the same redshift and intrinsic dispersion as the other narrow lines) yields a 3σ upper limit on the [N II] λ6583 flux < 0.1–0.15×10^{-18} erg s^{-1} cm^{-2} (depending on the survey and aperture considered). For [S II] λ6716 and [S II]λ6731, the JADES *G395H* fit yields 6σ and 5σ detections, respectively. The nominal fluxes are $(0.36 \pm 0.06)\times 10^{-18}$ and $(0.31 \pm 0.05)\times10^{-18}$ erg s^{-1} cm^{-2}, with a plausible doublet ratio of 1.2. The BlackTHUNDER G395H data cannot confirm this detection, because at the position of 159717, the doublet falls in the detector gap. However, neither of these two lines are confirmed in the medium-resolution grating or in the prism (even though the low spectral resolution of the prism is expected to increase the SNR of the doublet). Besides, [S II]λ6731 is very near some noise features. Therefore, we dismiss the signal observed in *G395H* as an artefact. Similarly, we find no evidence for HeI I, in agreement with similar findings in other LRDs (see e.g. the objects included in the AGN sample of I. Juodžbalis et al. 2025).

3.7 Other tests and model parameters

Using *G395H* data from both JADES and BlackTHUNDER, we tested the impact of wavelength-calibration issues on the recovered parameters. We repeated the Bayesian inference by decoupling the Hβ and [O III]$\lambda\lambda$4959,5007 region of the spectrum from Hα. This was done by introducing a new free parameter for the line broadening of the narrow Hβ and [O III]$\lambda\lambda$4959,5007 lines ($\sigma_{\rm n,\,blue}$) and a velocity offset $v_{\rm n,\,blue}$ between this set of narrow lines and narrow Hα. The marginalized posterior on $\sigma_{\rm n,\,blue}$ is 10 per cent larger than $\sigma_{\rm n}$, suggesting that our LSF characterization does not fully capture the instrument performance. For $v_{\rm n,\,blue}$, we find either no offset (for JADES, $v_{\rm n,\,blue} = 10 \pm 10$ km s^{-1}), or a 4σ offset of Hβ and [O III]$\lambda\lambda$4959,5007 towards the blue (for BlackTHUNDER, $v_{\rm n,\,blue} = -6.1 \pm 1.5$ km s^{-1}). In both cases, there is a strong correlation between $v_{\rm n,\,blue}$ and the velocity of the absorber, which propagates to other physical quantities like C_f and τ_0. This is understandable, because a velocity offset of the absorber can shift the peak of the narrow-Hα line. The exact effect on C_f and $v_{\rm abs}$ is complicated by the interdependence of these two quantities. However, for EW$_{\rm abs}$ (H α), using a free $v_{\rm n,\,blue}$ (as opposed to $v_{\rm n,\,blue} = 0$ in the fiducial models) leads to changes in the EW measurement of 10 per cent.

3.8 Importance of high-resolution *JWST* spectroscopy

To evaluate the bias of our measurements for different dispersers, we repeat the above modelling analysis on the medium-resolution JADES data, with spectral resolution $R = 700$–1500, and with a mock realization of NIRCam/WFSS (Wide Field Slitless Spectroscopy) *F444W* data. Besides differences in the data and LSF, the models are identical. However, for the NIRCam mock spectrum, we exclude the model and data near Hβ and [O III]$\lambda\lambda$4959,5007, because these would not be normally available. We do not correct for the generally higher noise of the NIRCam slitless spectroscopy. The comparison between the high- and medium-resolution NIRSpec/MSA spectroscopy is shown in Fig. 7 (for NIRCam/WFSS, see

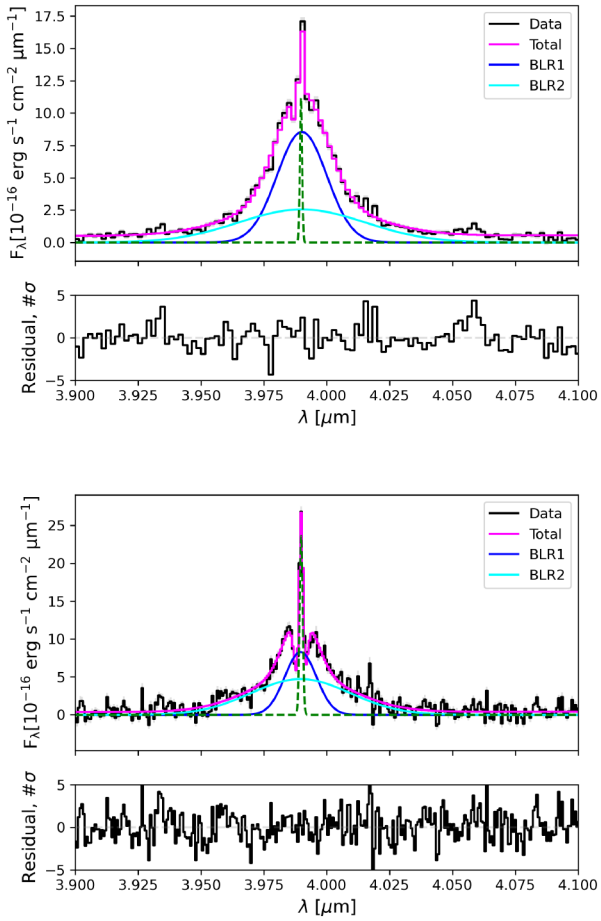

Figure 7. Medium- and high-resolution JADES spectra of 159717, highlighting how *G395M* (panel a) can completely miss an absorber with τ_0(H α) = 3.

Appendix D). The contrast between panels (a) and (b) is stark. In the medium-resolution data, there is almost no trace and certainly no statistical evidence of Hα absorption. For the NIRCam mock data, the presence of the absorber is still clear (Appendix D), and its physical properties C_f and τ_0(H α) are reasonably well constrained (Fig. 8), though these constraints may stem from an unreasonably good data quality, which would require very long integration for NIRCam/WFSS. However, even the best-quality NIRCam/WFSS data cannot constrain well the kinematic properties of the absorber, with 5× larger uncertainties. From here on, we adopt the high-resolution *G395H* model as the fiducial model for deriving the galaxy redshift, the narrow-line velocity dispersion, and the SMBH parameters.

3.9 Dust attenuation

The dust attenuation in 159717 consists of an intrinsic component, and a foreground screen due to the interloper 159715. In principle, we should distinguish between the intrinsic and foreground terms. In practice, the dust attenuation from the interloper is negligible (Appendix A), due to a combination of low intrinsic attenuation in the interloper and to the fact that the optical emission lines from 159717 are already at observed-frame 1 μm when they pass through 159715 at $z \sim 1$. For the main analysis, we assume the K. D. Gordon et al. (2003, hereafter: G03) attenuation law, parametrized by the V-band attenuation A_V and expressed as a spline interpolating the data presented in G03. To infer A_V, we compare the Balmer decrement F(H α)/F(H β) to the assumed intrinsic ratio.

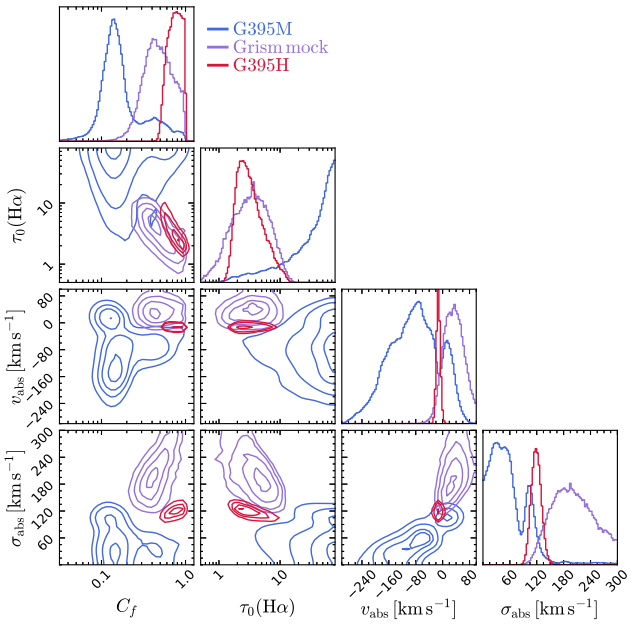

Figure 8. Posterior probability distribution of the Hα model, showing the different constraining power of the NIRSpec medium-resolution data (blue; *G395M*), of the NIRCam/WFSS grisms (purple; grism mock), and of the high-resolution NIRSpec data (red; *G395H*). At a resolution of $R = 1000$, *G395M* is unable to constrain the absorber, and even at $R = 1600$ (corresponding to NIRCam/WFSS), the physical properties of the absorber may be biased. With NIRSpec and *G395H*, we can measure the velocity of the absorber with high precision, showing that it is very close to the galaxy rest frame.

For the galaxy interstellar medium (ISM), we use the narrow-line fluxes measured from the fiducial BlackTHUNDER aperture, where bias due to aperture losses is minimal. We assume Case-B recombination, electron temperature $T_{\rm e} = 10\,000$ K, and electron density $n_{\rm e} = 500\,{\rm cm}^{-3}$ giving H $\alpha/{\rm H}\ \beta = 2.86$ (D. E. Osterbrock & G. J. Ferland 2006). In the fiducial aperture, we find an effective dust-attenuation value $A_V = 1.0 \pm 0.2$ mag (Table 2, column 1). The smaller $R_{\rm ap} = 0.125$-arcsec aperture instead yields 1.3 ± 0.2 mag. While these two values are statistically consistent, the higher attenuation in the smallest aperture suggests that the larger aperture captures additional narrow-line emission for which our aperture correction is inadequate (based as it is on the curve of growth of the broad-Hα line, which is a point source). Alternatively, the innermost region may suffer from higher dust attenuation relative to the outskirts. Assuming a higher intrinsic Hα/Hβ ratio of 3.10 would revise A_V down by 0.21 mag.

As we have noted, A_V is an equivalent dust attenuation, which includes reddening in 159717, as well as additional reddening due to crossing the interloper 159715 at $z_{\rm spec} = 1.001$. This latter reddening is hard to estimate accurately, because we do not detect Hβ in the foreground star-forming regions. We detect either the spectrally blended Hβ–[O III]λλ4959,5007 complex (in the prism), or just [O III]λ5007 (in the *G140M* grating). Flux calibration uncertainties between the NIRSpec dispersers are of the same order of magnitude as the effect of moderate dust attenuation (F. D'Eugenio et al. 2025d), so we do not attempt to infer Hβ by subtracting the grating [O III]λλ4959,5007 flux from the Hβ–[O III]λλ4959,5007 blend in the prism. A physically motivated fit of the interloper spectrum finds $A_V = 0.4^{+0.7}_{-0.3}$, and is thus consistent with no dust attenuation (Appendix A). We thus do not attempt to break down A_V, the effective dust attenuation in 159717, into a local and a foreground component.

For the BLR, we find a Balmer decrement of 15^{+5}_{-3}. Estimating the attenuation towards the BLR is highly uncertain, because in the high-density BLR, the Balmer lines can be powered by other processes such as collisional excitation. Assuming an intrinsic ratio of 3.06 (from observations of blue quasars; X. Dong et al. 2008), we obtain $A_{V,\rm b} = 4.4^{+0.7}_{-0.5}$ mag, which would imply an intrinsic Hα flux 25 times brighter than what we measure. Such a high attenuation may be at odds with the reported weakness of LRDs at MIR (mid-infrared) wavelengths (C. C. Williams et al. 2024; A. Graaff et al. 2025; B. Wang et al. 2025; H. B. Akins et al. 2025c).

On the other hand, an intrinsic Balmer ratio of 10 (D. Ilić et al. 2012) would give a dust attenuation $A_{V,\rm b} = 1.2$ mag, fully consistent with the dust attenuation inferred from the narrow-line ratios and implying no additional dust towards the BLR.

3.10 Medium-resolution spectrum – host-galaxy ISM

To derive the physical properties of the host galaxy, we use the medium-resolution spectra, because they cover the full range of rest-optical strong lines, unlike high-resolution *G395H* spectroscopy. We detect no line emission in the *G140M* spectrum (except for rest-frame optical lines from the interloper, Appendix A), so we use only the *G235M* and *G395M* spectra. We define four spectral windows around [O II]λλ3726,3729 and [Ne III] λ3869, Hγ and [O III]λ4363, Hβ and [O III]λλ4959,5007, and Hα, and we use a joint model to fit the spectrum simultaneously in each window (Fig. 9). The background is modelled piecewise inside each window as a first-order polynomial (two free parameters per window, eight total). The narrow lines are all modelled with the same redshift $z_{\rm n}$ and intrinsic velocity dispersion $\sigma_{\rm n}$ (two free parameters). All lines are parametrized via their dust-corrected flux, requiring one free parameter for the G03 dust attenuation. This approach models simultaneously the entire spectrum (similar to J. E. Greene et al. 2024), and ensures a Bayesian approach to estimate the dust attenuation. [O II]λλ3726,3729 is parametrized by the [O II]λ3726 flux and the [O II]λ3729/[O II]λ3726 ratio (two free parameters; the doublet ratio is constrained to the range 0.3839–1.4558, following R. L. Sanders et al. 2016). [O III]λ4363 and [O III]λ5007 are parametrized via their flux, whereas the flux of [O III]λ4959 is fixed to 0.335 the [O III]λ5007 flux (two free parameters).

The narrow-component Balmer lines Hγ, Hβ, and Hα are parametrized via the Hα flux alone (one free parameter). The fluxes of Hβ and Hγ are fixed to their Case-B recombination ratios with respect to Hα, where we assumed $T_{\rm e} = 10\,000$ K and $n_{\rm e} = 500$ cm^{-3} These values are justified as follows; for the density, we use the mean density of star-forming galaxies at $z \approx 5$ (Y. Isobe et al. 2023); *a posteriori*, this value is not inconsistent with the mean value we infer from the measured [O II]λ3729/[O II]3726 ratio (although the uncertainties are very large). The impact of this density choice on our model is in any case small; for example, the mean density of narrow-line AGN in the local Universe is found to be significantly higher, when estimated from higher ionization species ($n_{\rm e} = 10\,000$–$30\,000$ cm^{-3}; L. Binette et al. 2024), but even at these higher densities the Hα/Hβ and Hγ/Hβ ratios changes by less than 2 per cent. W. McClymont et al. (2025a) reported the discovery of galaxies at $z > 4$ with observed Balmer-line ratios which are inconsistent with Case-B recombination. However, these galaxies seem associated with density-bounded nebulae, and tend to exhibit blue continuum and Lyα emission, contrary to what we observe here. For the temperature, we reason that regions of higher temperature (as those producing auroral [O III]λ4363 emission) have lower Balmer-line emissivity, as highlighted by the anticorrelation between [O III]λ5007/H β and [O III]λ4363/[O III]λ5007 in the narrow-line

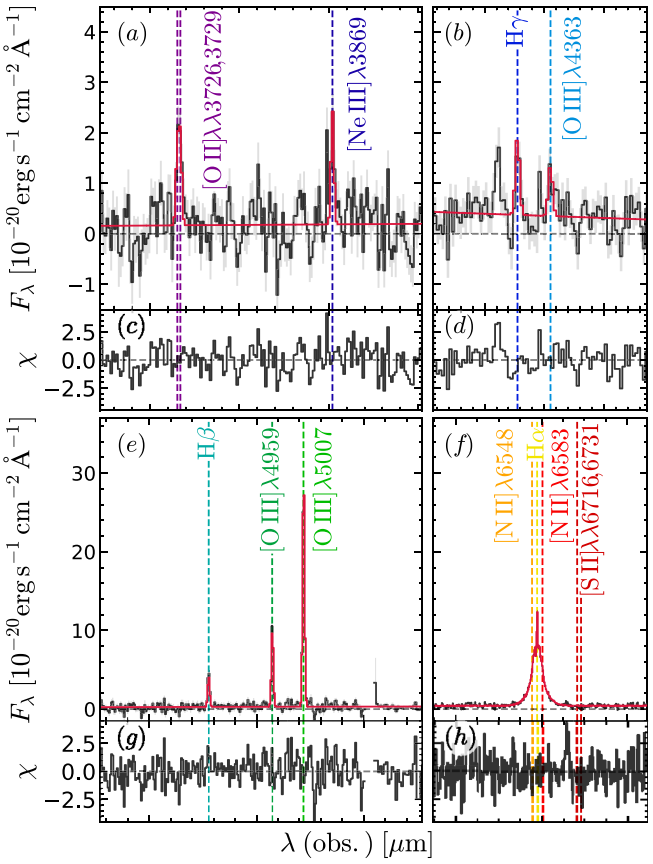

Figure 9. Piecewise fit of the medium-resolution spectroscopy for 159717, showing the region around [O II]λλ3726,3729 and [Ne III] λ3869 (panel a), around Hγ and [O III]λ4363 (panel b), H β and [O III]λλ4959,5007 (panel e), and Hα (panel f). Panels (c), (d), (g), and (h) show the model residuals normalized by the noise. All narrow lines are modelled assuming the same redshift z_n and intrinsic dispersion σ_n. The Balmer lines Hγ and Hβ are modelled assuming fixed ratios to Hα, and a K. D. Gordon et al. (2003) dust attenuation. Note that this model includes an unresolved Hα absorber near rest frame, with informative priors derived from modelling the *G395H* data. Including this absorber has a strong impact (> 0.5 mag) on the recovered dust attenuation A_V. All lines are seen in the 2D spectrum.

regions of type 1 AGN (A. Baskin & A. Laor 2005); therefore, the overall Balmer ratio should be biased towards lower temperature regions. In any case, also the assumptions on T_e do not have a major impact on our findings.

Four more narrow lines are included: [N II] λλ6548,6583 and [S II] λλ6716,6731; these are parametrized by three free parameters as in Section 3.3. Based on the fit residuals, the only clearly detected broad-line component is that of Hα, which is modelled in the same way as for the *G395H* data (Section 3.3), using two Gaussians and five free parameters. Finally, we add the Hα absorber, with its four free parameters. In total, this model has 28 free parameters, 11 for the narrow lines, 5 for the broad Hα, 4 for the absorber, and 8 for the local background. Given that these data are unable to constrain the properties of the absorber (Section 3.8), for the four free parameters describing the absorber we adopt informative priors based on the 1D marginalized posterior probabilities from the *G395H* model inference from JADES (Table 2, column 3), without considering the covariance in the posterior probability. We broaden these posteriors by a factor of two (we use a lognormal for C_f and τ_0(H α)). The goal of this setup is to capture the uncertainty in the narrow-line flux due to poorly constrained absorption, while still adopting a physically motivated range of absorber properties.

The resulting properties from the above model are reported in Table 2 (column 4). These measurements are the basis for our analysis of the galaxy ISM. To avoid confusion, we do not use the posterior for the broad-Hα and absorber parameters; these model components are included only to obtain an unbiased flux of the narrow Hα and of the dust attenuation. For analysing the broad component, we used the *G395H* data (Section 3.3; Table 2, column 2).

From the medium gratings, we obtain a dust attenuation $A_V = 1.2 \pm 0.2$ mag, lower than the value inferred from the *G395H* spectrum ($A_V = 1.4^{+0.3}_{-0.2}$ mag; Table 2). The main result of our joint fit to the Balmer lines is to upweight the Hγ/Hβ ratio in the estimate of the dust attenuation, yielding a higher value compared to fitting the lines separately and then estimating A_V (a method that yields $A_V = 0.9 \pm 0.2$ mag). Our high attenuation values are not implausible, given the red slope of the rest-optical continuum (e.g. Figs 1c and 9), and other reported measurements of A_V in the literature (L. J. Furtak et al. 2024; M. Killi et al. 2024; X. Ji et al. 2025; H. B. Akins et al. 2025b), including from narrow lines (M. Brooks et al. 2025; F. D'Eugenio et al. 2025a). The uncertainties are large, correctly reflecting the uncertainties in the properties of the absorber (which in our case are informed by the results of the *G395H* fit).

Including the known absorber is essential for recovering unbiased emission-line properties. For instance, removing the absorber altogether from the model leads to severely underpredicting the narrow Hα flux; with our physically motivated model we obtain F_n(H β) and F_n(H α) of $(0.53 \pm 0.03) \times 10^{-18}$ and $(1.55 \pm 0.08) \times 10^{-18}$ erg s^{-1} cm^{-2}, respectively. This yields a dust attenuation $A_V = 0.07 \pm 0.03$ mag, consistent with no dust and much lower than the true value. In fact, the Hα flux is so severely underestimated that the model underpredicts Hβ too, since our model enforces a minimum Balmer decrement of 2.86. Removing this constraint, we would obtain an unphysical Balmer decrement of 1.5.

4 PHYSICAL PROPERTIES

4.1 The supermassive black hole

From the *G395H* Hα model of the fiducial $R_{ap} = 0.25$-arcsec BlackTHUNDER spectrum (Section 3.3), we obtain a BLR FWHM $= 1740^{+80}_{-90}$ km s^{-1} (Table 2, column 1). The best-fitting value for the higher SNR $R_{ap} = 0.125$-arcsec spectrum has smaller uncertainties but is fully consistent (FWHM $= 1790 \pm 60$ km s^{-1}; column 2). We use the larger aperture because it minimizes aperture-loss corrections, ensuring the highest accuracy in the inferred dust attenuation. The absorption-corrected Hα luminosity is $7.3 \pm 0.2 \times 10^{42}$ erg s^{-1}, increasing to $15 \pm 2 \times 10^{42}$ erg s^{-1} after correcting for dust attenuation using $A_V = 1.0 \pm 0.2$ mag (for all derived quantities, we calculate the uncertainties from the MCMC chains, in the same way as the posterior probability on the other model parameters). We assume virial equilibrium, and use the single-epoch black-hole mass estimator of A. E. Reines & M. Volonteri (2015), appropriate for SMBHs at the low-mass end of the calibration. This gives $\log M_\bullet/M_\odot = 7.65 \pm 0.05$ (7.50 ± 0.04 without dust correction), dominated by uncertainties in the calibration, of order 0.3 dex.

Alternatively, instead of applying a dust-attenuation correction based on the Balmer decrement of the narrow-line region, we can apply the higher attenuation inferred from the Balmer decrement of the BLR. We estimate a maximum value of $A_{V,b} = 4.4^{+0.7}_{-0.5}$ mag, giving a broad Hα luminosity of $1.7^{\times 1.6}_{\div 1.5} \times 10^{44}$ erg s^{-1}. With this

much higher luminosity, we get $\log M_\bullet/\mathrm{M}_\odot = 8.1 \pm 0.1$, which we treat as an upper limit on the SMBH mass, due to the large range of possible intrinsic Balmer ratios for BLRs (X. Dong et al. 2008; D. Ilić et al. 2012; see Section 3.9). Recently, joint measurements of broad Hα, Hβ, and Hγ in a $z = 6.68$ LRD have shown observed ratios that are inconsistent with standard attenuation laws (G. P. Nikopoulos et al. 2025; F. D'Eugenio et al. 2025b), which would invalidate our maximal $A_V = 4.4$ mag. This scenario may be actually quite common, because LRDs – including 159717 –t end to have remarkably large Hα/Hβ.

To obtain the bolometric luminosity, we use the calibration of J. Stern & A. Laor (2012) based on Hα. The resulting Eddington ratio is $\lambda_\mathrm{E} = 0.35$ (0.24 without dust-attenuation correction). For the extreme case of a highly obscured BLR, we would estimate $\lambda_\mathrm{E} = 1.4$, driven by the fact that (with our single-epoch $M_\bullet$ calibration and for fixed FWHM), we have approximately $\lambda_\mathrm{E} \propto \sqrt{F_\mathrm{b}(\mathrm{H}\ \alpha)}$.

There is also the possibility that the double-Gaussian profile is due to two SMBHs; dual AGNs have already been reported (e.g. R. Maiolino et al. 2024; H. Übler et al. 2024, 2025) and their rate is more common at high redshift, at least on kpc scales (M. Perna et al. 2025). However, while 'double-Gaussian' profiles are widespread among LRDs (e.g. I. Juodžbalis et al. 2025), there is currently very little evidence for kinematic offsets between the two broad-line components. At plausible separations of 1–100 pc, the orbital velocity of two SMBHs with mass comparable to 159717 would range between 60–600 km s^{-1}; admittedly our observations cannot fully constrain the low-velocity envelope of this range, due to the difficulty of measuring a velocity offset that is small compared to the line widths, without even considering inclination effects or the complication of the narrow line and Hα absorber. However, while some confirmed cases do have small velocity offsets (e.g. H. Übler et al. 2024, $\delta v = 40$ km s^{-1}), the general paucity of larger offsets seems to be a problem for the double-SMBH interpretation.

An alternative interpretation is that the broad Balmer lines are shaped by electron scattering, not virial motions (V. Rusakov et al. 2025). This scenario is discussed in Section 6.1, but the relevant profile fits and calculations are reported in Appendix E.

4.2 The host galaxy

We do not attempt to measure the stellar mass of 159717. The usual uncertainties about the stellar mass of LRDs (B. Wang et al. 2024, 2025; J24; D. J. Setton et al. 2025a; Y. Ma et al. 2025b) are compounded by the presence of 159715 and of its UV-bright spiral arm (Fig. 2). Besides, two other LRDs have been confirmed to have time-variable[1] rest-frame optical continuum (X. Ji et al. 2025; R. P. Naidu et al. 2025), implying that the AGN dominates the optical continuum, from which stellar masses are usually inferred. With the interloper contaminating the UV, we have no handle on the stellar SED.

Assuming virial equilibrium, we can estimate the galaxy dynamical mass from the galaxy size and from the narrow-line width, following the approach outlined in H. Übler et al. (2023) and R. Maiolino et al. (2024). We adopt the calibration of A. der Wel et al. (2022), with Sérsic index $n = 4.5$, projected axis ratio $q = 0.44$, and $R_\mathrm{e} = 210$ pc (Table 1). We correct the observed narrow-line velocity dispersion $\sigma_\mathrm{n} = 49 \pm 2$ km s^{-1} upward by 0.2 dex, following the calibration of R. Bezanson et al. (2018) that converts gas velocity dispersions to stellar values. With these numbers, we obtain $\log(M_\mathrm{dyn}/\mathrm{M}_\odot) = 9.1$ dex, which we also use as an upper limit on the stellar mass. The large uncertainties on q and R_e translate into uncertainties on M_dyn of order 0.1 dex. For comparison, the virial calibration from J. P. Stott et al. (2016) gives $\log(M_\mathrm{dyn}/\mathrm{M}_\odot) = 8.6$, meaning that our dynamical mass is dominated by systematics. We remark that within a factor of 2, this M_dyn of 159717 is comparable to the stellar mass of the satellite 159716 (Section 5.2). Conversely, using the NIRSpec [O III]λ5007-inferred size, we obtain $\log(M_\mathrm{dyn}/\mathrm{M}_\odot) = 10.1$ dex (9.2 dex using J. P. Stott et al. 2016). For the A. der Wel et al. (2022) calibration, the 1-dex increase is due to the combination of 4.5-larger R_e, plus differences in q and n. For both NIRCam and NIRSpec, significant departures from virial equilibrium would probably overestimate M_dyn.

4.3 ISM properties

From the narrow-line parameters of the medium-resolution model (Table 2, second column), we can estimate the physical properties and chemical abundances of the ISM of the host galaxy. In principle, we can estimate the electron temperature $T_\mathrm{e}(\mathrm{O}^{++})$ of the O III-emitting gas directly from the dust-corrected [O III]λ4363/[O III]λ5007 ratio. This diagnostic is insensitive to the electron density over a wide range of values, so we assume $n_\mathrm{e} = 500$ cm^{-3}, which is typical of the O II-emitting regions of star-forming galaxies at $z \sim 5$ (Y. Isobe et al. 2023), and agrees with our (very uncertain) measurements based on the [O II]λλ3726,3729 doublet ratio. To infer T_e, we use PYNEB (V. Luridiana, C. Morisset & R. A. Shaw 2015), and we do so for each of the MCMC chains, obtaining $T_\mathrm{e}(\mathrm{O}^{++}) = 26\,000 \pm 4000$ K. From this value, we estimate the O^{++} abundance to be $12 + \log(\mathrm{O}^{++}/\mathrm{H}^+) = 7.4 \pm 0.1$ using the calibration of O. L. Dors et al. (2020). Further using the calibration of Y. I. Izotov et al. (2006), we estimate also $T(\mathrm{O}^+) = 21\,000 \pm 3000$ K (but we note that this calibration is used outside its established validity range). From n_e and $T(\mathrm{O}^+)$, using again the calibration of O. L. Dors et al. (2020), we find that the O^+ abundance is small (6.6 dex). The total metallicity is $12 + \log(\mathrm{O/H}) = 7.5 \pm 0.1$, or 10 per cent solar (M. Asplund et al. 2009).

To assess the photoionization source, we use the methods of G. Mazzolari et al. (2024, Fig. 10). We show the emission-line ratios [O III]λ4363/Hγ versus [Ne III] λ3869/[O II]λλ3726,3729, since these two ratios are robust against dust attenuation (unlike the version of the diagram that replaces [Ne III] λ3869 with [O III]λ5007). Our main target 159717 is found in the AGN-only region of the diagram, driven by the high [O III]λ4363/Hγ ratio. A number of high-redshift AGNs are also shown, including both Type 1 AGN (V. Kokorev et al. 2023; H. Übler et al. 2023, 2024; R. Maiolino et al. 2024; G. Mazzolari et al. 2024; I. Juodžbalis et al. 2025) and Type 2 AGN (G. Mazzolari et al. 2024; H. Übler et al. 2024; J. Scholtz et al. 2025c).

4.4 The absorbing clouds

As shown in Fig. 7(b), there is a clear absorption component near the rest-frame centroids of narrow and broad Hα emission lines in 159717. Such Balmer absorption is frequently seen in spectroscopically confirmed broad-line LRDs revealed by *JWST*, with a detection fraction of ∼20 per cent (J. Matthee et al. 2024; I. Juodžbalis et al. 2024a). Clearly, the case of 159717 shows that the occurrence rate of Balmer absorption can be even higher because NIRSpec medium-resolution spectroscopy is not effective in selecting such narrow absorption close to the line centroids (see Fig. 7). The absorption in LRDs is unlikely to have a stellar origin, as the absorption is usually

[1]We note that the prevalence of time variability among LRDs is debated, with NIRCam studies of large samples of LRDs showing no time variability (Z. Zhang et al. 2025).

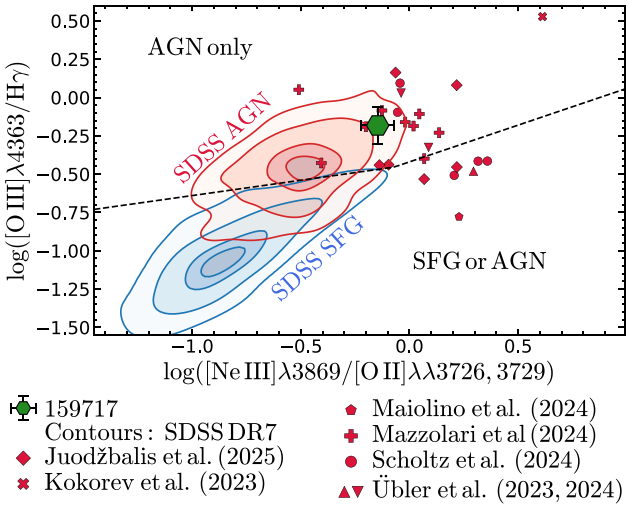

Figure 10. The photoionization diagnostic of G. Mazzolari et al. (2024) places our main target 159717 (hexagon) firmly in the 'AGN only' region, above the dashed demarcation line. For reference, we show star-forming and AGN-host galaxies from SDSS (contours), and a range of high-redshift AGN from the literature.

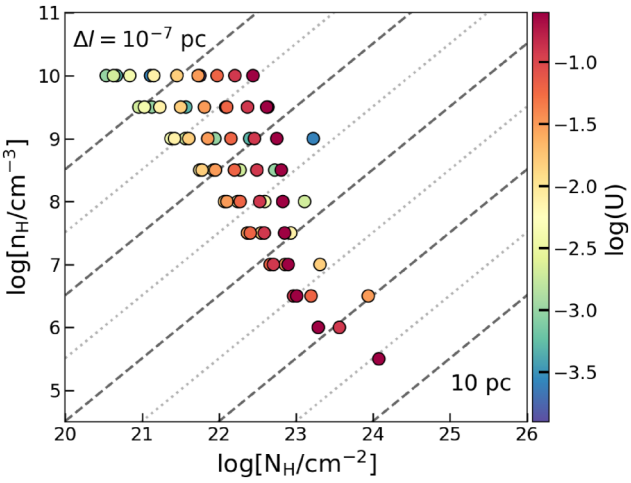

Figure 11. Plausible parameter space for the physical conditions of the warm absorber in 159717 that produces the Hα absorption. Coloured circles correspond to CLOUDY photoionization models for the absorber with a range of hydrogen density, column density, and ionization parameter. Dashed and dotted lines represent the effective thickness, N_H/n_H, of the absorber. With a single absorption line, N_H, n_H, and U show significant degeneracy. Still, there is a general indication of high densities and/or high column densities for the absorber.

deeper than the underlying continuum with a high EW, meaning the absorbing medium must (also) be absorbing the broad Balmer lines. The same situation is seen in 159717 as shown in Fig. 6.

Naively, one can model the absorption as a slab of gas obscuring our line of sight (LOS), as done in I. Juodžbalis et al. (2024a). To produce a strong Balmer absorption, the gas needs to be dense enough to collisionally excite hydrogen to the level $n = 2$, and/or thick enough to trap Lyα photons. With the optical depths, we fit for the Balmer absorption lines in Table 2, we calculate the column density of the excited hydrogen using

$$N_{H(n=2)} = \frac{m_e c}{4\pi e^2 f_0 \lambda_0}\tau, \quad (3)$$

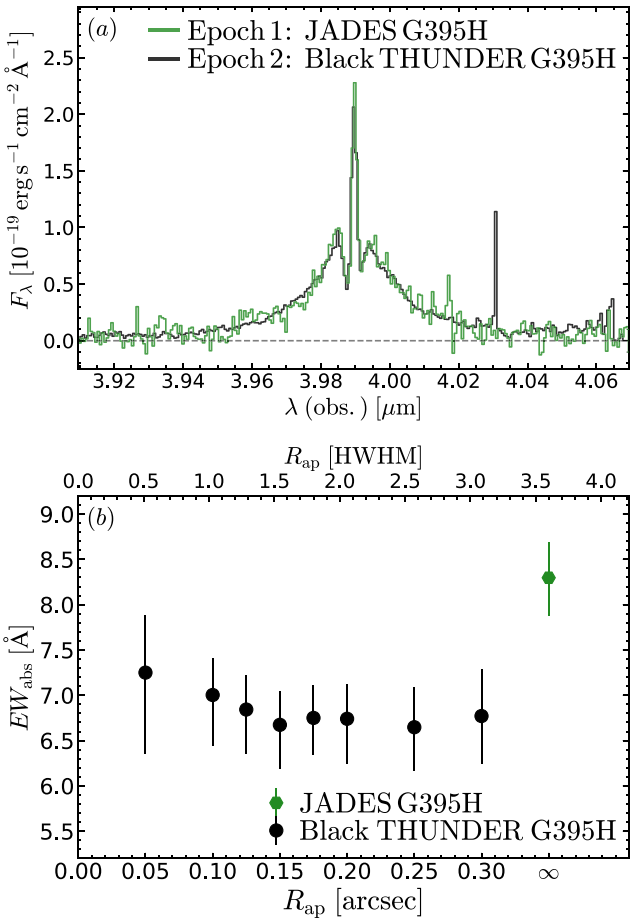

Figure 12. Panel (a)compares the Hα emission from JADES (Epoch 1, 2023 December, green) and BlackTHUNDER (Epoch 2, black; 2024 December). Panel (b) shows the EW of the Hα absorption (JADES, green hexagon; and BlackTHUNDER, black circles); the black circles show EW as a function of the aperture radius. The top axis indicates the extent of the radial aperture in units of the half-width at half maximum (HWHM) of the NIRSpec/IFS PSF. The fiducial measurements differ by 2.6σ.

where m_e is the electron mass, c is the speed of light, $e \equiv q_e/\sqrt{4\pi\epsilon_0}$ is the 'Gaussian electron charge' (q_e is the electron charge and ϵ_0 is the vacuum permittivity), f_0 is the oscillator strength, λ_0 is the central wavelength, and τ is the integrated optical depth with a dimension of velocity. From the value of $N_{H\,(n=2)}$, we can use CLOUDY models to infer the density and column density of hydrogen, n_H and N_H. Unfortunately, due to the lack of constraints on the ionization fraction, the conversion between $n = 2$ and the total hydrogen column density is very uncertain, resulting in poorly constrained N_H (Fig. 11).

Intriguingly, the EW of the Hα absorption is different between the JADES and BlackTHUNDER *G395H* observations. In Fig. 12(a), we compare directly the two emission lines. Note that there may be small flux-calibration systematics affecting the normalization. In Fig. 12(b), we compare the EW measured from JADES (hexagon) to the EWs measured from BlackTHUNDER. To check for systematics, for BlackTHUNDER we extended the measurements of Section 3.3 to a set of apertures of increasing radius. It is clear that the value from BlackTHUNDER is systematically lower, with 2.6σ significance (P-value < 0.005). This result is unchanged if we repeat the BlackTHUNDER measurements but modelling only Hα, without including broad Hβ, hence the systematic difference is not due, e.g.

to tying the absorber kinematics and covering factor between the two Balmer lines. Moreover, we can rule out that the observed difference is due to errors in the flux calibration, because EW measurements are completely insensitive to flux calibration. In principle, aperture losses could play a role, since our EW measurements combine flux emitted on different spatial scales; however, the BlackTHUNDER data also rules out this possibility, because the EW stays constant (within the uncertainties) as we change the aperture radius.

Under the hypothesis that the absorber is in front of both the broad lines and the continuum, the EW of a non-saturated absorber would not change with the underlying continuum. This would suggest that it may be the absorber itself that is varying on a rest-frame time-scale of two months. The picture is complicated by the fact that in the JADES observations, the absorber is nearing saturation (τ_0(H α) $\sim$3; Table 2). New observations are needed to both confirm the time variability, and to establish if it originates in the absorber itself or rather in the underlying continuum and BLR.

5 NEARBY SOURCES

5.1 Aperture spectra

The aperture spectra of three associated sources are shown in Fig. 13. 159716 and 159717B are undoubtedly detected and associated with 159717 (panels a–f). To the south-west, we find evidence for a spatially detached emission-line source, detected only in [O III]λ5007, which we call 159717C (panels i and j). Below we report the emission-line properties of these three sources, using a simplified version of the model from Section 3.3, where we removed both the broad-line Hβ and Hα, and the gas absorber.

159717B (Figs 13a–d) is spatially unresolved (Section 3.1) and has Gaussian line profiles with $\sigma_n = 41 \pm 1$ km s^{-1}, narrower than for 159717. The continuum in this location is dominated by the bright spiral arm of 159715, which prevents us from robustly detecting 159717B's own continuum. Using the Balmer lines, and under the same assumptions as for 159717 (Section 3.3), we infer $A_V = 0.1 \pm 0.3$ mag, consistent with no dust. We estimate the star formation rate (SFR) using the Hα-to-SFR scaling of A. E. Shapley et al. (2023). After applying an aperture correction of 1.5, we obtain $\log(\mathrm{SFR}[\mathrm{M}_\odot\ \mathrm{yr}^{-1}]) = -0.5 \pm 0.1$. Lacking an accurate continuum deblending, we do not attempt to measure a stellar mass for this target, but we note that if it lay on the star-forming sequence it would have a stellar mass $\log(M_\star/\mathrm{M}_\odot) = 7.6$–$8.1$, where the lowest value is from J. W. Cole et al. (2025, their $z = 4.5$–5 redshift bin), while the largest value is from the bias-corrected theoretical work of W. McClymont et al. (2025b) and the corresponding empirical measurements of C. Simmonds et al. (2025). Of course, this estimate is very uncertain, not just due to the large scatter about the main sequence (0.3 dex; J. W. Cole et al. 2025), but primarily due to the possibility that the galaxy may not lie on the main sequence (e.g. due to environment-driven quenching in close environments; S. Alberts et al. 2024; F. D'Eugenio et al. 2025f), and to the possibility that the emission lines are not powered by star formation photoionization. In fact, we cannot rule out that 159717B may be externally photoionized (see also Section 5.4).

159716 (Figs 13e–h) is much more extended. This source is clearly detected in the continuum, both in NIRSpec and NIRCam, hence it is clearly a satellite galaxy with stellar content (Section 5.2). Its emission lines are also Gaussian, but have velocity dispersion $\sigma_n = 67 \pm 2$ km s^{-1}, broader than both 159717B and 159717.

The last source, 159717C, is a tentative detection (Figs 13i–l). As for 159717B, there is substantial contamination from 159715 in the foreground, hence the continuum level is unreliable. This system has a diffuse morphology. While the SNR is low, three arguments support the detection of this system. In addition to [O III]λ5007 in the aperture spectrum (8σ detection), we also detect this source in the emission-line maps (Section 5.3). Moreover, there is a marginal detection of Hα at the same redshift as [O III]λ5007 (4σ significance). Finally, we have some indications that weak [O III]λ5007 emission may be present in the NIRCam $F200W-F277W$ image (Section 5.3), at a location that matches very well the NIRSpec findings. This source has an intrinsic velocity dispersion $\sigma_n = 70 \pm 10$ km s^{-1}, which is large for such a faint source. We also find a [O III]λ5007/H $\beta > 10$.

Unfortunately, none of these sources has useful constraints on the dynamical mass. For 159717B and 159717C, we lack an accurate measurement of their size and morphology. Using the same formula

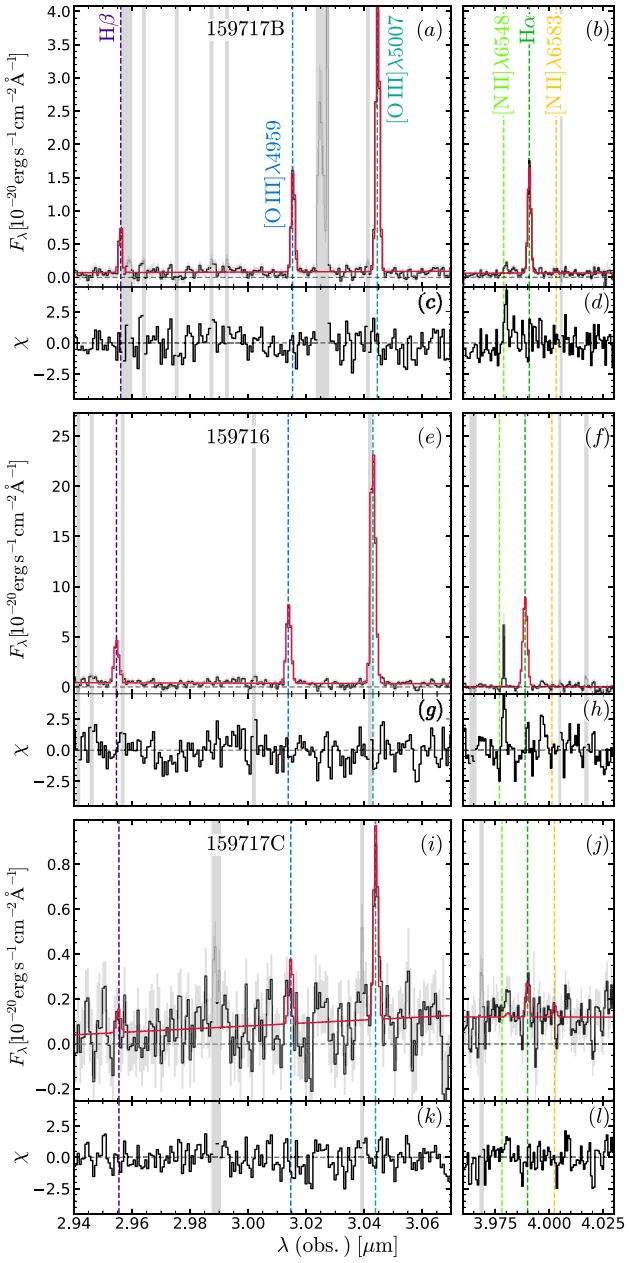

Figure 13. BlackTHUNDER *G395H* aperture spectra for the three nearby sources, showing H β and [O III]$\lambda\lambda$4959,5007 (left) and Hα (right). The three sources show a range of line widths and ionization properties.

as in Section 4.2, and adopting conservatively $R_e < 0.1$ pc, $q = 1$ and $n = 1$, we obtain $\log(M_{dyn}/M_\odot) < 9.1$ and < 9.6 for 159717B and 159717C, respectively. For 159716, the use of the virial theorem seems inappropriate, since this galaxy may be out of stationary equilibrium, as discussed in Section 5.3.

5.2 Stellar mass measurement for 159716

We measure the stellar mass of only one galaxy, 159716. Our method of choice is the Bayesian inference framework PROSPECTOR (B. D. Johnson et al. 2021). The SED model is derived from S. Tacchella et al. (2022), while the comparison with observations follows the setup of F. D'Eugenio et al. (2025e), with improvements described in W. M. Baker et al. (2025)-and S. Carniani et al. (2025). Here, we summarize the most important aspects. We use stellar-population template spectra derived from the MIST isochrones (J. Choi et al. 2016) and C3K model atmospheres (C. Conroy et al. 2019), synthesized using FSPS (C. Conroy, J. E. Gunn & M. White 2009; C. Conroy & J. E. Gunn 2010). The nebular continuum uses precomputed CLOUDY models (N. Byler et al. 2017). The dust attenuation law follows S. Noll et al. (2009) and the implementation of M. Kriek & C. Conroy (2013). A dual dust screen captures attenuation due to diffuse dust, and the additional birth-cloud attenuation toward star-forming regions (S. Charlot & S. M. Fall 2000), following the parametrization of S. Tacchella et al. (2022). We adopt a non-parametric star formation history (SFH) with 9 time bins between $z = 20$ and the epoch of observation $t = 0$. The first four bins are manually set to $t = 5$, 10, 30, and 100 Myr, while the remaining five bins are logarithmically spaced between 100 Myr and $z = 20$. We use a 'rising' probability prior (C. Turner et al. 2025), where the SFH follows the increasing mass accretion rate on dark-matter haloes (S. Tacchella et al. 2018). We also use a second-order Chebyshev polynomial to rescale the best-fitting model to the level and shape of the observed spectrum; this means that our extensive quantities ($M_\star$, SFR) are driven by the photometry, while the high-frequency spectral information (e.g. emission-line ratios) is preserved. Overall, this model has 22 free parameters, and we calculate the posterior probability distribution using the MCMC method. The data are shown in Fig. 14(a), with the BlackTHUNDER aperture spectrum in grey. There is a systematic flux mismatch between the NIRCam photometry and NIRSpec spectrum, probably due to the photometry suffering from contamination, while the spectroscopy suffers from aperture losses. The spectrum of this satellite galaxy displays a clear Balmer break. Unlike for LRDs, the shape of the continuum is blue both bluewards and redwards of the break, as expected from a Balmer break due to an older stellar population. This break therefore suggests that there was likely a decline in the SFR in the last few tens million years. The Balmer break is also supported by NIRCam, since the flux in $F335M$ and $F356W$ (which does not have strong line contamination) is considerably higher than the SED extrapolation from the UV. The PROSPECTOR SFH shows a drop, which drives the observed Balmer break. We show only a subset of the model parameters (Fig. 14d), highlighting the most relevant physical properties. In particular, we infer $\log(M_\star/M_\odot) = 8.74^{+0.10}_{-0.04}$.

5.3 Spatially resolved gas kinematics

To fit the spatially extended emission, we use QUBESPEC (J. Scholtz et al. 2025b). The narrow lines are modelled as single-component Gaussians, and broad Gaussians are added to model the BLR Hα. [O III]$\lambda\lambda$4959,5007 can also use a broader component, but a single component is favoured everywhere, which is in agreement with the

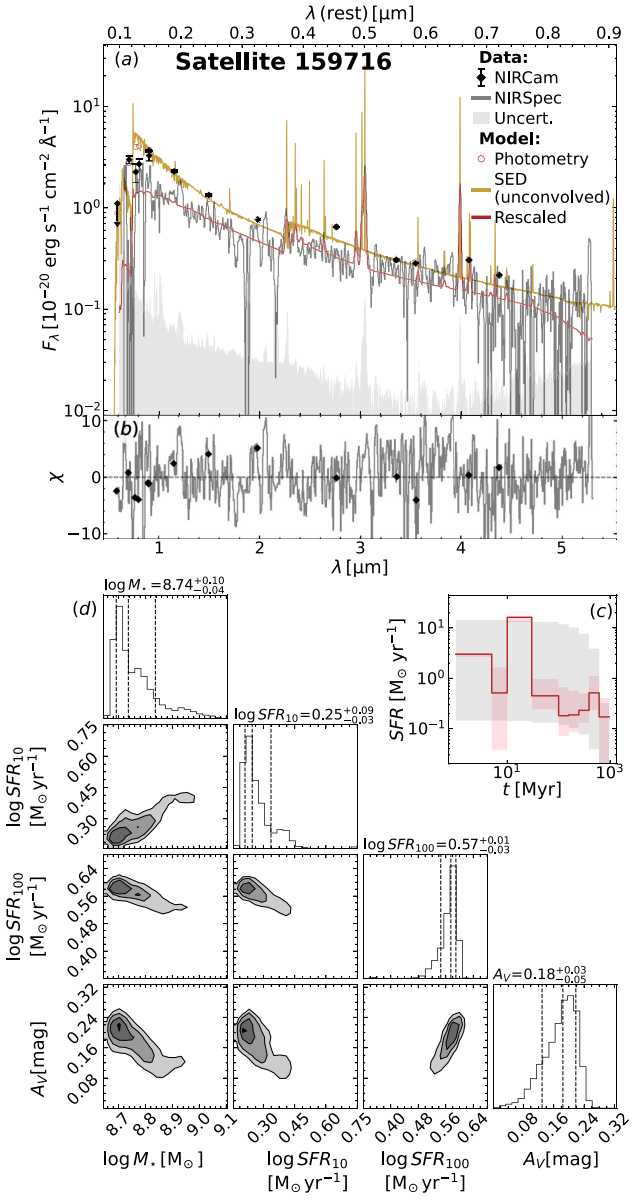

Figure 14. Summary of the PROSPECTOR inference of the physical properties of 159716. The data and best-fitting model are shown in panel (a); a weak Balmer break is evidence in both the NIRSpec data (grey line) and in the fiducial model (the sand and red lines are the model, and the model rescaled to match the shape and normalization of the spectrum). The residuals are shown in panel (b). Panel (c) shows the SFH, with the prior in grey. The corner diagram (panel d) displays a subset of the model parameters.

expectations, since we barely detect a second, broader [O III]$\lambda\lambda$4959,5007 component even in the aperture-integrated spectrum, which has much higher SNR than individual spaxels (Section 3.5). For the same reason, no model of the BLR Hβ is used.

The SNR map of [O III]λ5007 is overlaid as white contours on the NIRCam RGB image in Fig. 15(a), highlighting values of 15, 30, and 60. The colour bar measures the emission-line map derived from NIRCam $F277W-F200W$ (Section 3.1), also overlaid in transparency. The two independent emission-line maps match reasonably well. NIRSpec detects an extended ionized-gas bridge connecting all three of 159716, 159717, and 159717B, with a noticeable gap

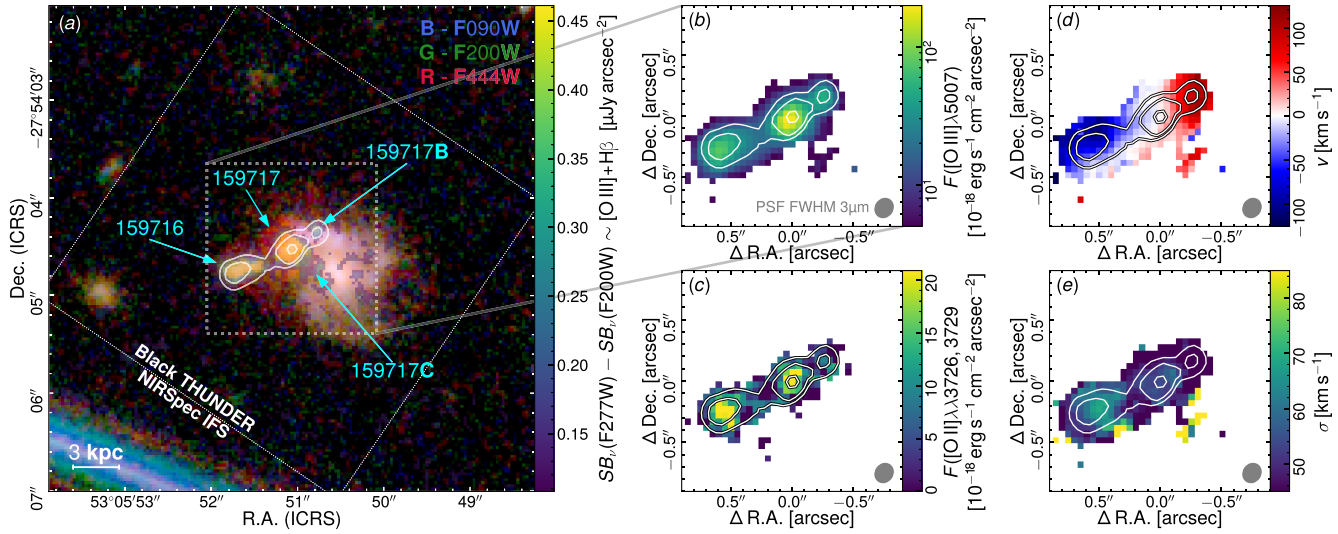

Figure 15. Same as Fig. 2, but also highlighting [O III]λλ4959,5007 emission (white contours), estimated using the photometric excess between NIRCam *F277W* and *F200W*. The map identifies another possible satellite to the north-west of 159717, 159717B, which is also confirmed by BlackTHUNDER in [O III]λλ4959,5007 and Hα. The bright source at the centre of JADES-GS-159715 is the galaxy's bulge, which is prominent in this map due to its relatively red *F200W*−*F277W* colour.

separating 159717C (Fig. 15b). The [O II]λλ3726,3729 emission-line map from the prism observations (Fig. 15c) shows significant detections both in 159717 and in 159716, indicating the presence of some lower ionization gas too, except for 159717C.

The velocity map (Fig. 15d) displays a smooth gradient across the entire gas distribution, with an end-to-end amplitude of 200 km s^{-1}, while the velocity dispersion map is relatively low at around 50 km s^{-1} (Fig. 15e). There is a 70-km s^{-1} σ peak about one spaxel east of the centre of 159716, and a second, weaker peak between 159717 and 159717B. The fact that σ is overall narrow, with the highest values found between the surface-brightness maxima suggests a merger scenario, where gas is being removed from the galaxies and has formed an extended, common reservoir. Alternatively, the superposition along the LOS of multiple systemic kinematic components could also broaden the velocity dispersion. However, in this case-, the observed broadening (50–70 km s^{-1}) requires such a small difference in systemic velocity, as to make interaction a more plausible scenario. Significant disturbance of stationary equilibrium can be inferred from the kinematics of 159716; for this galaxy, the photometric major axis is aligned with the kinematic axis, implying prolate rotation which is dynamically unstable for such an elongated object (A. M. Fridman & V. L. Poliachenko 1984; D. Merritt & L. Hernquist 1991). The disturbed nature of 159716 suggests an advanced interaction stage. This hypothesis resonates with the presence of the fainter 159717B on the far side with respect to 159717, possibly due to tidally stripped material during the first passage. In this case, 159717 would be interpreted naturally as the most massive of the three systems. Overall, these observations imply that 159717, far from being isolated, is located at the centre of a relatively dense region, where gas is collapsing, leading to both star formation and SMBH accretion.

159717C instead represents a separate case; it has velocity dispersion $\sigma \sim 100$ km s^{-1}, which is small, but noticeably higher than the rest of the system – a fact that is even more striking when we recall that this is the faintest of the three sources. This larger dispersion is confirmed by the aperture spectra, although the measurement uncertainties are large, due to the low SNR. This source could represent a tidally disrupted system or a tidal tail. Its location, orthogonal to the axis connecting 159717B to 159716, disfavours an origin from either of 159717, 159717B or 159716, but we cannot fully rule out 159717C being a smaller system involved in the merger. Still, the relatively large dispersion, together with the non-detection in both Hβ and Hα (the latter line has SNR = 4), could point to 159717C being a ionized gas outflow, or, alternatively, a gas cloud photoionized by the AGN. It is located at right angles to both the elongated gas distribution and to the spatially resolved component of 159717 (Section 3.1; Table 1), which also favours the interpretation of an outflow or photoionized cloud. If we accept the hypothesis that 159717 is the dominant galaxy in the system, and given the clear presence of an SMBH, it is natural to attribute the origins of this outflow to 159717 itself.

5.4 Gas ionization sources

We do not detect [N II] λ6583 or other low-ionization lines useful for the BPT (J. A. Baldwin et al. 1981) and VO diagrams (S. Veilleux & D. E. Osterbrock 1987), but thanks to the depth of these observations, we can provide stringent limits on the [N II] λ6583/Hα. In Fig. 16(a), we highlight the four components of the system around 159717 as large diamonds, which are colour coded to match the segmentation map in panel (b). The largest three systems, 159717, 159716, and 159717C display [O III]λ5007/Hβ ratios (or lower limits) consistent with star-forming galaxies (A. J. Cameron et al. 2023) and type-1 AGN (I. Juodžbalis et al. 2025) at the same epoch. These three sources have very similar locations on the BPT diagram, despite 159717 being seemingly dominated by AGN emission. Nevertheless, their location cannot discriminate between AGN-driven and star-formation-driven photoionization (D. D. Kocevski et al. 2023; H. Übler et al. 2023), since the demarcation lines derived for local star-forming and AGN-host galaxies (dotted and dashed lines in Fig. 16a) do not apply at $z \gtrsim 5$. In Fig. 16(a), we also show individual spaxels, with the same colour coding. When detected, [O III]λ5007/Hβ displays a relatively broad range of values, from 3 to 12, including high-SNR detections. This variation suggests that the ionization conditions vary across the system. This is confirmed by the [O III]λ5007/[O II]λλ3726,3729 map (Fig. 16c), derived from

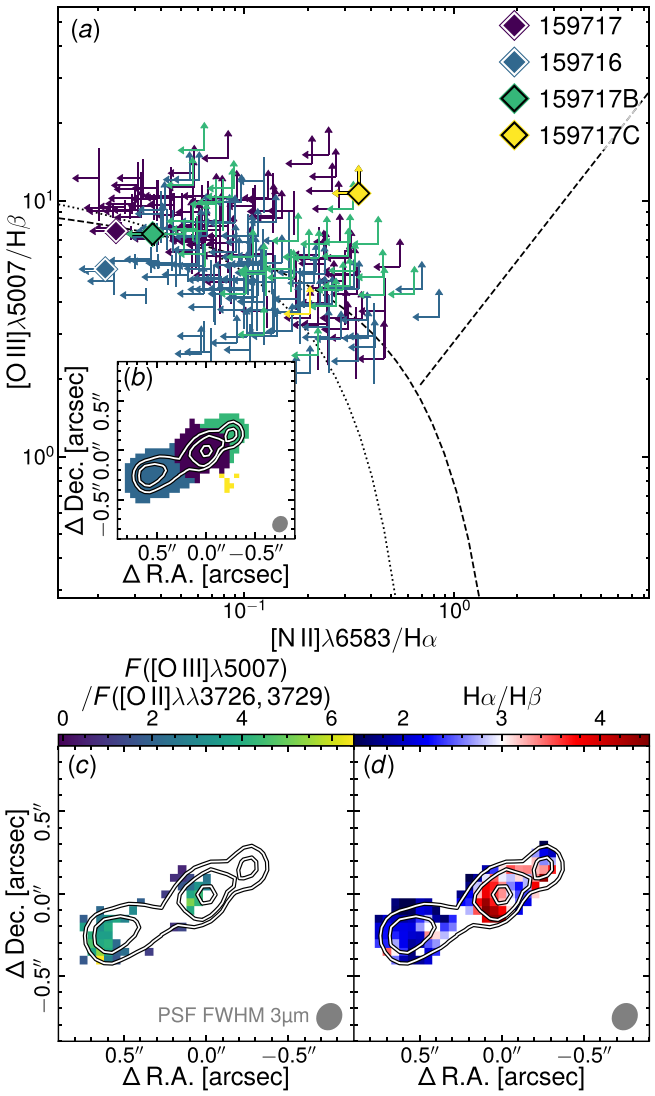

Figure 16. Panel (a): BPT diagram, colour coded as indicated in the segmentation map of panel (b) (the dashed and dotted demarcation lines separate star-forming, AGN, and low-ionization emission at $z \sim 0$, and are taken from L. J. Kewley et al. 2001, 2006; G. Kauffmann et al. 2003; and K. Schawinski et al. 2007). The BPT diagram indicates that three out of four systems are located in a similar region of the BPT (large diamonds), while 159717C (large yellow diamonds) has noticeably larger [O III]λ5007/H β. The individual spaxels (colour coded as in panel b) show a broad range of [O III]λ5007/H β, while [N II] λ6583is not detected. Panel (c): the ionization diagnostic [O III]λ5007/[O II]λλ3726,3729; we do not apply a dust attenuation correction, hence the intrinsic ratio should be lower in 159717 than in 159716, given that the observed ratios are comparable, but 159717 is more dusty than 159716. Panel (d): the Balmer decrement from the narrow lines is largest in 159717, indicating that it has the strongest dust attenuation among the four systems.

fitting the BlackTHUNDER prism data. The Balmer decrement map is shown in Fig. 16(d); in 159717, the decrement is larger than the Case-B value of 2.86, while 159716 shows no appreciable deviation, indicating little dust content. Overall, these findings are consistent with the spatially integrated view of star-forming galaxies and LRDs at $z \sim 5$ (A. E. Shapley et al. 2023; L. Sandles et al. 2024; I. Juodžbalis et al. 2025; A. J. Taylor et al. 2025; W. McClymont et al. 2025a).

Probably the most interesting source is 159717C. While the lower limit on [O III]λ5007/H β is not constraining, in Fig. 16(a), we show instead the ratio $2.86 \cdot$ [O III]λ5007/H α, where we treat the 4σ measurement of Hα as a detection, and we derive Hβ from Case-B recombination and no dust. This lower limit is larger than the integrated value for the other three galaxies, suggesting a different source of photoionization. The harder ionizing spectrum implied by the large inferred [O III]λ5007/Hβ supports the hypothesis that 159717C is not a star-forming clump or tidal tail, but either an outflow or a AGN-illuminated cloud (Section 5.3).

6 DISCUSSION

6.1 Overmassive black hole

The stellar mass of the host galaxy of 159717 is difficult to determine, due to a combination of intrinsic and accidental difficulties (Sections 3.9 and 4.2). Nevertheless, maximal stellar models for this kind of source consistently exceed the physical limit imposed by dynamical mass (B. Wang et al. 2025; J24; Y. Ma et al. 2025b; X. Ji et al. 2025; F. D'Eugenio et al. 2025a; H. B. Akins et al. 2025a). For this reason, projection effects alone cannot explain why $M_\star > M_{\rm dyn}$ is very common among broad-line AGN with 'v'-shaped SEDs. Unless one assumes a preferential viewing angle to the host galaxy, the maximal mass scenario seems ruled out. In addition, the finding of time variability in the rest-frame optical continuum in A2744-QSO1 (X. Ji et al. 2025) disfavours a stellar-dominated continuum in 159717 too, since the two objects share at least four similarities: the 'v'-shaped SED, a relatively high $M_\bullet/M_{\rm dyn}$ ratio (discussed below), a broad Hα line that is best fit by a double Gaussian, and a strong Hα absorber in the rest frame (F. D'Eugenio et al. 2025a). In Fig. 17(a), we show 159717 on the $M_\bullet$–$M_\star$ plane, together with sources from the literature. Since we cannot measure a reliable $M_\star$, we use $M_{\rm dyn}$ as an upper limit; the conclusion of an overmassive black hole (relative to local scaling relations) seems thus warranted, in agreement with previous findings in the redshift range $z = 5$–7 (Y. Harikane et al. 2023; R. Maiolino et al. 2024). While recent works have challenged the inference of overmassive black holes (J. Li, Y. Shen & M.-Y. Zhuang 2025; Y. Sun et al. 2025), both these works focus on lower redshifts $z \sim 3$ and more massive galaxies.

It is important to note that, in addition to the uncertainties on their $M_\star$, LRDs also have uncertain $M_\bullet$. While virial SMBH mass estimates from single-epoch spectra are widely used, they are subject to systematic uncertainties from assumptions about the geometry, kinematics, and ionization of the BLR. Calibrations can vary by up to 0.5 dex depending on the line used (e.g. H α versus C IVλλ1548,1551; C. Bertemes et al. 2025) and the adopted virial factor or line width (e.g. E. Dalla Bontà et al. 2025). These systematics must be kept in mind, especially when comparing across redshifts, and particularly for a seemingly new class of AGN, such as LRDs. While a few direct $M_\bullet$ measurements do exist beyond the local Universe (R. Abuter et al. 2024), these do not extend to LRDs.

More recently, V. Rusakov et al. (2025) proposed that broad-line profiles that cannot be modelled by a single Gaussian are best modelled with an exponential profile, which represents the effect of electron scattering by ionized gas. With their approach, the intrinsic FWHM is much narrower than what inferred from a single-Gaussian fit, leading to much smaller SMBH masses. However, since we use two Gaussians, and given the inferred flux ratio between the two components, the decrease in FWHM between the fiducial fit (Table 2) and the exponential fit (Appendix E) is only a factor of two, leading to four times smaller SMBH mass of $\log(M_\bullet/{\rm M}_\odot) = 7.0^{+0.2}_{-0.3}$. Even

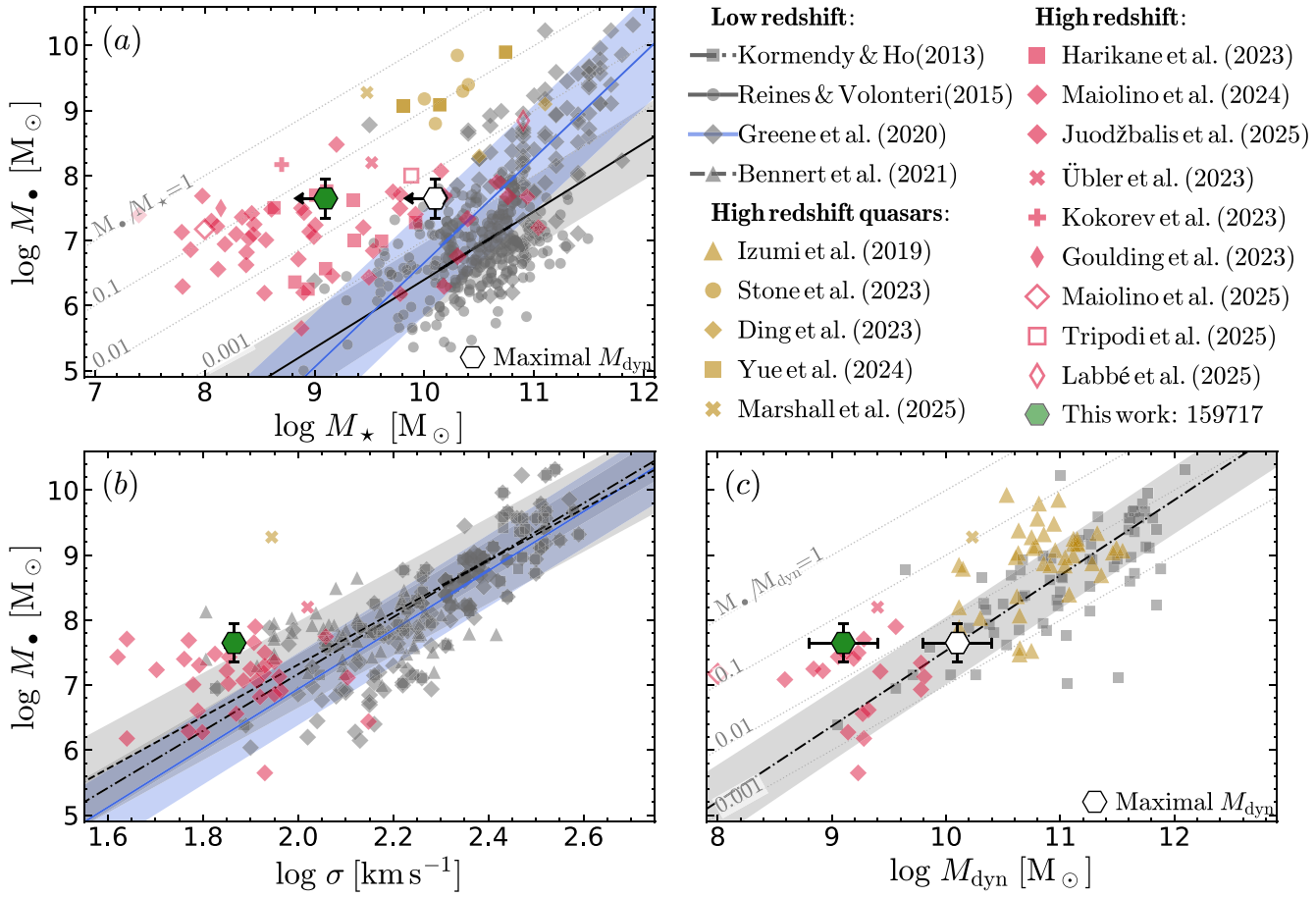

Figure 17. When compared to local scaling relations between $M_\bullet$ and $M_\star$ (panel a), the SMBH in 159717 (green hexagon) is overmassive, similar to the low-luminosity, high-redshift AGN samples from earlier works (e.g. Y. Harikane et al. 2023; R. Maiolino et al. 2024). Even our most conservative estimate (white hexagon, Section 4.2) lies above the local relation from A. E. Reines & M. Volonteri (2015, but is consistent with J. E. Greene et al. 2020). Similarly to R. Maiolino et al. (2025a) and X. Ji et al. (2025), we do not have an actual $M_\star$ measurement, but we use our largest estimates of M_{dyn} as upper limits on $M_\star$. In contrast to relations with $M_\star$, and in agreement with R. Maiolino et al. (2024), 159717 seems to follow the $M_\bullet$–σ relation (panel b), while agreement with the $M_\bullet$–M_{dyn} relation depends on the adopted M_{dyn} value (panel c). The low-redshift data and fitted relations are from J. Kormendy & L. C. Ho (2013), A. E. Reines & M. Volonteri (2015), J. E. Greene et al. (2020), and V. N. Bennert et al. (2021); for the relations, we show the 16th–84th prediction interval as a shaded region. High-luminosity AGNs (quasars, golden) are from T. Izumi et al. (2021), X. Ding et al. (2023), M. A. Stone et al. (2023), M. Yue et al. (2024a), and M. A. Marshall et al. (2025). High-redshift, low-luminosity AGNs (red) are from Y. Harikane et al. (2023), R. Maiolino et al. (2024, 2025a), I. Juodžbalis et al. (2025), H. Übler et al. (2023), V. Kokorev et al. (2023), A. D. Goulding et al. (2023), and I. Labbe et al. (2024). This figure is available as a github repository.

with this reduced $M_\bullet$ value, 159717 remains above the local $M_\bullet$–$M_\star$ relation of A. E. Reines & M. Volonteri (2015), indicating that it is overmassive under the scenario of V. Rusakov et al. (2025). This demonstrates that overmassive black holes can exist even against the most conservative modelling assumptions.

Our results are consistent with the redshift evolution between a regime of large $M_\bullet$–$M_\star$ scatter at early epochs and the settling of the local scaling relation around $z \sim 3$, as proposed by I. Juodžbalis et al. (2025). In contrast to stellar mass, our target is fully consistent with the $M_\bullet$–M_{dyn} relation (Fig. 17b), in agreement with the sample of R. Maiolino et al. (2024).

It is interesting to note that both the stellar mass and the upper limit on the dynamical mass of 159716 are of the same order as the dynamical mass of 159717. If true, this would imply that we are witnessing a major merger, which intuitively seems at odds with the disrupted nature of 159716. Admittedly, this different behaviour could also be explained by an encounter between galaxies of similar mass but significantly different size, such that the more diffuse nature of 159716 relative to 159717 could have made the former more susceptible to external perturbations, unlike 159717.

6.2 Gas metallicity

For the metallicity, we find a gas-phase value of $Z = 0.1\ Z_\odot$, but these measurements are subject to large uncertainties, due to insufficient information to explore the possibility of a multizone ISM. The key unknown is the possible presence of a high-density zone ($n_e \gtrsim 10^5$ cm^{-3}) in the narrow-line region (e.g. L. Binette et al. 2024). If present, this zone would significantly affect the [O III]λ4363/[O III]λ5007 ratio, yielding a higher $T_e(O^{++})$, a higher emissivity, and, therefore, lower metallicity. The auroral-to-strong OIII ratio may be enhanced in the densest zone of the narrow-line region due to collisional suppression of [O III]λ5007. This would explain both the high n_e inferred from high-ionization species in local narrow-line AGN ($n_e \sim 10^4$ cm^{-3}; L. Binette et al. 2024) and the anticorrelation between the ratio [O III]λ5007 to narrow Hβ and [O III]λ4363/[O III]λ5007 in type 1 AGN (where, according to the unified model of AGNs, we should be seeing the deepest zone of the narrow-line region). As a reference, from the observed [O III]λ5007/Hβ and assuming $T_e = 15\,000$ K and $n_e = 10^5$ cm^{-3}, PYNEB gives $12 + \log(O^{++}/H) = 7.9$ dex, an O^{++} abundance that is three times

higher than the fiducial value reported in Table 2. Nevertheless, the scatter about the metallicity relations at these redshifts is large, hence our value is still plausible for a galaxy with the dynamical mass of 159717. We do not attempt a multiline approach due to the relatively low number of emission lines, with key density diagnostics undetected (C III]λλ1907,1909, [S II] λλ6716,6731), or not adequately resolved ([O II]λλ3726,3729).

We find substantial dust attenuation through the narrow-line ratios, in agreement with previous works (F. D'Eugenio et al. 2025a). This result is somewhat in tension with two findings. On one hand, our dust attenuation is larger than for typical star-forming galaxies at $z = 5$ (A. E. Shapley et al. 2023; L. Sandles et al. 2024). This could be alleviated by attributing some of the narrow-line emission to AGN photoionization. In addition, LRDs seem to require low dust attenuation, based on constraints from MIR and far-infrared observations (C. M. Casey et al. 2024, 2025; D. J. Setton et al. 2025b; H. B. Akins et al. 2025c).

6.3 The broader picture

The fact that 159717 is found at the centre of an extended distribution of ionized gas seems significant. Indeed, many LRDs seem accompanied by fainter blue dots (C.-H. Chen et al. 2025; P. Rinaldi et al. 2025), suggesting a physical association. The presence of dense gas clouds in 159717 could be due to gas being accreted towards the central regions, aided by gravitational torques during the ongoing merger with 159716. LRDs are certainly capable of driving outflows, which are generally observed through nuclear hydrogen absorption (J. Matthee et al. 2024; J24; V. Rusakov et al. 2025), or through broad, centrally concentrated [O III]λ5007 emission (J24). In 159717, for the first time, we see tentative evidence of a spatially detached ionized gas outflow (Section 5). If confirmed, this detection could indicate past feedback. The gap between this cloud and 159717 may indicate that feedback was interrupted, perhaps in relation to the recent merger with 159716. For instance, if the rate of gas accretion towards the central regions was too high, it could have overwhelmed the outflows driving an accumulation of gas.

This scenario would be in agreement with recent works, which have highlighted the complex morphology of many LRDs (P. Rinaldi et al. 2025; A. Torralba et al. 2025a). Although there are notable examples of LRDs without prominent companions (e.g. L. J. Furtak et al. 2023, 2024; M. Carranza-Escudero et al. 2025; R. P. Naidu et al. 2025), several others are known to have neighbours (T. S. Tanaka et al. 2024; R. M. Mérida et al. 2025).

6.4 Gas absorber

The observed Hα absorption is undoubtedly originating in a gas cloud between the BLR and the observer. A stellar origin is excluded because when measuring the EW of Hα with respect to the continuum (by subtracting the unabsorbed model BLR from the data), we find EW(H α) = 100 Å, much higher than in any stellar-atmosphere model. Similarly, if the absorber was not positioned in front of the BLR, the absorption depth would reach unphysical negative values. However, even with high-quality, high-resolution data, it is impossible to provide a tight constraint on the total column density, due to the uncertain conversion between the $n = 2$ hydrogen population and the other levels, and between the bound and ionized hydrogen populations. This uncertainty is reflected in the broad range of column and volume densities that can reproduce our observations (Fig. 11). Tighter constraints are available when Hβ absorption is also strongly detected (I. Juodžbalis et al. 2024a), but this would require deeper spectra – particularly for sources with large Balmer decrement, such as LRDs (L. J. Furtak et al. 2024; M. Brooks et al. 2025; G. P. Nikopoulos et al. 2025; F. D'Eugenio et al. 2025b; A. Torralba et al. 2025b). In the future, deep *JWST* programs using high-resolution *G*235*H* and *G*395*H* gratings may be able to better characterize Balmer absorption in AGNs at redshifts $z = 2.5$–7. The range $z = 2.5$–3.9 would additionally cover He Iλ1.08μm, useful to characterize the ionization state of the absorbing gas and thereby the distance of the absorber to the black hole accretion disc (I. Juodžbalis et al. 2024a). From current data, we can constrain the total column density of hydrogen to be $\log(N_H/cm^{-2}) = 20.5$–24, with the upper range reaching the Compton-thick threshold; such high values have been proposed to explain the low X-ray to bolometric luminosity ratio of low-luminosity AGNs at $z \sim 5$ (M. Yue et al. 2024b; R. Maiolino et al. 2025b; J24), and would be consistent with the non-detection of 159717 in X-rays, despite lying in one of the deepest zones of the 7-Ms *Chandra* mosaic of GOODS-S (B. Luo et al. 2017).

Just like for A2744-QSO1 (L. J. Furtak et al. 2023, 2024), also in 159717, we can rule out completely a stellar origin of the absorber, based on the same two arguments as used in F. D'Eugenio et al. (2025a). First, the absorber EW is too large to absorb only the continuum. As noted also by J24, the depth of the absorption is so large that if we were to remove the BLR line, we would be left with negative flux. Additionally, thanks to the superior resolution of *G*395*H*, we can infer that the absorber turbulence is $v_{turb} \equiv \sqrt{2} \cdot \sigma_{abs} \approx 140$–$150$ km s^{-1}. This value is similar to what has been found independently in A2744-QSO1 by X. Ji et al. (2025) and F. D'Eugenio et al. (2025a, using, respectively, the shape of the Balmer break and the shape of Hα absorption). Such a large turbulence parameter is an order of magnitude higher than what is found in the stellar atmospheres of luminous stars (K. C. Smith & I. D. Howarth 1998), hence constituting a second, independent argument ruling out stellar absorption. To these two compelling arguments, we can add EW variability (Section 4.4). While admittedly tentative, time variability is completely inconsistent with stellar absorption, while being in perfect agreement with a scenario where the absorbing clouds are located relatively near to the SMBH.

For a typical gas temperature of $T \sim 10^4$ K, the speed of sound is of order of 10–15 km s^{-1}, implying a Mach number around 10 for the absorbing gas. Although it remains unclear how such high turbulence is sustained, the consistency with previous LRD studies reporting $v_{turb} \sim 100$ km s^{-1} supports the measurement (X. Ji et al. 2025; R. P. Naidu et al. 2025; F. D'Eugenio et al. 2025a). Similar turbulent velocities are also required to explain Fe II emission regularly seen in the UV spectra of local AGN and QSOs, yet the physical origin of this turbulence remains unresolved (J. A. Baldwin et al. 2004).

As an alternative to absorption, scenarios such as Balmer-line resonant scattering have been considered (R. P. Naidu et al. 2025). In this case, the intrinsic Balmer lines would be much narrower than the observed profiles, with the broadening primarily due to scattering. A key advantage of this scenario is that it explains why the absorber appears near rest-frame wavelengths. However, this mechanism would likely produce different line profiles for Hα and H β. While our data cannot rule out such differences, deep observations of bright targets (e.g. J24; Y. Ma et al. 2025a) will be able to test this possibility.

6.5 Towards atmospheric models?

An intriguing finding is that the optical depth of Hβ and Hα are inconsistent with the absorption cross sections of these two lines, which are set by the oscillator strengths. In our model, this ratio

should be exactly equal to the value dictated by atomic physics, which is 0.139. While of course this mismatch could be only apparent, due to the low SNR of our observations, this has now been confirmed in other objects too (e.g. F. D'Eugenio et al. 2025a, b). At face value, the only possible explanation then is that a simple passive absorber modelled as a gas slab may be inadequate, much like in the atmosphere of A-type stars the absorption strength of Hβ and higher order Balmer lines is larger than for Hα – contrary to the expectations from the relative cross sections of these lines. This explanation could imply that Hα and Hβ arise from different depths in the absorbing gas, mimicking what happens in stellar atmospheres. For reference, the density where Hα arises in A-type stars is 10^{12} cm^{-3}, larger but not too different from the findings of R. P. Naidu et al. (2025).

6.6 Absorber kinematics

Gas absorbers along the LOS of AGNs are interpreted as inflows/outflows (J. Matthee et al. 2024; J24; B. Wang et al. 2025). In our case, the absorbing cloud is consistent with no velocity component along the LOS (relative to the systemic velocity determined from the narrow lines). In principle, this low projected velocity could be due to orbital motion of a cloud bound to the SMBH. In the local Universe, this configuration would require both a high-inclination orbit, LOS alignment and the right orbital phase, as found in local AGNs (NGC 1365; R. Maiolino et al. 2010). However, the combination of all these occurrences is unlikely, making NGC 1365 one of very few cases where the inclination is suitable for observing transiting clouds. The particular geometric configuration seen in NGC 1365 should not be common at $z = 5$ either. Moreover, in this case, there is no direct evidence of a dusty torus, with several claims of LRDs being deficient in MIR emission (e.g. A. Graaff et al. 2025; D. J. Setton et al. 2025b; B. Wang et al. 2025), and the highest-redshift MIR detection of an LRD unambiguously attributed to a dusty torus being at $z = 2.26$ (J24). A rotating configuration is therefore possible in our case, although other absorbers have been measured with LOS velocities between -340 and $+50$ km s^{-1} (J. Matthee et al. 2024; J24; V. Rusakov et al. 2025), which are clearly inconsistent with rotation and favour non-equilibrium configurations.

While the remarkably low outflow velocity could be due to projection effects (with the inclination of the outflow axis close to $i \approx 90°$), this solution seems disfavoured too. For example, observing only $v_{\rm abs} = -13$ km s^{-1} from a typical deprojected outflow velocity of 350 km s^{-1} (S. Carniani et al. 2024), we would need $v_{\rm abs}/\cos i \equiv v_{\rm out} \leq -350$ km s^{-1} which requires $i \geq 88°$. For a randomly oriented galaxy, the corresponding probability is only $P < 0.04$. While this is not a small value, 159717 is already the third case of an absorbing cloud very near to rest frame (R. P. Naidu et al. 2025; F. D'Eugenio et al. 2025a), out of $\sim$10 LRDs with clearly detected absorption. This suggests that the low velocity is not due to projection, but reflects low intrinsic velocity.

This scenario would indicate therefore a long-lived cloud lingering near the SMBH, or even a 'stalling' outflow, caused by insufficient AGN power or by inefficient coupling (A. C. Fabian, R. V. Vasudevan & P. Gandhi 2008; N. Arakawa et al. 2022). Insufficient energy seems at odds with our relatively high Eddington ratio ($\lambda_{\rm E} = 0.45$). The other possibility, that feedback is inefficient, e.g. due to poor coupling with the gas, seems also unlikely. Such a scenario could be plausible in low-metallicity gas, if we assume that most of the opacity is driven by metals and dust (A. C. Fabian et al. 2008). However, in our case, the galaxy appears decidedly dusty, based on the narrow-line ratios ($A_V = 1 - 1.6$ mag) and the metallicity of the host galaxy seems fairly high too (> 0.06 Z$_\odot$; Table 2). Furthermore, our metallicity values could be underestimated, since any contribution from high-density regions to the [O III]λ4363 emission would decrease $T_{\rm e}$ and hence further increase metallicity (Section 6.2).

D. Kido et al. (2025) argue that typical LRDs occupy a region of the $M_\bullet$–$M_\star$ plane where strong outflows are expected. The general absence of such outflows in sources like 159717 therefore suggests an alternative scenario: the dense gas envelope model proposed by R. P. Naidu et al. (2025), A. Graaff et al. (2025), and D. Kido et al. (2025). In the case of 159717, not only is the combination of its large $M_\bullet/M_\star$ ratio and lack of outflows notable, but its relatively high $\lambda_{\rm Edd}$ and rest-frame Balmer absorption are also consistent with the predictions of the envelope model.

6.7 Breathing-mode accretion?

Hydrodynamic simulations of cold-gas accretion onto SMBHs which include radiative transfer suggest a self-regulated behaviour, with highly turbulent gas flows near the ionization front (K. Park, J. H. Wise & T. Bogdanović 2017; K. Inayoshi et al. 2022), but even in this case, the turbulence is 10 times lower than what inferred from our measurements.

K. Park et al. (2017) also find that during quiescent periods between bursts of accretion, the ionized bubble around the SMBH shrinks in size, leading to an increase in the density of the gas near and before the ionization front. Moreover, the dense gas is not dissipated, but following the accretion rate on the central SMBH, gives rise to an oscillatory behaviour of expansion and contraction. This 'breathing mode' of the gas could explain the observation of Hα absorption with a range of inflow, outflow, and rest velocities. Depending on the distance travelled, the gas would spend different amounts of time near the inversion points. The formation of a shell of neutral gas around accreting black holes is also consistent with the models of M. Milosavljević, S. M. Couch & V. Bromm (2009, for $M_\bullet \sim 100$ M$_\odot$) and K. Park & M. Ricotti (2012, for $M_\bullet = 100$–10^5 M$_\odot$), thus further supporting the presence of gas capable of Balmer absorption. If this breathing-mode picture is true, then the relative abundance of absorbers with different velocities could hold valuable information about the interface between the accreting SMBH and the host galaxy. As we have seen, the incidence of Balmer absorbers may be underestimated by current medium-resolution observations (Section 3.8). This is particularly true at high redshifts, where most LRD spectra use either the NIRSpec medium-resolution gratings or the prism (but to some extent, it is a problem also in the local Universe, where large surveys such as SDSS (Sload Digital Sky Survey) and LAMOST (Large Sky Area Multi-Object Fiber Spectroscopic Telescope) have $R \lesssim 2000$, in the relevant wavelength region). Clearly, current *JWST*/NIRSpec observations underestimate the total incidence of absorbers. The problem must be relatively more severe for rest-frame absorbers, since symmetric narrow-line infill would be more effective at removing the absorber, and would still result in a symmetric line profile. This suggests that the fraction of red- and blueshifted absorbers relative to rest-frame ones could also be overestimated by current data.

Still, key issues with the model of K. Park et al. (2017) remain, most notably the large discrepancy in density between their simulations and those inferred for LRD absorbers (10^9–10^{11}cm^{-3}; J24; X. Ji et al. 2025; R. P. Naidu et al. 2025). The models of K. Park et al. (2017) reach maximum densities of only 10 000 cm^{-3}. This discrepancy may be due to the *ad-hoc* assumptions of the K. Park et al. (2017) simulations, which may not consider the appropriate cosmological context for LRDs – particularly if LRDs occupy

somehow atypical dark-matter haloes compared to the general galaxy population (e.g. F. Pacucci & A. Loeb 2025). For instance, theory supports the possibility of rapid gas inflow towards the central region of galaxies (e.g. S. Tacchella et al. 2016). While these results apply to dark matter haloes that are more massive than for LRDs (E. Pizzati et al. 2025), recent zoom-in simulations such as THESAN-Zoom (R. Kannan et al. 2025; W. McClymont et al. 2025b) suggest that the accretion rate onto the central regions of lower mass, high-redshift galaxies can be substantial too, potentially supporting the accumulation of high-density gas near the SMBHs powering LRDs. However, while THESAN-Zoom preserves the cosmological context (R. Kannan et al. 2025), it still lacks the spatial resolution of high-resolution simulations like those of K. Park et al. (2017) and thus it cannot resolve the immediate environment around SMBHs. A promising path would be to use constraints from zoom-in simulations like THESAN-Zoom to supply the boundary conditions for even higher resolution simulations targeting galactic nuclei.

6.8 Soft ionizing spectrum

The absence of high-ionization lines in LRDs, including metallicity independent lines, such as He II, could be due to an intrinsically red SED (E. Lambrides et al. 2024; B. Wang et al. 2024), However, there are convincing reports of high-ionization UV lines in a few LRDs (I. Labbe et al. 2024; R. Tripodi et al. 2025; M. Tang et al. 2025; H. B. Akins et al. 2025b), while preliminary analysis suggests an incidence rate of ~ 12 per cent across the population (M. Tang et al. 2025), albeit with large uncertainties. A possibility to reconcile these differences is that ionizing photons from an intrinsically hard SED are being absorbed by hydrogen (K. Inayoshi & R. Maiolino 2025; X. Ji et al. 2025; R. P. Naidu et al. 2025). This would be in agreement with the weakness of some bright LRDs at MIR and far-IR wavelengths (D. J. Setton et al. 2025b). This hydrogen absorption should drive DLA and possibly a Balmer break, which are not seen in this and in many other LRDs (e.g. J. E. Greene et al. 2024; I. Juodžbalis et al. 2025; V. Rusakov et al. 2025). Arguably, the Balmer break could be hidden by dust reddening, which in this and in other objects is inferred independently from the Balmer decrement (e.g.M. Killi et al. 2024; J24; F. D'Eugenio et al. 2025a), in combination with outshining from the host galaxy (R. P. Naidu et al. 2025). Either way, if Balmer breaks were common to all LRDs (whether hidden or not), we should always see Balmer-line absorption. While this is seemingly contradicted by current observations, we showed that this conclusion may be driven by inadequate spectral resolution (Section 3.8). Future surveys using high-resolution spectroscopy would be an easy way to check the incidence of (possibly hidden) Balmer breaks.

7 CONCLUSIONS

We presented the broad-line AGN 159717 at $z \approx 5.077$, observed by the JADES and BlackTHUNDER programmes using *JWST*/NIRCam, NIRSpec/MSA in multiple dispersers, and NIRSpec/IFS. While a full analysis of this system is complicated by the foreground system, extensive *JWST* data and deep, multi-epoch high-resolution observations provide new insights into the nature of low-luminosity, 'LRD' AGN.

(i) The prism spectroscopy shows a 'v'-shaped continuum spectrum (Fig. 1), characterizing this source as an LRD. In the medium- and high-resolution spectrum, the Hα line has multiple components, including two broad Gaussians, with an overall broad-component width FWHM $= 1510 \pm 70$ km s^{-1}. [O III]λ5007 has a narrow $\sigma_{\rm n} = 47$–54 km s^{-1} (FWHM $= 127$ km s^{-1}). Combined, this is evidence for a BLR.

(ii) The resulting SMBH mass of $\log M_\bullet/{\rm M}_\odot = 7.5$ dex places 159717 very near the $M_\bullet - \sigma$ scaling relation of nearby galaxies. From the dynamical mass, used as an upper limit on $M_\star$, we infer that the SMBH is overmassive relative to the local scaling relations (Fig. 17).

(iii) The overmassive nature of 159717 remains true (but less severe) even if we model the broad line as a single Gaussian plus electron scattering (V. Rusakov et al. 2025).

(iv) The metallicity of this system from the direct method is 0.06 Z$_\odot$; while 159717 is metal poor, it is far from pristine, also in agreement with the large Balmer decrement of the narrow Balmer lines ($A_V = 1.0 \pm 0.2$ mag).

(v) Far from being isolated, 159717 is found in the process of interacting with a companion, 159716, in what is a possible major merger. Interestingly, 159716 exhibits a Balmer break likely driven by a recent period of lowered star formation. Another source, 159717B, may be material stripped from 159716, while the whole triple is immersed in a pool of [O III]λ5007 emitting gas. The merger may be helping in funnelling gas towards the central regions of 159717, ultimately feeding the SMBH.

(vi) Despite their differences in luminosity, morphology, and AGN presence, the three sources have similar ionization properties, such as a similar location on the BPT diagram.

(vii) One more source, 159717C, is spatially detached. Its higher ionization and dispersion suggest a possible outflow origin. If confirmed, this would be the first evidence of kpc-scale AGN feedback in an LRD.

(viii) Hα presents clear absorption with velocity and velocity dispersion of $v_{\rm abs} = -13$ km s^{-1} and $\sigma_{\rm abs} = 120$ km s^{-1}. We interpret the low projected velocity and large turbulence as a 'stalling' outflow, or lingering gas cloud.

(ix) Intriguingly, there is tentative evidence (2.6σ) of time variability in the EW of the Hα absorber. If confirmed, this would indicate a highly dynamic environment.

(x) This LRD, like others, lacks high-ionization lines, which could be due to hydrogen bound-free absorption. We do not observe a Balmer break, but this could be due to dust attenuation, since dust is seen in the narrow lines too. If Balmer breaks were widespread in LRDs (including many hidden by dust), this should still give rise to Balmer line absorption.

(xi) We highlight that the absorber in 159717, despite being clearly evident and even dominant in the *G*395*H* observations, is not detected in the medium-resolution *G*395*M* data, implying that current incidence of absorbers may be severely underestimated.

These findings resonate with earlier results pointing to LRDs being 'more than just a dot' (P. Rinaldi et al. 2025). The presence of rest-frame Balmer absorption, determined here with unprecedented precision, highlights how dense gas near LRDs may display properties that are not common in massive SMBHs, as highlighted by several studies (K. Inayoshi & R. Maiolino 2025; X. Ji et al. 2025; R. P. Naidu et al. 2025; V. Rusakov et al. 2025; F. D'Eugenio et al. 2025a; Y. Ma et al. 2025a). Overall, our findings highlight the exciting opportunities offered by multi-epoch, high-resolution observations of LRDs, to investigate both their local environment, SMBHs, and time variability. The use of high-resolution NIRSpec spectroscopy is essential for a complete census of gas absorbers in broad-line AGN, because estimates based on NIRSpec medium-resolution spectroscopy may severely underestimate the incidence of absorbers (Fig. 7).

ACKNOWLEDGEMENTS

We thank Debora Sijacki, Sergio Martin-Alvarez, William McClymont, Gabriele Pezzulli, and Harley Katz for useful discussions. FDE, RM, XJ, JS, IJ, and GCJ acknowledge support by the Science and Technology Facilities Council (STFC), by the ERC through Advanced Grant 695671 'QUENCH', and by the UKRI Frontier Research grant RISEandFALL. RM also acknowledges funding from a research professorship from the Royal Society. IJ also acknowledges support by the Huo Family Foundation through a P.C. Ho PhD Studentship. MP, SA, and BRP acknowledge grant PID2021-127718NB-I00 funded by the Spanish Ministry of Science and Innovation/State Agency of Research (MICIN/AEI/ 10.13039/501100011033). MP also acknowledges the grant RYC2023-044853-I, funded by MICIU/AEI/10.13039/501100011033 and European Social Fund Plus (FSE+). GM and HÜ acknowledge funding by the European Union (ERC APEX, 101164796). Views and opinions expressed are however those of the authors only and do not necessarily reflect those of the European Union or the European Research Council Executive Agency. Neither the European Union nor the granting authority can be held responsible for them. SC and GV acknowledge support by European Union's HE ERC Starting grant no. 101040227 – WINGS. AJB acknowledges funding from the 'FirstGalaxies' Advanced Grant from the European Research Council (ERC) under the European Union's Horizon 2020 research and innovation program (grant agreement no. 789056). ECL acknowledges support of an STFC Webb Fellowship (ST/W001438/1). KI acknowledges support from the National Natural Science Foundation of China (12073003, 11721303, and 11991052), and the China Manned Space Project (CMS-CSST-2021-A04 and CMS-CSST-2021-A06). YI is supported by JSPS KAKENHI grant no. 24KJ0202. ZJ, BDJ, BER, and CNAW acknowledge support from the NIRCam Science Team contract to the University of Arizona, NAS5-02015. BER also acknowledges support from *JWST* Program 3215. ST acknowledges support by the Royal Society Research Grant G125142. The research of CCW is supported by NOIRLab, which is managed by the Association of Universities for Research in Astronomy (AURA) under a cooperative agreement with the National Science Foundation. JW gratefully acknowledges support from the Cosmic Dawn Center through the DAWN Fellowship. The Cosmic Dawn Center (DAWN) is funded by the Danish National Research Foundation under grant no. 140. The authors acknowledge use of the lux supercomputer at UC Santa Cruz, funded by NSF MRI grant AST 1828315.

This work is based on observations made with the NASA/ESA/CSA *James Webb Space Telescope*. The data were obtained from the Mikulski Archive for Space Telescopes at the Space Telescope Science Institute, which is operated by the Association of Universities for Research in Astronomy, Inc., under NASA contract NAS 5-03127 for *JWST*. These observations are associated with program no.1286.

This work made extensive use of the freely available Debian GNU/Linux operating system. We used the PYTHON programming language (G. Rossum 1995), maintained and distributed by the Python Software Foundation. We made direct use of PYTHON packages ASTROPY (Astropy Collaboration 2013, 2018), CORNER (D. Foreman-Mackey 2016), EMCEE (D. Foreman-Mackey et al. 2013), JWST (C. Alves de Oliveira et al. 2018), MATPLOTLIB (J. D. Hunter 2007), NUMPY (C. R. Harris et al. 2020), PROSPECTOR (B. D. Johnson et al. 2021) v2.0, PYNEB (V. Luridiana et al. 2015), PYTHON-FSPS (B. Johnson et al. 2023), PYSERSIC (I. Pasha & T. B. Miller 2023), QUBESPEC (J. Scholtz et al. 2025b), and SCIPY (E. Jones et al. 2001). We also used the software packages FSPS (C. Conroy et al. 2009; C. Conroy & J. E. Gunn 2010), TOPCAT (M. B. Taylor 2005), FITSMAP (R. Hausen & B. E. Robertson 2022), and DS9 (W. A. Joye & E. Mandel 2003).

DATA AVAILABILITY

The data used in this article are all available through the MAST archive. The JADES data are publicly available also on the JADES Collaboration website. The specific data-reduction version used in this work has been published in F. D'Eugenio et al. (2025d, 10.17909/8tdj-8n28). The most recent updates to the reduction have been presented in J. Scholtz et al. (2025a).

REFERENCES

Abuter R. et al., 2024, Nature, 627, 281
Akins H. B. et al., 2025a, preprint (arXiv:2503.00998)
Akins H. B. et al., 2025b, ApJ, 980, L29
Akins H. B. et al., 2025c, ApJ, 991, 37
Alberts S. et al., 2024, ApJ, 975, 85
Alves de Oliveira C. et al., 2018, in Peck A. B., Seaman R. L., Benn C. R., eds, Proc. Conf Ser. Vol. 10704, Observatory Operations: Strategies, Processes, and Systems VII. SPIE, Bellingham, p. 107040Q
Arakawa N., Fabian A. C., Ferland G. J., Ishibashi W., 2022, MNRAS, 517, 5069
Asplund M., Grevesse N., Sauval A. J., Scott P., 2009, ARA&A, 47, 481
Astropy Collaboration, 2013, A&A, 558, A33
Astropy Collaboration, 2018, AJ, 156, 123
Baggen J. F. W. et al., 2024, ApJ, 977, L13
Baker W. M. et al., 2025, MNRAS, 539, 557
Baldwin J. A., Phillips M. M., Terlevich R., 1981, PASP, 93, 5
Baldwin J. A., Ferland G. J., Korista K. T., Hamann F., LaCluyzé A., 2004, ApJ, 615, 610
Baskin A., Laor A., 2005, MNRAS, 358, 1043
Behroozi P. S., Conroy C., Wechsler R. H., 2010, ApJ, 717, 379
Behroozi P. S., Wechsler R. H., Conroy C., 2013, ApJ, 770, 57
Bennert V. N. et al., 2021, ApJ, 921, 36
Bertemes C. et al., 2025, A&A, 693, A176
Bertin E., Arnouts S., 1996, A&AS, 117, 393
Bezanson R. et al., 2018, ApJ, 868, L36
Binette L. et al., 2024, A&A, 684, A53
Böker T. et al., 2022, A&A, 661, A82
Bouwens R. J. et al., 2015, ApJ, 803, 34
Brammer G. B., van Dokkum P. G., Coppi P., 2008, ApJ, 686, 1503
Brooks M. et al., 2025, ApJ, 986, 177
Bullock J. S., Kolatt T. S., Sigad Y., Somerville R. S., Kravtsov A. V., Klypin A. A., Primack J. R., Dekel A., 2001, MNRAS, 321, 559
Bunker A. J., NIRSPEC Instrument Science Team, JADES Collaboration, 2020, in da Cunha E., Hodge J., Afonso J., Pentericci L., Sobral D., eds, Proc. IAU Symp. Vol. 352, Uncovering Early Galaxy Evolution in the ALMA and JWST Era. Cambridge Univ. Press, Cambridge, p. 342
Bunker A. J. et al., 2023, A&A, 677, A88
Bunker A. J. et al., 2024, A&A, 690, A288
Byler N., Dalcanton J. J., Conroy C., Johnson B. D., 2017, ApJ, 840, 44
Cameron A. J. et al., 2023, A&A, 677, A115
Cameron A. J., Katz H., Witten C., Saxena A., Laporte N., Bunker A. J., 2024, MNRAS, 534, 523
Cardelli J. A., Clayton G. C., Mathis J. S., 1989, ApJ, 345, 245
Carniani S. et al., 2024, A&A, 685, A99
Carniani S. et al., 2025, A&A, 696, A87
Carranza-Escudero M. et al., 2025, ApJ, 989, L50
Casey C. M., Akins H. B., Kokorev V., McKinney J., Cooper O. R., Long A. S., Franco M., Manning S. M., 2024, ApJ, 975, L4
Casey C. M. et al., 2025, ApJ, 990, L61
Chabrier G., 2003, PASP, 115, 763
Charlot S., Fall S. M., 2000, ApJ, 539, 718
Chen C.-H., Ho L. C., Li R., Inayoshi K., 2025, ApJ, 989, L12

Choi J., Dotter A., Conroy C., Cantiello M., Paxton B., Johnson B. D., 2016, ApJ, 823, 102
Cole J. W. et al., 2025, ApJ, 979, 193
Conroy C., Gunn J. E., 2010, Astrophysics Source Code Library, record ascl:1010.043
Conroy C., Gunn J. E., White M., 2009, ApJ, 699, 486
Conroy C., Naidu R. P., Zaritsky D., Bonaca A., Cargile P., Johnson B. D., Caldwell N., 2019, ApJ, 887, 237
D'Eugenio F. et al., 2024, Nat. Astron., 8, 1443
D'Eugenio F. et al., 2025a, preprint (arXiv:2503.11752)
D'Eugenio F. et al., 2025b, preprint (arXiv:2510.00101)
D'Eugenio F. et al., 2025c, preprint (arXiv:2510.11626)
D'Eugenio F. et al., 2025d, ApJS, 277, 4
D'Eugenio F. et al., 2025e, MNRAS, 536, 51
D'Eugenio F. et al., 2025f, MNRAS, 542, 960
Dalla Bontà E. et al., 2025, A&A, 696, A48
Davies R. L. et al., 2024, MNRAS, 528, 4976
de Graaff A. et al., 2024, A&A, 684, A87
de Graaff A. et al., 2025, A&A, 701, A168
Ding X. et al., 2023, Nature, 621, 51
Dojčinović I., Kovačević-Dojčinović J., Popović L. Č., 2023, Adv. Space Res., 71, 1219
Dong X., Wang T., Wang J., Yuan W., Zhou H., Dai H., Zhang K., 2008, MNRAS, 383, 581
Dors O. L., Maiolino R., Cardaci M. V., Hägele G. F., Krabbe A. C., Pérez-Montero E., Armah M., 2020, MNRAS, 496, 3209
Dutton A. A., Macciò A. V., 2014, MNRAS, 441, 3359
Eisenstein D. J. et al., 2023, preprint (arXiv:2306.02465)
Eisenstein D. J. et al., 2025, ApJS, 281, 50
Fabian A. C., Vasudevan R. V., Gandhi P., 2008, MNRAS, 385, L43
Ferruit P. et al., 2022, A&A, 661, A81
Foreman-Mackey D., 2016, J. Open Source Softw., 1, 24
Foreman-Mackey D., Hogg D. W., Lang D., Goodman J., 2013, PASP, 125, 306
Fridman A. M., Poliachenko V. L., 1984, Physics of Gravitating Systems. II – Nonlinear Collective Processes: Nonlinear Waves, Solitons, Collisionless Shocks, Turbulence. Astrophysical Applications. Springer-Verlag, New York
Furtak L. J. et al., 2023, ApJ, 952, 142
Furtak L. J. et al., 2024, Nature, 628, 57
Furtak L. J. et al., 2025, A&A, 698, A227
Giavalisco M. et al., 2004, ApJ, 600, L93
Gordon K. D., Clayton G. C., Misselt K. A., Landolt A. U., Wolff M. J., 2003, ApJ, 594, 279
Goulding A. D. et al., 2023, ApJ, 955, L24
Greene J. E., Ho L. C., 2004, ApJ, 610, 722
Greene J. E., Ho L. C., Ulvestad J. S., 2006, ApJ, 636, 56
Greene J. E., Strader J., Ho L. C., 2020, ARA&A, 58, 257
Greene J. E. et al., 2024, ApJ, 964, 39
Greene T. P. et al., 2017, J. Astron. Telesc. Instrum. Syst, 3, 035001
Grogin N. A. et al., 2011, ApJS, 197, 35
Hainline K. N. et al., 2024, ApJ, 964, 71
Harikane Y. et al., 2023, ApJ, 959, 39
Harris C. R. et al., 2020, Nature, 585, 357
Hausen R., Robertson B. E., 2022, Astron. Comput., 39, 100586
Hunter J. D., 2007, Comput. Sci. Eng., 9, 90
Ilić D., Popović L. Č., La Mura G., Ciroi S., Rafanelli P., 2012, A&A, 543, A142
Inayoshi K., Maiolino R., 2025, ApJ, 980, L27
Inayoshi K., Nakatani R., Toyouchi D., Hosokawa T., Kuiper R., Onoue M., 2022, ApJ, 927, 237
Izotov Y. I., Stasińska G., Meynet G., Guseva N. G., Thuan T. X., 2006, A&A, 448, 955
Isobe Y., Ouchi M., Nakajima K., Harikane Y., Ono Y., Xu Y., Zhang Y., Umeda H., 2023, ApJ, 956, 139
Izumi T. et al., 2021, ApJ, 914, 36
Jakobsen P. et al., 2022, A&A, 661, A80
Ji X. et al., 2025, MNRAS, 544, 3900
Ji Z. et al., 2024, ApJ, 974, 135
Johnson B. D., Leja J., Conroy C., Speagle J. S., 2021, ApJS, 254, 22
Johnson B. et al., 2023, dfm/python-fsps: v0.4.4, Zenodo, https://doi.org/10.5281/zenodo.8230430
Jones E., et al., 2001, SciPy: Open source scientific tools for Python, http://www.scipy.org/
Jones G. C. et al., 2024, A&A, 683, A238
Jones G. C. et al., 2025, preprint (arXiv:2509.20455)
Joye W. A., Mandel E., 2003, in Payne H. E., Jedrzejewski R. I., Hook R. N., eds, ASP Conf. Ser. Vol. 295, Astronomical Data Analysis Software and Systems XII. Astron. Soc. Pac., San Francisco, p. 489
Juodžbalis I. et al., 2024a, MNRAS, 535, 853
Juodžbalis I. et al., 2024b, Nature, 636, 594
Juodžbalis I. et al., 2025, preprint (arXiv:2504.03551)
Kannan R. et al., 2025, Open J. Astrophys., 8, 153
Kauffmann G. et al., 2003, MNRAS, 346, 1055
Kewley L. J., Dopita M. A., Sutherland R. S., Heisler C. A., Trevena J., 2001, ApJ, 556, 121
Kewley L. J., Groves B., Kauffmann G., Heckman T., 2006, MNRAS, 372, 961
Kido D., Ioka K., Hotokezaka K., Inayoshi K., Irwin C. M., 2025, MNRAS, 544, 3547
Killi M. et al., 2024, A&A, 691, A52
Kocevski D. D. et al., 2023, ApJ, 954, L4
Kocevski D. D. et al., 2025, ApJ, 986, 126
Koekemoer A. M. et al., 2011, ApJS, 197, 36
Kokorev V. et al., 2023, ApJ, 957, L7
Kokubo M., Harikane Y., 2025, ApJ, 995, 24
Kormendy J., Ho L. C., 2013, ARA&A, 51, 511
Koudmani S., Sijacki D., Smith M. C., 2022, MNRAS, 516, 2112
Kriek M., Conroy C., 2013, ApJ, 775, L16
Labbe I. et al., 2024, preprint (arXiv:2412.04557)
Lambrides E. et al., 2024, preprint (arXiv:2409.13047)
Laor A., 2006, ApJ, 643, 112
Li Y., Leja J., Johnson B. D., Tacchella S., Naidu R. P., 2024, ApJ, 969, L5
Li J., Shen Y., Zhuang M.-Y., 2025, preprint (arXiv:2502.05048)
Luo B. et al., 2017, ApJS, 228, 2
Luridiana V., Morisset C., Shaw R. A., 2015, A&A, 573, A42
Ma Y. et al., 2025a, preprint (arXiv:2504.08032)
Ma Y. et al., 2025b, ApJ, 981, 191
Maiolino R. et al., 2010, A&A, 517, A47
Maiolino R. et al., 2024, A&A, 691, A145
Maiolino R. et al., 2025a, preprint (arXiv:2505.22567)
Maiolino R. et al., 2025b, MNRAS, 538, 1921
Marshall M. A. et al., 2025, A&A, 702, A50
Mascia S. et al., 2024, A&A, 690, A2
Matthee J. et al., 2024, ApJ, 963, 129
Mazzolari G. et al., 2024, A&A, 691, A345
McClymont W. et al., 2025a, MNRAS, 540, 190
McClymont W. et al., 2025b, MNRAS, 544, 513
Mérida R. M. et al., 2025, A&A, 698, A317
Merritt D., Hernquist L., 1991, ApJ, 376, 439
Miller T. B. et al., 2025, ApJ, 988, 196
Milosavljević M., Couch S. M., Bromm V., 2009, ApJ, 696, L146
Moster B. P., Somerville R. S., Maulbetsch C., van den Bosch F. C., Macciò A. V., Naab T., Oser L., 2010, ApJ, 710, 903
Moster B. P., Naab T., White S. D. M., 2013, MNRAS, 428, 3121
Naidu R. P. et al., 2025, preprint (arXiv:2503.16596)
Navarro J. F., Frenk C. S., White S. D. M., 1997, ApJ, 490, 493
Nikopoulos G. P., Watson D., Sneppen A., Rusakov V., Heintz K. E., Witstok J., Brammer G., 2025, preprint (arXiv:2510.06362)
Noll S., Burgarella D., Giovannoli E., Buat V., Marcillac D., Muñoz-Mateos J. C., 2009, A&A, 507, 1793
Oesch P. A. et al., 2023, MNRAS, 525, 2864
Oke J. B., Gunn J. E., 1983, ApJ, 266, 713
Osterbrock D. E., Ferland G. J., 2006, Astrophysics of Gaseous Nebulae and Active Galactic Nuclei. University Science Books, Sausalito, CA
Pacucci F., Loeb A., 2025, ApJ, 989, L19

Pacucci F., Narayan R., 2024, ApJ, 976, 96
Park K., Ricotti M., 2012, ApJ, 747, 9
Park K., Wise J. H., Bogdanović T., 2017, ApJ, 847, 70
Pasha I., Miller T. B., 2023, J. Open Source Softw., 8, 5703
Peng C. Y., Ho L. C., Impey C. D., Rix H.-W., 2002, AJ, 124, 266
Peng C. Y., Ho L. C., Impey C. D., Rix H.-W., 2010, AJ, 139, 2097
Pérez-González P. G. et al., 2024, ApJ, 968, 4
Perna M. et al., 2023, A&A, 679, A89
Perna M. et al., 2025, A&A, 696, A59
Pizzati E., Hennawi J. F., Schaye J., Eilers A.-C., Huang J., Schindler J.-T., Wang F., 2025, MNRAS, 539, 2910
Planck Collaboration VI, 2020, A&A, 641, A6
Rauscher B. J. et al., 2012, in Holland A. D., Beletic J. W., eds, Proc. SPIE Conf. Ser. Vol. 8453, High Energy, Optical, and Infrared Detectors for Astronomy V. SPIE, Bellingham, p. 84531F
Rauscher B. J. et al., 2017, PASP, 129, 105003
Reines A. E., Volonteri M., 2015, ApJ, 813, 82
Rieke M., 2020, in da Cunha E., Hodge J., Afonso J., Pentericci L., Sobral D., eds, Proc. IAU Symp. Vol. 352, Uncovering Early Galaxy Evolution in the ALMA and JWST Era. Cambridge Univ. Press, Cambridge, p. 337
Rieke M. J. et al., 2023, ApJS, 269, 16
Rinaldi P. et al., 2025, ApJ, 992, 71
Rudy R. J., Rossano G. S., Puetter R. C., 1989, ApJ, 342, 235
Rupke D. S., Veilleux S., Sanders D. B., 2005, ApJS, 160, 115
Rusakov V. et al., 2025, preprint (arXiv:2503.16595)
Sanders R. L. et al., 2016, ApJ, 816, 23
Sandles L. et al., 2024, A&A, 691, A305
Satyapal S., Secrest N. J., McAlpine W., Ellison S. L., Fischer J., Rosenberg J. L., 2014, ApJ, 784, 113
Schawinski K., Thomas D., Sarzi M., Maraston C., Kaviraj S., Joo S.-J., Yi S. K., Silk J., 2007, MNRAS, 382, 1415
Schlafly E. F., Finkbeiner D. P., 2011, ApJ, 737, 103
Scholtz J. et al., 2025a, preprint (arXiv:2510.01034)
Scholtz J. et al., 2025b, MNRAS, 539, 2463
Scholtz J. et al., 2025c, A&A, 697, A175
Schramm M. et al., 2013, ApJ, 773, 150
Schwarz G., 1978, Ann. Stat., 6, 461
Setton D. J. et al., 2025a, ApJ, 995, 118
Setton D. J. et al., 2025b, ApJ, 991, L10
Shapley A. E., Sanders R. L., Reddy N. A., Topping M. W., Brammer G. B., 2023, ApJ, 954, 157
Silk J., 2017, ApJ, 839, L13
Simmonds C. et al., 2025, MNRAS, 544, 4551
Smith K. C., Howarth I. D., 1998, MNRAS, 299, 1146
Stern J., Laor A., 2012, MNRAS, 423, 600
Stone M. A., Lyu J., Rieke G. H., Alberts S., 2023, ApJ, 953, 180
Storey P. J., Zeippen C. J., 2000, MNRAS, 312, 813
Stott J. P. et al., 2016, MNRAS, 457, 1888
Strom A. L. et al., 2023, ApJ, 958, L11
Sun Y. et al., 2025, ApJ, 978, 98
Tacchella S., Dekel A., Carollo C. M., Ceverino D., DeGraf C., Lapiner S., Mandelker N., Primack Joel R., 2016, MNRAS, 457, 2790
Tacchella S., Bose S., Conroy C., Eisenstein D. J., Johnson B. D., 2018, ApJ, 868, 92
Tacchella S. et al., 2022, ApJ, 926, 134
Tacchella S. et al., 2025, MNRAS, 540, 851
Tanaka T. S. et al., 2024, preprint (arXiv:2412.14246)
Tang M. et al., 2025, ApJ, 991, 217
Taylor A. J. et al., 2025, ApJ, 986, 165
Taylor M. B., 2005, in Shopbell P., Britton M., Ebert R., eds, ASP Conf. Ser. Vol. 347, Astronomical Data Analysis Software and Systems XIV. Astron. Soc. Pac., San Francisco, p. 29
Terp C., Heintz K. E., Watson D., Brammer G., Carnall A., Witstok J., Smit R., Vejlgaard S., 2024, A&A, 690, A70
Torralba A. et al., 2025a, preprint (arXiv:2505.09542)
Torralba A. et al., 2025b, preprint (arXiv:2510.00103)
Tripodi R. et al., 2025, Nat. Commun., 16, 9830
Turner C. et al., 2025, MNRAS, 537, 1826
Übler H. et al., 2023, A&A, 677, A145
Übler H. et al., 2024, MNRAS, 531, 355
Übler H. et al., 2025, preprint (arXiv:2509.21575)
van der Wel A. et al., 2012, ApJS, 203, 24
van der Wel A. et al., 2022, ApJ, 936, 9
van Dokkum P. G., 2001, PASP, 113, 1420
van Rossum G., 1995, CWI Technical Report, CS-R9526, CWI, Amsterdam
Veilleux S., Osterbrock D. E., 1987, ApJS, 63, 295
Veilleux S., Cecil G., Bland-Hawthorn J., 2005, ARA&A, 43, 769
Wang B. et al., 2024, ApJ, 969, L13
Wang B. et al., 2025, ApJ, 984, 121
Whitaker K. E. et al., 2019, ApJS, 244, 16
Williams C. C. et al., 2024, ApJ, 968, 34
Wu S. et al., 2024, MNRAS, 532, 4703
Yue M. et al., 2024a, ApJ, 966, 176
Yue M., Eilers A.-C., Ananna T. T., Panagiotou C., Kara E., Miyaji T., 2024b, ApJ, 974, L26
Zamora S. et al., 2025, A&A, 702, A102
Zhang Z., Jiang L., Liu W., Ho L. C., 2025, ApJ, 985, 119

APPENDIX A: INTERLOPING GALAXY.

Emission from 159717 is plagued by a foreground spiral galaxy, JADES ID 159715 (Fig. 1a). By inspecting *HST* imaging at wavelengths shorter than 7000 Å (the Lyα drop in 159717), we can readily identify a star-forming region near to the LOS to 159717; this region is detected in [O III]$\lambda\lambda$4959,5007 and Hα in the 2D and 1D NIRSpec spectra (see Fig. 1). The redshift of these emission lines is consistent with what found from the BlackTHUNDER high-resolution spectrum, where we find Paα at 3.75 μm, giving a redshift of $z_{\rm spec} = 1.00115 \pm 0.00001$. This is independently confirmed by F. D'Eugenio et al. (2025c) using deeper grating observations in *G*235*M* and *G*395*M*.

To analyse this lower redshift interloper, we start by correcting the *G*140*M*/*F*070*LP* spectrum for foreground Milky-Way attenuation, using the J. A. Cardelli, G. C. Clayton & J. S. Mathis (1989) extinction law with $E(B-V) = 0.0067$ from E. F. Schlafly & D. P. Finkbeiner (2011). This has minimal impact (0.02 mag) on the recovered A_V. We extract the 1D spectrum from three spaxels of the JADES 2D spectrum, identified from the 2D SNR map as displaying clear evidence of [O III]λ5007 emission in the prism spectrum (cf. Fig. 1b). The resulting spectrum is shown in Fig. A1, with clear evidence of both [O III]$\lambda\lambda$4959,5007 (panel a) and Hα (panel b), while Hβ is superimposed to a noise feature. We model this spectrum using two local backgrounds around H β–[O III]$\lambda\lambda$4959,5007 and Hβ, and four Gaussians, the latter having the same redshift and (instrument-convolved) velocity dispersion. The Hα flux is a free parameter, while the Hβ flux is derived from Hα assuming the intrinsic Case-B recombination ratio of 2.86 for $T_{\rm e} = 10\,000$ K and $n_{\rm e} = 100$ cm^{-3}, and a G03 dust law with free A_V. We also limit the observed [O III]λ5007/H β ratio to be less than 20, which effectively limits A_V to realistic values of $A_V < 3$ mag. The model is fit to the data using the Bayesian approach described in Sections 3.2 and 3.3. We find a redshift $z_{\rm spec} = 1.0012 \pm 0.0002$, higher than the fiducial value from BlackTHUNDER, but still compatible, given the known wavelength calibration discrepancies between different NIRSpec dispersers (e.g. F. D'Eugenio et al. 2025d). The resulting dust attenuation is $A_V = 0.4^{+0.7}_{-0.3}$ mag, consistent with no attenuation. A consistent result is obtained by fitting jointly Paα together with Hβ, [O III]$\lambda\lambda$4959,5007 and Hα, where we assume an intrinsic Paα/Hβ = 0.339, consistent with the assumptions for the intrinsic Hα/H β. This fit is performed on the prism spectrum, because Paα is not detected in the gratings. This model gives $A_V = 0.4^{+0.5}_{-0.3}$ mag.

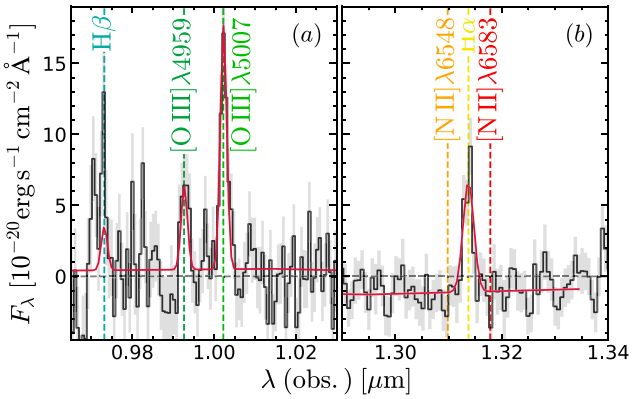

Figure A1. Medium-resolution *G*140*M* grating data of the interloping star-forming regions from galaxy 159715. The model (red) assumes a physically motivated Hα/H β ratio, due to a noise spike at the location of Hβ. Background over-subtraction is present throughout the spectrum, due to the spatial footprint of the main target 159717 and of the interloper itself on the NIRSpec shutters (Fig. 1a).

The most stringent constraints come from the BlackTHUNDER data; we extract prism spectra from two apertures, one centred on the target AGN, and one capturing the brightest star-forming region to the north-west of the AGN. Modelling these spectra yields respectively $A_V = 0.35 \pm 0.15$ and 0.55 ± 0.10 mag. Of these two values, the most relevant one for the foreground screen is the lowest, given that it is closer to the LOS of 159717.

In any case, Hβ and Hα light from 159717 passing through the interloper had observed-frame wavelengths of 1.48 and 1.99 μm. At these wavelengths, with the fiducial $A_V = 0.35$ of the interloper, the attenuation would be dominated by dust within 159717, with a foreground attenuation of only 6 and 4 per cent for Hβ and Hα, respectively.

To assess the Lyα emission, we compare the spatial distribution of secure emission lines in the main 159717 and in the interloper. In Fig. A2(a), we use the BlackTHUNDER prism data to create emission-line maps at the wavelengths of [O III]λ5007 at $z = 5.078$ (cyan), of [O III]λ5007 at $z = 1$ (magenta), and at the coincident wavelengths of Lyα (at $z = 5.078$) and [O II]λλ3726,3729(at $z = 1$; black contours). The cyan contours are clearly misaligned with respect to the black contours, but this in itself is not sufficient reason to discard the Lyα interpretation, since Lyα can have substantially different morphology than optically thin emission lines (e.g. A. Torralba et al. 2025a). To further test the Lyα or [O II]λλ3726,3729 origin of the black contours, all emission-line contours are overlaid on a RGB image that shows the rest-frame UV and optical from the interloper in *HST*/ACS *F*606*W* and *JWST*/NIRCam *F*090*W*, respectively. UV-bright regions are seen in pink hues, and coincide with the core of the foreground galaxy and with its northern spiral arm. The latter also coincides perfectly with both the northern magenta contour ([O III]λ5007 at $z = 1$) and with the black contours, suggesting the latter should be conservatively identified as [O II]λλ3726,3729 arising

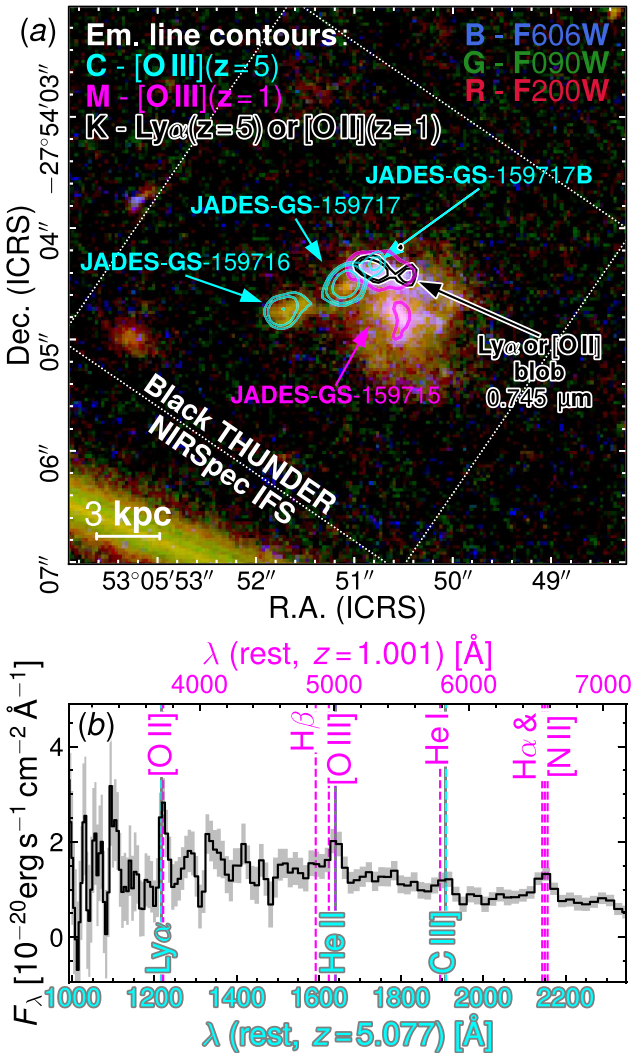

Figure A2. Panel (a): a morphological analysis favours interpreting the 0.745-μm emission line (black contours) as [O II]λλ3726,3729 from the $z = 1$ interloper, instead of Lyα from 159717. The false-colour RGB image highlights in blue the bulge of JADES ID 159715 and a star-forming spiral arm just north of the bulge. The contours show the location of various emission lines from the BlackTHUNDER prism observations. The 0.745-μm line emission coincides spatially and morphologically with the star-forming spiral arm of JADES ID 159715, which is also traced by the [O III]λ5007 emission line at $z = 1$ (magenta). In contrast, [O III]λ5007 at $z = 5.0775$ (cyan) is either spatially offset (159717 and 159716), or morphologically different (159717B). Panel (b) reports the prism spectrum, annotating notable emission lines at the two redshift solutions.

from the foreground. The prism spectrum is shown in Fig. A2(b), where the top and bottom axes report the rest-frame wavelengths for 159715 and 159717, respectively. We annotate notable emission lines for the two redshift solutions. Note that [O III]λλ4959,5007 and Hα are independently confirmed by the *G*140*M* detection (Fig. A1).

APPENDIX B: GRAVITATIONAL LENS

Finding a bright LRD within only 0.6-arcsec separation from a foreground galaxy raises the question of possible gravitational-lens magnification $\mu_{\rm lens}$. To evaluate this possibility and to infer $\mu_{\rm lens}$, we need to estimate the mass of the lens galaxy inside the circle of radius $\theta = 0.6$ arcsec, corresponding to 4.94 kpc at $z = 1.00115$. We start from the stellar mass measurement $M_\star = 10^{8.9}$ M$_\odot$ from the CANDELS catalogue (N. A. Grogin et al. 2011; A. M. Koekemoer et al. 2011), and we use the stellar-to-halo mass relation of (P. S. Behroozi, R. H. Wechsler & C. Conroy 2013) to derive a dark-matter halo mass of $M_{\rm DM} = 10^{11.8}$ M$_\odot$, with a scatter of 0.2–0.3 dex (P. S. Behroozi et al. 2013; B. P. Moster, T. Naab & S. D. M. White 2013). For this halo, the virial radius is $R_{\rm vir} = 90$ kpc (J. S. Bullock et al. 2001). Assuming an NFW profile (J. F. Navarro, C. S. Frenk & S. D. M. White 1997), and a concentration value $c = 7$–10 (A. A. Dutton & A. V. Macciò 2014), we can estimate both the scale density and scale radius of the NFW profile, from which we derive enclosed masses of $M_{\rm DM}(R < 4.94\ {\rm kpc}) = 3.3$–$2.7 \times 10^{10}$ M$_\odot$. This value is still much larger than $M_\star$, without even considering that some of the stellar mass lies beyond the separation radius $\theta = 0.6$ arcsec, because the half-light radius of the lens is $R_{\rm e} = 0.43 \pm 0.05$ arcsec (A. der Wel et al. 2012). We derive a magnification factor $\mu_{\rm lens} < 1.1$, which is below the typical uncertainties on both $M_\star$, $R_{\rm e}$, and $M_\bullet$. From similar considerations, applied to the source 159717C (which lies closer to the centre of 159715, about 0.1-arcsec away), we still derive $\mu_{\rm lens} < 1.1$.

APPENDIX C: POINT-SOURCE CONTINUUM IN 159717

In Section 3.1, we study the morphology of 159717 and its neighbours using NIRCam and NIRSpec/IFS. Aiming to isolate the sources at $z \sim 5$ from the foreground, we target [O III]λλ4959,5007 emission, which is done in NIRCam by taking the difference between *F277W* and *F200W*, and in NIRSpec by creating an emission-line map centred on [O III]λ5007. The two approaches have different strengths, but they yield different morphological properties for 159717. Here, we show that 159717 has a strong point-source continuum, which NIRCam *F277W*− *F200W* cannot separate from the line emission, unlike NIRSpec/IFS. Such emission could easily explain the different inferences between NIRCam and NIRSpec, as reported in Section 3.1.

In Fig. C1, we show synthetic images derived from the NIRSpec/IFS prism observations, targeting the continuum blueward and redward of the Hβ–[O III]λλ4959,5007 emission-line group, $2.6 < \lambda < 2.9$ μm and $3.1 < \lambda < 3.3$ μm, respectively. 159717 is clearly detected at both wavelengths – as are other sources in the field of view (panels a and b). However, the difference image $b - a$ (Fig. C1c) shows that 159717 is clearly red, which would then leave continuum flux in the *F277W*− *F200W* image (Fig. 4a), while the narrow-wavelength range of the NIRSpec/IFS line map removes the continuum completely (Fig. 4e).

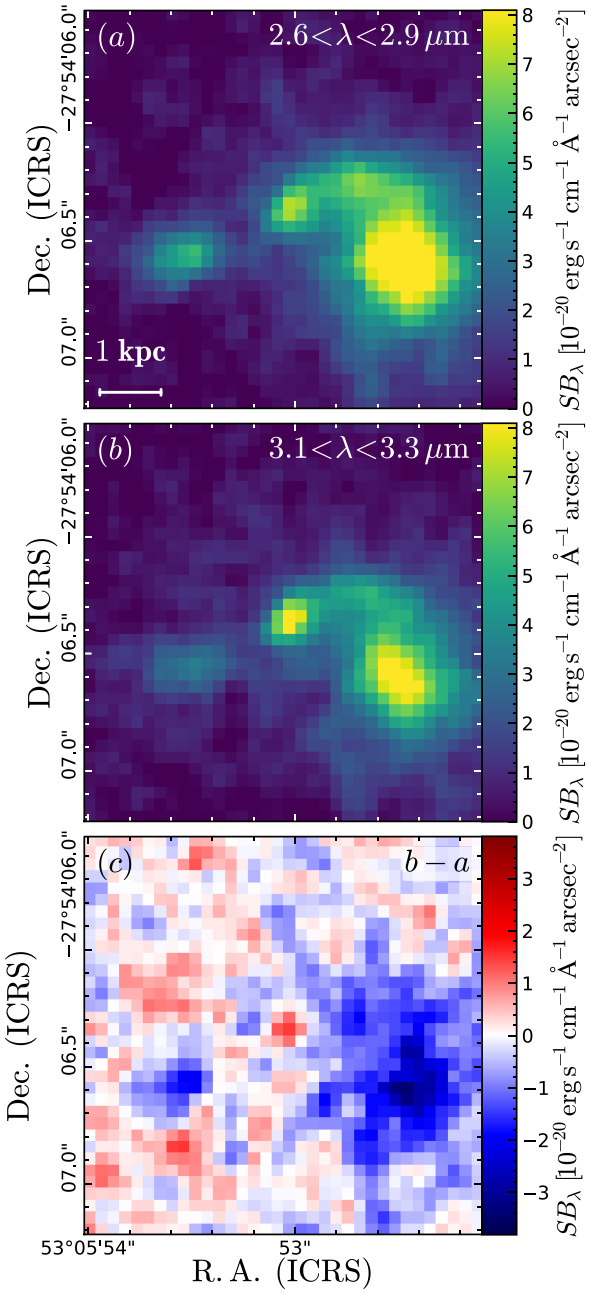

Figure C1. Synthetic images from NIRSpec/IFS prism, in two narrow-wavelength intervals blueward and redward of the Hβ–[O III]λλ4959,5007 complex (panels a and b). Panel (c) shows the flux difference between the two images, acting as a pseudo-colour (but in linear space). The negative regions underscore the blue continuum colour of 159716 and of the foreground galaxy 159715, while 159717 appears in red, indicating the presence of a spectrally red, point-source continuum.

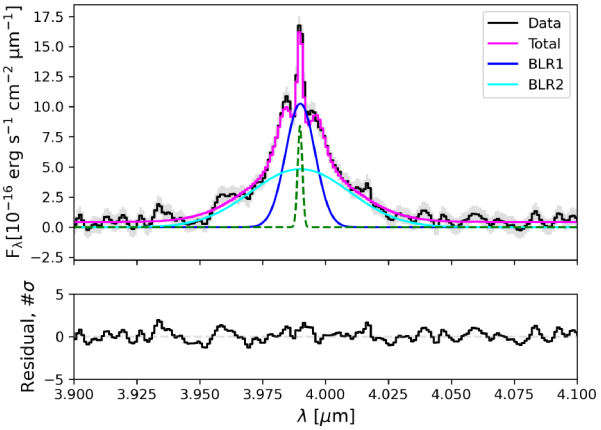

Figure D1. Mock observations of broad Hα in 159717, using the spectral resolution of NIRCam/WFSS. While $R \sim 1600$ can capture the presence of the rest-frame absorber (unlike the NIRSpec $R \sim 1000$ gratings, Fig. 7a), in practice the typical SNR of NIRCam/WFSS is significantly lower, due primarily to the brighter background. This makes slitless spectroscopy excellent for identifying absorbers, but only in bright sources. The lines are the same as Fig. 7.

APPENDIX D: NIRCAM/WFSS FITS

To probe the ability of NIRCam/WFSS to identify rest-frame absorbers, we mock a NIRCam spectrum by convolving the *G*395*H* JADES data to match the resolution of NIRCam *F*444*W* (T. P. Greene et al. 2017; Fig. D1). We then fit this spectrum with the same setup as Fig. 7, with the resulting absorber parameters shown in the corner diagram of Fig. 8 (purple). With resolution $R \sim 1600$, NIRCam/WFSS can clearly identify the absorber, although we note that the actual SNR achieved here would require significantly longer than the 2 h used for NIRSpec. Nevertheless, NIRCam/WFSS seems very well suited to assess the incidence of rest-frame (and other) absorbers in bright sources. As for the inferred parameters, NIRCam/WFSS performs significantly better than the medium-resolution NIRSpec gratings (Fig. 8), but the posterior probabilities are both significantly broader and biased compared to the results from the high-resolution NIRSpec grating.

APPENDIX E: LINE BROADENING DUE TO ELECTRON SCATTERING

The broad-line profiles of some AGN display a distinctively exponential profile (A. Laor 2006). This has also been found in LRD-like AGN (V. Rusakov et al. 2025). In this section, we repeat the fit on the high-SNR aperture, using the scattering assumption. We use the same framework from Section 3.3, but the broad line is modelled as a single emitted Gaussian, which we convolve with a symmetric exponential kernel in wavelength space, $K(\lambda) = 1/(2W)\exp(-|\lambda/W|)$, where W is a free parameter. The emitted and transmitted Gaussian are then rescaled by factors of $\exp(-\tau)$ and $1 - \exp(-\tau)$, respectively, where the optical depth τ is also a free parameter.

The resulting model is illustrated in Fig. E1. We find $\tau = 3.7$, implying that over 98 per cent of the intrinsic broad line has been scattered. W (σ, in theterminology of A. Laor 2006) instead takes a value of 870 km s^{-1}, while the broad-line FWHM is 800 ± 200 km s^{-1}, two times narrower than the fiducial value. With these numbers, and using the calibration from A. E. Reines & M. Volonteri (2015), we obtain an SMBH mass $\log(M_{\bullet,\rm ism}/\mathrm{M}_\odot) = 7.0^{+0.2}_{-0.3}$, four

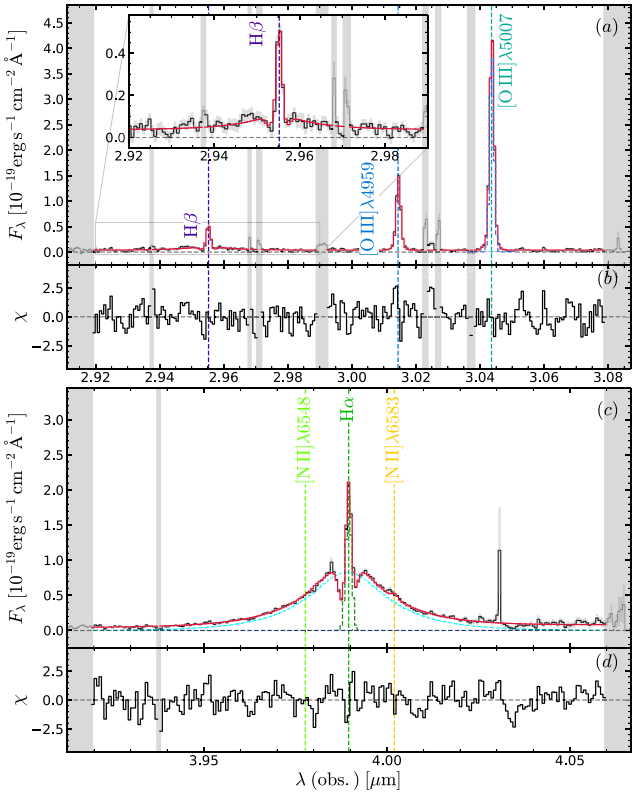

Figure E1. Modelling the broad lines with a single Gaussian and electron scattering, following the approach of A. Laor (2006) and V. Rusakov et al. (2025). This model finds a four times smaller SMBH mass, but our overall conclusions would remain unchanged.

times smaller than the fiducial value, implying a super-Eddington ratio of order 1.6.

The best-fitting model is illustrated in Fig. E1, with the same meaning as the fiducial fit in the main text (Fig. 5). Both models reproduce the data, but there is a possible inconsistency between the large optical depth τ and the relatively narrow scatter parameter W. Using the relation from V. Rusakov et al. (2025), we can in fact estimate τ directly from W, with $\tau(W)$ scaling as $W = (428\,\tau(W) + 370) \times \sqrt{T_e/10^4\ \mathrm{K}}$. With the narrow value of W inferred from the model, we need $T_e \sim 2,000$ K to have $\tau = \tau(W)$, i.e. the large optical depth inferred from the line shapes does not match the width of the exponential. This is also confirmed if we repeat the inference procedure with a model where W is not a free parameter, but is inferred using the relation from V. Rusakov et al. (2025), with τ and T_e as free parameters.

[1]*Kavli Institute for Cosmology, University of Cambridge, Madingley Road, Cambridge CB3 0HA, UK*
[2]*Cavendish Laboratory – Astrophysics Group, University of Cambridge, 19 JJ Thomson Avenue, Cambridge CB3 0HE, UK*
[3]*Department of Physics and Astronomy, University College London, Gower Street, London WC1E 6BT, UK*
[4]*Scuola Normale Superiore, Piazza dei Cavalieri 7, I-56126 Pisa, Italy*
[5]*Centro de Astrobiología (CAB), CSIC–INTA, Cra. de Ajalvir Km. 4, E-28850 Torrejón de Ardoz, Madrid, Spain*
[6]*Max-Planck-Institut für Extraterrestrische Physik (MPE), Gießenbachstraße 1, D-85748 Garching, Germany*
[7]*Dipartimento di Fisica e Astronomia, Università di Bologna, Via Gobetti 93/2, I-40129 Bologna, Italy*

[8]*INAF – Osservatorio di Astrofisica e Scienza dello Spazio di Bologna, Via Gobetti 93/3, I-40129 Bologna, Italy*
[9]*European Space Agency (ESA), European Space Astronomy Centre (ESAC), Camino Bajo del Castillo s/n, E-28692 Villanueva de la Cañada, Madrid, Spain*
[10]*Department of Physics, University of Oxford, Denys Wilkinson Building, Keble Road, Oxford OX1 3RH, UK*
[11]*INAF – Osservatorio Astrofisico di Arcetri, largo E. Fermi 5, I-50127 Firenze, Italy*
[12]*Centre for Astrophysics Research, Department of Physics, Astronomy and Mathematics, University of Hertfordshire, Hatfield AL10 9AB, UK*
[13]*Steward Observatory, University of Arizona, 933 N. Cherry Ave., Tucson, AZ 85721, USA*
[14]*Kavli Institute for Astronomy and Astrophysics, Peking University, Beijing 100871, China*
[15]*Center for Astrophysics | Harvard & Smithsonian, 60 Garden St., Cambridge, MA 02138, USA*
[16]*Department for Astrophysical and Planetary Science, University of Colorado, Boulder, CO 80309, USA*
[17]*Department of Astronomy and Astrophysics, University of California, Santa Cruz, 1156 High Street, Santa Cruz, CA 96054, USA*
[18]*Institut d'Astrophysique de Paris, Paris, 98 bis Boulevard Arago, F-75014 Paris, France*
[19]*NSF, National Optical-Infrared Astronomy Research Laboratory, 950 North Cherry Avenue, Tucson, AZ 85719, USA*
[20]*NRC Herzberg, 5071 West Saanich Rd, Victoria, BC V9E 2E7, Canada*
[21]*Cosmic Dawn Center (DAWN), Copenhagen, Denmark*
[22]*Niels Bohr Institute, University of Copenhagen, Jagtvej 128, DK-2200, Copenhagen, Denmark*

This paper has been typeset from a TEX/LATEX file prepared by the author.